DYNAMICS OF CURRENT-INDUCED SWITCHING IN SPIN-ORBIT TORQUE MAGNETIC DEVICES

WILLIAM SYLVAIN LEGRAND
Engineering Degree
École Polytechnique, France

A THESIS SUBMITTED
FOR THE DEGREE OF MASTER OF ENGINEERING
DEPARTMENT OF ELECTRICAL & COMPUTER ENGINEERING
NATIONAL UNIVERSITY OF SINGAPORE
2016

À Mathilde.

Declaration

I hereby declare that this thesis is my original work and it has been written by me in its entirety. I have duly acknowledged all the sources of information which have been used in this thesis.

This thesis has also not been submitted for any degree in any university previously.

William Legrand
13th March, 2016

Acknowledgements

To begin with the doubtlessly most important part of my Master's thesis, I would like to acknowledge all those thanks to who this step in my studies was completed. I have met many people who shared with me a taste for research and helped me to feel the delightful excitement that exploring physics with friends can bring to the mind. In no particular order,

my many thanks go to my supervisor Prof. Yang, who hired me in his great research team for my time in NUS and advised me, week after week, on the orientation of my projects,

Jae Hyun, thank you for your great help and support during my stay in SEL. It has been a pleasure to work with you these long evenings in the cleanroom, and all of my experiments have been completed only thanks to your help,

to Xuepeng, many thanks to you, as you always found the patience of sharing your knowledge with me. You have been a model as a researcher and an example regarding your attitude with your juniors. It has been really great to work together,

thanks also to Baochen and Habee for their work, taking care of all of us staying in the lab and providing for our needs, and always doing it with a smile,

Sagaran, thanks for your wise advice and your inspiring attitude. I enjoyed enjoying my cups of coffee with you, that you always have an interesting

topic to discuss, and your unique nature that makes you the friend you are,

to Tanmay, thank you for all the time we shared in and out the lab. We have been sitting together, travelling together, and above all, discussing together so many times. I will always keep a (Chinese apple) cake ready for you,

thanks Rahul for being such a nice classmate and such a relaxed labmate. It was very enjoyable to be with you day and night here and to learn your stories,

thank you Raj, for standing together in the graduate life. It has been such a pleasure to study and work with you day after day, and also I have to thank you for all the help you have given, probably as much as if you were my senior tutor,

to Jean, thank you for having been supporting me, as a motivator, as a source of daily passionating scientific discussions, as a friend. We had ten years of difference when I arrived but it is like we have known each other for ten years now that I leave,

to Yi, Jungbum, Jaesung, Praveen, Liming, Reuben, Shawn, Shreia, Jiawei, Karan, Wu Yang, Mehrdad, Liu Yang, Shalabh, Shawn, Dapeng, Pan, Gurleen, Sumendu, Shuyuan, Mengji, thank you all for staying together as a team, sharing some thoughts and some efforts, or much time after work. I do not thank you individually in link with this work but you know how much I enjoyed to be with you in Singapore, and what I appreciate in you in all other aspects. And if I have forgotten any of you, you anyway know for sure what I am thankful to you for and how much I like you,

and to all of you, see you soon!

Table of Contents

Declaration **iii**

Acknowledgements **iv**

Table of Contents **vi**

Abstract **viii**

List of Tables **ix**

List of Figures **x**

List of Symbols and Constants **xii**

Introduction **1**

1 Magnetic memory devices **3**
1.1 Magnetoresistance in magnetic multilayers 4
1.2 Magnetization switching by spin-transfer torques 6
1.3 Application to magnetic memories 7

2 Magnetization dynamics **11**
2.1 Magnetic interactions 11
2.2 Landau-Lifshitz-Gilbert equation 19
2.3 The macrospin description 22

3 Magnetization switching by spin-orbit torques **27**
3.1 Origins of spin-orbit torques in magnetic multilayers 27
3.2 Perpendicular magnetic anisotropy and spin-orbit torques . . 31
3.3 Switching processes 34
3.4 Spin-orbit-torque-driven magnetic memories 37

4 Dynamic spin-orbit torque switching without external fields **41**
4.1 Nature of the Slonczewski and field-like torques 41
4.2 Varying the torques ratio 46
4.3 Influence of the rising time 53
4.4 Switching times and anisotropy 56
4.5 Validation by micromagnetic simulations 60
4.6 Conclusions 63

5 Spin-orbit torques in the thermal regime **67**
5.1 Thermal processes and Fokker-Planck equation 67
5.2 Thermal barrier under currents 70
5.3 Field-like torque influence on thermal regime 74
5.4 Finding the right assist field angle 76
5.5 Conclusions 79

6 Triaxial anisotropy in spin-orbit torque devices **81**
6.1 Principle of triaxial anisotropy in ellipse-shaped devices . . . 81
6.2 Asymmetric destabilization of the equilibria 84
6.3 Experimental investigation 87
6.4 Conclusions and remaining works 94

Conclusions and recommendations **97**

Bibliography **101**

Abstract

Spin-orbit torques in heavy metal/ferromagnet bilayers are expected to overcome spin-transfer torques for application to magnetic memories, in terms of power-efficiency, endurance and speed. However, switching nanomagnets by spin-orbit torques is hindered by a limited understanding of their switching dynamics as well as by the requirement that an external assist field must be applied to the systems to ensure deterministic switching. This thesis addresses these two emergent issues of spin-orbit-torque induced dynamics. The non-linear behaviour of the magnetization under a combination of the different spin-orbit torques is first analysed and reveals a regime of dynamic switching that does not require any external assist field. This study is then extended to the thermal regime where the switching requirements and the roles of the different torques are investigated using the Lagrangian-Hamiltonian theory. Finally, switching is analysed for triaxial anisotropy devices in which the additional shape anisotropy of ellipses can advantageously replace the assist field for deterministic spin-orbit torque switching. These simple and efficient switching schemes may greatly contribute to the realization of spin-orbit-torque-based memories.

- Legrand, W., Ramaswamy, R., Mishra, R. & Yang, H. Coherent Subnanosecond Switching of Perpendicular Magnetization by the Fieldlike Spin-Orbit Torque without an External Magnetic Field, Phys. Rev. Appl. **3**, 064012 (2015).

- Legrand, W., Ramaswamy, R., Mishra, R. & Yang, H. Coherent Sub-Nanosecond Switching of Perpendicular Magnetization by the Field-Like Spin-Orbit Torque Without External Magnetic Field. (oral), Intermag 2015, May 11^{th}–15^{th}, Beijing.

List of Tables

6.1 Values of the demagnetizing factors and reduced anisotropy for different ellipse sizes. 84

List of Figures

1.1 Schematic illustration of the GMR in a perpendicular configuration 6
1.2 Schematic illustration of the spin-valve concept and reading/writing schemes in field-operated versus spin-transfer torque MRAM 8

2.1 Energy minimization principle in a perpendicularly magnetized system 19
2.2 Coordinate system and angles 23
2.3 Solution trajectories of the Landau-Lifshitz-Gilbert (LLG) equation in the macrospin approximation 25

3.1 Schematic picture of the spin Hall effect and Rashba mechanism in heavy-metal/ferromagnet/oxide stacks 28
3.2 Location of the different possible equilibria under spin-orbit torques and perpendicularly magnetic anisotropy 32

4.1 Differences between the Slonczewski and field-like torques in the quasi-static and dynamic regime 44
4.2 Isoenergetic orbits under the influence of the field-like torque in the dynamic regime 47
4.3 Switching trajectories obtained for increasing values of the ratio between the Slonczewski and the field-like torques in the absence of external fields 49
4.4 Switching outcome as a function of the strengh of the field-like and Slonczewski torques 51
4.5 Switching trajectories obtained for increasing values of the rising time of the pulse 54
4.6 Switching outcome as a function of the strength of the field-like and Slonczewski torques for finite rising times 55
4.7 Switching outcome as a function of the anisotropy and current density 57
4.8 Switching times as a function of the anisotropy for two rising times 59
4.9 Micromagnetic simulations of dynamic spin-orbit torque switching for different sizes and strengths of the Dzyaloshinskii-Moriya interaction 65

5.1 Evolution of the barrier height with the amplitude of the assist field for different torques ratios 75
5.2 Evolution of the barrier height with the angle of the assist field for different torques ratios 77

5.3 Evolution of the barrier height with the magnitude of a rotated in-plane assist field in the case of a significant field-like torque 78

6.1 Schematics of devices with triaxial anisotropy 83
6.2 Vertical component of the magnetization under current in ellipse-shaped devices 86
6.3 Schematic (top view) of the geometry of our devices and definition of the measurement currents 88
6.4 Out-of-plane and in-plane field swept anomalous Hall resistance measurements 89
6.5 Spin-orbit torque current-induced switching loops of circle devices in the presence of different assist fields 90
6.6 Spin-orbit torque current-induced switching loops of ellipse devices (45° rotation) in the presence of different assist fields 91
6.7 Spin-orbit torque current-induced switching loops at zero field 92

List of Symbols and Constants

AHR	Anomalous Hall Resistance.
CIP	Current In-Plane.
CPP	Current Perpendicular to the Plane.
DMI	Dzyalonshinskii-Moriya Interaction.
DW	Domain-wall.
FM	Ferromagnet.
GMR	Giant Magnetoresistance.
HM	Heavy-metal.
MRAM	Magnetic Random Access Memory.
MTJ	Magnetic Tunnel Junction.
NM	Non-magnet.
SOT	Spin-Orbit Torque.
STT	Spin-Transfer Torque.
TMR	Tunneling Magnetoresistance.

Introduction

In the field of spintronics the manipulation of the magnetization can be achieved by utlizing the degree of freedom that spin provides in order to realize next generation electronic systems and components. Less than thirty years old, spintronics is still a young field in condensed-matter physics, but intensely studied as it benefits from various other fields such as magnetism, materials science, and quantum and statistical physics. With the announced end of the successive, continuous miniaturization in the silicon electronics, many candidate materials and physical mechanisms are being proposed for further technological improvement or even replacement of the present technology. Therefore, a strong interest for magnetic systems has emerged, especially regarding random access memories, given their many advantages in terms of non-volatility and energy requirements. Random access memories are very often a critical component limiting the performance of the systems, as they are embedded in a vehicle, part of a computational unit or more generally integrated into almost any electronic equipment. The present Master's thesis deals with the operation and performances of a particular type of magnetic systems, proposed since the very recent discovery of a new physical phenomenon in spintronics: the spin-orbit torques. In addition to the interesting physics involved in the manipulation of the magnetization by spin-orbit torques, its development is expected to lead to a promising alternative to silicon-based random access memories.

This thesis has been divided into two parts. A first part, which includes the first three chapters, constitutes a review and provides the required background to approach magnetization dynamics applied to magnetic memories. Chapter 1 is devoted to a brief history of the evolution of spintronics devices, in order to introduce the present technology of spin torque memories. Chapter 2 focuses on basic concepts in magnetism and micromagnetics which are used in the present work. After this introduction, Chapter 3 opens the topic of spin-orbit torques and provides a summarized description of its physics, an analysis of its switching properties and its expected advantages for magnetic memory applications. The second part of this thesis presents its original work and includes the next three chapters. Each of them deals with one of three complementary regimes of spin-orbit-torque-induced magnetization switching. In Chapter 4, a dynamic approach is adopted in order to develop a switching scheme that provides a high degree of control over the motion and the final state of the magnetization. Chapter 5 deals with the thermal activation regime, and provides a theoretical framework for spin-orbit torque switching analysis. Chapter 6 finally focuses on an easily accessible, quasi-static regime without exploiting high-speed dynamics aspects, acting on the symmetries of the system to offer deterministic switching properties.

Chapter 1

Magnetic memory devices

Whatever the generations and the types of solid-state memories, the adopted technical solutions have always strived to address the same critical requirements, which can be summarized as follows: (i) ensuring the best data retention properties over time, with endurance against the physical environment; (ii) minimising the error rates during reading and writing operations; (iii) requiring the shortest operation times; (iv) being scalable down to the lowest sizes in order to increase the density of memory embedded in one chip and (v) saving power by reducing the operating currents and energies. Even though this thesis does not intend to formally focus on the applicability of the physical mechanisms it deals with, the present introductory chapter will explain how these few essential needs motivate this work on the dynamics of the spin-orbit torques. In addition, keeping these criteria in mind will be useful throughout the thesis in order to appreciate the properties attributable to spin-orbit torques. Before we address the dynamics of spin-orbit torque, we first briefly review the background founded by the successive discoveries that lead to the present generation of magnetic devices, with a particular focus on magnetic memories.

1.1 Magnetoresistance in magnetic multilayers

The discovery of the Giant Magnetoresistance (GMR) in magnetic multilayers by Fert and Grünberg in 1988 [1, 2] immediately opened a new and vast subfield in solid-state physics, now referred as spintronics. In spintronics, the spin-dependent properties of the electrons rather than their charge-dependent properties are studied. The whole field of spintronics is therefore intrinsically related to magnetism. The GMR effect (and the numerous subsequent discoveries it allowed) immediately found applications in the electronics industry as hard-disk drives read heads, and not long after, in magnetoresistive random-access memories (MRAM) as we will discuss in §1.3.

The historical systems that first evidenced the GMR effect are multilayered thin-film or ultrathin-film structures composed of alternating ferromagnetic and non-magnetic layers. In these structures, the variation of resistance with respect to the relative orientations of the magnetization in the ferromagnetic layers (the magnetoresistance) is explained by the spin-dependent scattering of the conduction electrons. It is to be mentionned that GMR is observed in two different geometries, namely the current in plane (CIP) and current perpendicular to the plane (CPP) geometries, depending on whether the current flows along the layers or across them, respectively. The origins of the CIP-GMR [3] and CPP-GMR [4] are not fundamentally different: we will thus only describe the case of the CPP geometry, which is of more relevance for nowadays applications, and especially for spin torque memories, as we will discuss below. The interested reader may refer to the several references given here for a more detailed description and modelling of these two

phenomena.

Consider a trilayered structure made of two ferromagnetic (FM) layers separated by a non-magnetic (NM) spacer, for example, where the FM is Fe and the NM is Cr as in Ref. [1]. Due to the NM spacer, the magnetization inside the two FM layers can be set either aligned along the same direction, which is the parallel (P) configuration, or along opposite directions, which is the antiparallel (AP) configuration, as represented in Fig. 1.1. The conduction electrons become spin-polarized in the direction of the magnetization when they flow through the FM layers, after which they are injected from one layer into the other one. As their spin is polarized either parallel or antiparallel to the FM magnetization, two channels of conduction are defined, one for spin-up and one for spin-down. The scattering of conduction electrons is significantly stronger for the electrons whose spin is opposed to the local magnetization, resulting in different resistivities for the two conduction channels, as can be seen in Fig. 1.1. When considering the total conductivity, the structure is more resistive in the AP state than it is in the P state, and therefore, the magnetic configuration of the layers can be easily detected by an electrical current as the magnetoresistance ratio—the relative difference of resistance between the AP and P states—can reach several tens of percent.

Nevertheless, many layers may be required to obtain a significant magnetoresistance at room temperature. A significant improvement of the magnetoresistance was achieved using the tunnelling magnetoresistance (TMR) in magnetic tunnel junctions (MTJ). In an MTJ, the two FM layers are separated by an insulator rather than by a NM metal. With the insulating barrier layer as thin as several Å, a tunnelling current can flow. Because of

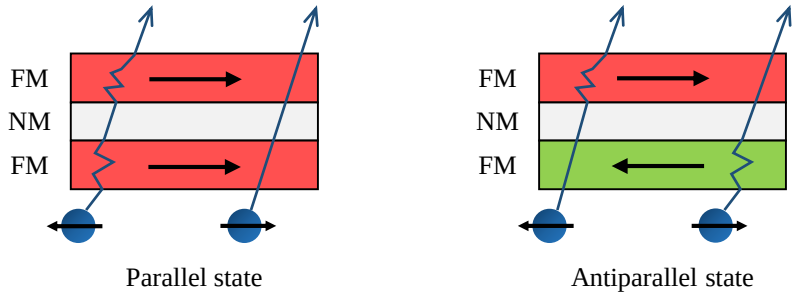

Figure 1.1: Schematic illustration of the GMR in a perpendicular configuration. The two FM layers can be either in the P (left panel) or AP (right panel) states. The two channels of conduction spin-up and spin-down are represented, and the blue arrows show the spin-dependant scattering inside the FM layers.

spin-dependent tunnelling the amount of current is dramatically affected by the relative orientations of the magnetization in the FM electrodes, giving rise to a very large magnetoresistance between the P and AP states. The principle of the TMR is known since Julliere's calculations dating back to 1975 [5], but an effective demonstration of the TMR had to wait for a reliable fabrication processes until 1995 [6, 7]. The TMR contributed to improve the magnetoresistance of the devices by one order of magnitude, and materials choices in MTJs achieving coherent tunnelling contributed another tenfold increase in the magnetoresistance. The latest reports demonstrate magnetoresistance ratios larger than 600% at room temperature [8]. With such high TMR ratios, an ultrafast electrical reading of the magnetic state—below the nanosecond scale—can easily be implemented.

1.2 Magnetization switching by spin-transfer torques

As we have seen in the previous section, an initially non-spin-polarized current flowing through the CPP spin-valve structure is spin-polarized when it flows through any of the FM layers. Because of the conservation of the

total angular momentum, this process of local exchange interaction implies that the flowing electrons conversely exert a reciprocal torque on the magnetization of the FM layer. The idea of Slonczewski that a large enough current can be capable of switching the magnetization of a FM layer by a process called spin-transfer torque (STT) [9] has been verified experimentally in metallic spin-valves just before the 2000's [10]. In this new scheme, it is possible to switch from the AP to the P configuration, as the electrons are polarized in one of the layer, and reverse the other layer (as it aligns with the flow of polarized electrons). The fact that the spin-transfer torque effects act not only in the direction of the flowing electrons, but also due to reflected electrons, makes it possible to reverse the direction of the switching to generate the AP state from the P state as well, only by reversing the current [9]. Spin-transfer torques physically originate in spin-transport phenomena that we will not cover here. For the interested reader, detailed investigations on the origins of spin-transfer torques can be found in Refs. [11–13]. A theoretical description of how the magnetization reverses from one direction to the opposite one is necessary in order to understand the principles of magnetization dynamics investigated in this thesis: the dynamics of magnetization switching will be covered in Chapter 2.

1.3 Application to magnetic memories

To make a device out of a GMR or TMR trilayer, it is often designed as a spin-valve, as shown in Fig. 1.2a. In a spin-valve, the magnetization of one of the two FM layers (the reference layer) is fixed by coupling it strongly with a neighbouring pinning layer (usually, an antiferromagnet) while the other FM layer (the free layer) is free of any coupling, and can be reversed externally.

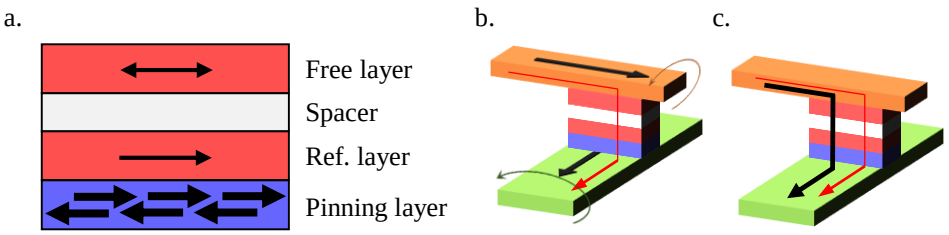

Figure 1.2: a. Schematic illustration of a spin-valve showing the free layer (symbolized by the double-ended arrow), the reference layer (simple arrow) and the antiferromagnet pinning layer (multiple thick arrows). Reading and writing operation concept for b. field-operated and c. spin-transfer torque MRAM unit cells and current lines. The reading currents are the red lines while the writing currents are the thick black arrows. In b., the colored arrows represent the Oersted fields that reverse the free-layer magnetization.

The spin-valve can thus be used to obtain a very sensitive magnetic response. The easy electrical readout of the magnetic state in GMR spin-valves, and to an even larger extent, in MTJs, make them also perfectly suitable to build elementary memory cells. An MRAM chip is nothing else than an array of such MTJ-based memory elements, where the binary magnetic state (P or AP) of every single junction encodes one bit of information. In the first generation of MRAM devices, the reading process was based on the electrical reading of the magnetoresistance, and was associated with a simple writing process: the free layers of the junctions were switched by the Oersted field created from large currents flowing along a 'write' current line on top of the devices (see Fig. 1.2b). However, this approach was not satisfactorily scalable, as the required current densities to achieve field-induced switching dramatically diverge when the size of the devices is reduced, in addition to increased crosstalk between the neighbouring cells. The solution to scale down the magnetic memory devices has then been found in using current-induced switching by spin-transfer torque.

In the spin-transfer torque MRAM, the writing operation as well as the

reading operation are performed by flowing the current through the spin-valve. Only the intensity of the current varies between reading and writing: reading is done at a low current to read the magnetoresistance without affecting the magnetic state, while writing any of the AP or P states is achieved by passing a high current through the structure, as represented in Fig. 1.2c. It is essential for a memory that it can be switched back and forth between the two states: this is achieved using the two opposite directions of the current flowing across the layers.

The advantages of the STT-MRAM technology among previous generations are diverse. First, the spin-valve is a simple, two-terminal device, that occupies less chip area. Second, switching can be achieved at lower currents than in the previous field-switched MRAM scheme. Third, the operation speed is enhanced as compared to the field-switched scheme. To move forward beyond the STT-MRAM technology, a new operation scheme would need to enhance the performance of the devices, at least, with respect to these three criteria. As we will see in Chapter 3, one promising candidate is found in spin-orbit torques (SOTs), which constitutes the primary motivation for this thesis' work. In order to explain the differences between SOT and STT, we will first study the essential principles of magnetization dynamics in Chapter 2, before we introduce the SOTs in Chapter 3.

Chapter 2

Magnetization dynamics

This chapter aims at introducing the basic concepts in the physics of magnetization dynamics that constitute a starting point for this work. The chapter therefore opens with a description of the different magnetic interactions and associated energies at the microscopic scales that rule the behaviour of magnetic systems (§2.1). These energies also drive, through the concept of effective magnetic field, the dynamics of the system as described by the Landau-Lifshitz-Gilbert equation (§2.2). A simplified but extremely useful model of magnetic system is then presented in order to introduce some general behaviours of the magnetic systems (§2.3).

2.1 Magnetic interactions

The magnetic state in a material can be defined when its electrons are affected by magnetic fields: a large variety of behaviours occur in many kinds of magnetic orderings. In this work, we are interested in the behaviour of spontaneous magnetization materials, in which the magnetic ordering is not caused by the application of external fields but, on the contrary, remains even in the absence of fields and currents, as this retention of the magnetic state is indeed essential to build a memory, for instance. This is possible in materials that spontaneously have unpaired electrons, which create magnetic

moments. The magnetic moments are a vector quantity, which defines a direction and an amplitude of magnetization. The magnetic phase of the core electrons inside a solid-state magnet is well described by a set of spatially fixed magnetic moments, each moment accounting for the behaviour of the electrons located at each atom[1]. Other interactions are due to the magnetic moments of the delocalized electrons.

Moreover, for the magnetization to be permanent, the magnetic moments of the electrons have to remain unaffected by the fluctuations that any individual quantity is subject to: at room temperature, this happens notably in ferromagnets and antiferromagnets. In a ferromagnet, the neighbouring moments have a tendency to align their directions, while in an antiferromagnet, they tend to be aligned along opposite directions. This forms larger volumes with coherent, almost identical (or alternate) moments, that can resist quantum fluctuations to define a stable magnetization. This work is focusing on the behaviour of ferromagnetic systems, but we should note that the dynamics of antiferromagnetic systems under current-induced torques are a growing field of much interest as well (see, e.g., [14, 15]).

The size of the magnetic systems we are interested in is most often of mesoscopic scale, and thus a continuous description of the magnetization is of more relevance for the dynamics that an atomistic description, especially given that the neighbouring moments aligns well with each other. To build this continuous description, we introduce the local magnetization $\mathbf{M}$, which is the sum of a local subset of magnetic moments divided by the infinitesimal local volume they belong to (in antiferromagnets, a similar treatment can be done for two sublattices of opposite moments). In the usual ferromagnets

[1] by fixing the positions of the magnetic moments, we neglect all kind of deformations originating in magnetic interactions, such as magnetostriction.

far from their Curie temperature (the temperature at which they lose their ferromagnetic properties), the modulus of the local magnetization $M_S = |\mathbf{M}|$ cannot change, but only its direction $\mathbf{m}$ can rotate and can thus be defined by $\mathbf{M}/M_S$. $\mathbf{m}$ is called the reduced magnetization. The following subsections describe into some more details the different types of interactions affecting $\mathbf{M}$ in ferromagnets. We also define the energies associated with each of them, as they will allow us to subsequently derive the dynamics of $\mathbf{M}$, in §2.2.

2.1.1 Exchange interaction

Mainly due to the Pauli exclusion principle, the orbits of two neighbouring electrons can overlap significantly more when their spin are antiparallel rather than parallel. This, in turn, causes a lower energy state for aligned neighbouring moments in ferromagnets as the Coulomb interaction disfavours overlapping orbitals[2]. These combined influences of the electronic orbitals and positions of two electron of spin states $\mathbf{S_i}$ and $\mathbf{S_j}$ are included into the exchange integral term J that defines the relative difference of energy between the aligned and antialigned neighbouring orbitals as in $E = -2J(\mathbf{S_i} \cdot \mathbf{S_j})$. By integration over all the neighbouring moments in a volume V, one finds the exchange energy density

$$\varepsilon_{ex} = \frac{A_{ex}}{V} \int dV (\nabla \mathbf{m})^2 \tag{2.1}$$

with A_{ex} the exchange stiffness constant, proportional to J and inversely proportional to the lattice parameter. The effect of the exchange interaction is to favor domains of uniform magnetization. For typical ferromagnets made of Co, Ni, Fe and their alloys, A_{ex} is in the range of 10–30 pJ m^{-1} [16].

[2] this is an extremely simplified explanation. Under some conditions, the antialigned neighbouring moments have a lower energy, which notably gives rise to antiferromagnetism

2.1.2 Dzyaloshinskii-Moriya interaction

It has been recently highlighted that another local magnetic interaction affects the magnetization states in thin-film ferromagnets: the Dzyalonshinkii-Moriya interaction (DMI). It is an antisymmetric exchange interaction that originates in spin-orbit coupling, and it can be observed when the materials structure lacks inversion symmetry, notably in the case of asymmetric interfaces [17]. Differently than in the case of the symmetric exchange interaction, the energy for two neighbouring spins $\mathbf{S_i}$ and $\mathbf{S_j}$ coupled by the DMI is $E = \mathbf{D_{ij}} \cdot (\mathbf{S_i} \times \mathbf{S_j})$, where $\mathbf{D_{ij}}$ is a DMI-related vector. By integration over all the neighbouring moments in a volume V, one finds the DMI energy density to be

$$\varepsilon_{dmi} = \frac{1}{V} \int dV \sum_{i=x,y,z} \mathbf{D_i} \cdot \left(\mathbf{m} \times \frac{\partial \mathbf{m}}{\partial i} \right) \tag{2.2}$$

with $\mathbf{D_i}$ the DMI vectors, whose signs of components determines the chirality of the magnetic ordering for the different symmetry breaking directions and whose values range up to 1–2 mJ m^{-2} for usual HM/FM interfaces [18]. In thin film ferromagnets, the magnetization is extremely close to be uniform in the vertical z direction, and the DMI originates from the symmetry breaking in the same direction at the interface.

2.1.3 Dipolar interaction

Any single magnetic moment inside the system is also affected, as a dipole, by the magnetic dipolar interaction with all the other moments. As compared to the local exchange interaction that is limited to the immediate neighbours only, the dipolar interaction has a longer range (as it decays as $1/r^3$) and can thus give rise to non-local fields at the scale of the whole system. However, the dipolar interaction is several orders of magnitude weaker

than the exchange interaction: the formation of coherent domains in ferromagnets, as mentioned above, originates in the exchange interaction, while the dipolar fields only contribute to orientate them depending on the geometry of the sample. The dipolar interaction with all the moments of the system can be integrated into an local (and thus non-uniform over the different dimensions of the system) demagnetizing field $\mathbf{H_d}$ acting on the magnetic moment. Integrating over all the individual moments translates in the continuous description into defining the demagnetizing field as originating from a magnetic scalar potential ψ such that $\mathbf{H_d} = -\nabla\psi$ where ψ is defined by $\mathbf{M}$ all over the magnet. For a simply connected domain and in the absence of currents, ψ is found by solving $\nabla^2\psi_{in} = \nabla \cdot \mathbf{M}$ inside the magnet and $\nabla\psi_{out} = 0$ outside the magnet, with the following boundary conditions: at the surface of the magnet, ψ and its derivative along the normal $\mathbf{n}$ to the surface, noted $\dot{\psi}$, obey $\psi_{in} = \psi_{out}$ and $\dot{\psi_{in}} = \dot{\psi_{out}} + \mathbf{M} \cdot \mathbf{n}$, respectively. $\mathbf{M}$ is indeed interacting with itself, hence the name of demagnetizing field, as $\mathbf{H_d}$ points against the internal magnetic field. In terms of energy, we have

$$\varepsilon_d = -\frac{\mu_0}{2V} \int dV (\mathbf{M} \cdot \mathbf{H_d}). \tag{2.3}$$

Finding $\mathbf{H_d}(\mathbf{r})$ from $\mathbf{M}(\mathbf{r})$ analytically is in general extremely complex in any particular geometries of realistic magnets. However, a rather useful model system is given by the ellipsoid with a uniform magnetization. Defining the three principal axes unit vectors of the ellipsoid $\hat{\mathbf{x}}$, $\hat{\mathbf{y}}$ and $\hat{\mathbf{z}}$, one have

$$\mathbf{H_d} = -[N_x(\mathbf{M} \cdot \hat{\mathbf{x}})\hat{\mathbf{x}} + N_y(\mathbf{M} \cdot \hat{\mathbf{y}})\hat{\mathbf{y}} + N_z(\mathbf{M} \cdot \hat{\mathbf{z}})\hat{\mathbf{z}}] \tag{2.4}$$

where N_x, N_y and N_z are the three demagnetizing factors which verify $N_x + N_y + N_z = 1$. This gives

$$\varepsilon_d = \frac{\mu_0}{2} M_S^2 \Big[N_x (\mathbf{m} \cdot \hat{\mathbf{x}})^2 + N_y (\mathbf{m} \cdot \hat{\mathbf{y}})^2 + N_z (\mathbf{m} \cdot \hat{\mathbf{z}})^2 \Big] \tag{2.5}$$

which can be extended to any system close to a uniformly magnetized volume of simple geometry (prism, disk, etc.) by some approximation. N_x, N_y and N_z are lower in the longest dimension of the system, so that the magnetization naturally aligns along the longest dimensions of a magnetic object.

2.1.4 Zeeman energy

Any magnetic dipole naturally rotates to align itself with the direction of an applied magnetic field. This interaction is integrated over the microscopic scale into the Zeeman energy term

$$\varepsilon_z = -\frac{\mu_0}{V} \int dV (\mathbf{M} \cdot \mathbf{H_{ext}}). \tag{2.6}$$

The Zeeman energy tends to make $\mathbf{M}$ aligned with $\mathbf{H_{ext}}$.

2.1.5 Magnetic anisotropy

The magnetic systems do not necessarily have the same properties in all directions. This is called magnetic anisotropy, and it is actually extremely useful to exploit materials which exhibit magnetic anisotropy as they give rise to more complex behaviours and energy landscapes, thus providing extra degrees of freedom for realizing specific magnetic configurations. Microscopically, the magnetic anisotropy arises from the shape of the electronic orbitals in the materials and their interactions, depending on their spatial ordering.

We distinguish two principal kinds of magnetic anisotropy, namely, magnetocrystalline and interfacial anisotropies. Magnetocrystalline anisotropy is found in crystalline materials, in which some axes of the magnetization are preferred over the other directions due to the crystalline order. This adds an angular dependence to the energy: in the simplest case of a uniaxial anisotropy along an axis $\hat{\mathbf{u}}$, we can define

$$\varepsilon_u = -K_2(\mathbf{m}\cdot\hat{\mathbf{u}})^2 - \frac{K_4}{2}(\mathbf{m}\cdot\hat{\mathbf{u}})^4 \tag{2.7}$$

where K_2 and K_4 define the strength and angular dependence of the anisotropy. From Eq. (2.7), it is seen that the magnetic anisotropy favours a particular axis but no direction along it, and thus cannot break the symmetry along this axis.

The case of an interfacial anisotropy occurs in ultrathin films, where the interaction with other atoms at the surface of the magnetic material is no longer negligible as compared to the interactions within its inner volume. Because of the electronic interactions between the different atoms in contact, an additional anisotropy arises from this surface contribution. It then has a form similar to the one of Eq. (2.7). In addition, K_2 and K_4 scale as the inverse of the thickness, because the interfacial effect is proportional to the surface while affecting the whole volume. In thin films, the interfacial anisotropy is directed along the direction of symmetry breaking, perpendicular to the film plane.

It is to be noted that Eq. (2.7) is very similar to Eq. (2.5): therefore the effect of the demagnetizing fields in uniformly magnetized systems is referred to as a shape anisotropy. This shape anisotropy can compete with

the anisotropy due to the material and may result in a system with a complex angular dependence of the magnetization energy. The case of a uniaxial anisotropy is common in thin films and very often used in magnetic devices, as we have seen in Chapter 1. In ultrathin films, the interfacial anisotropy can easily dominate over any other anisotropy to produce a perpendicular magnetic anisotropy, which is of particular interest when combined with current-induced switching [19]. More complex behaviours arise when other anisotropy axes are present: notably, we will cover the case of a triaxial anisotropy, in relation with spin-orbit torques, into more details in Chapter 6.

2.1.6 Energy minimization

Finding the energy landscape of the system is essential for finding the equilibrium states of the system. They are found by minimizing the overall energy in the magnet, $\varepsilon_{tot} = \varepsilon_{ex} + \varepsilon_{dmi} + \varepsilon_d + \varepsilon_z + \varepsilon_u$. To give one example among the large diversity of magnetic systems and behaviours related to this energy minimization principle, consider the case of a simple square-shaped thin film magnet. Owing to the demagnetizing energy (Eq. (2.3)), the magnetization on the edges of the system tends to align with them: as the magnet is very thin in its vertical dimension, $N_z \approx 1$, which implies that $\mathbf{m}$ should be in-plane, as represented in Fig. 2.1a. However, if a large out-of plane magnetic anisotropy is present in the system, $\mathbf{m}$ is stabilized out-of plane against the demagnetizing energy (Fig. 2.1b). The exchange anisotropy favours the formation of uniformly magnetized domains, and $\mathbf{m}$ will be pointing upwards or downwards everywhere in a domain in order to minimize ε_{ex}. If the magnet is small enough the exchange interaction will dominate at the short

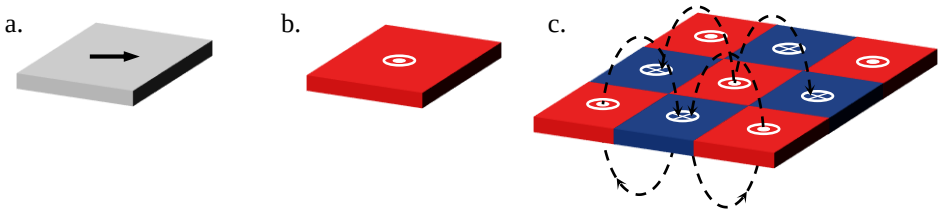

Figure 2.1: Energy minimization principle in a perpendicularly magnetized system. a. A square ferromagnet magnetized in-plane in the absence of interfacial anisotropy. b. A square ferromagnet magnetized out-of-plane due to high interfacial anisotropy. c. A magnet showing chequerboard demagnetizing patterns. The red colour corresponds to **m** pointing up and the blue colour corresponds to **m** pointing down. The black arrows represent the dipolar interactions between the neighbouring domains.

length scale, and the magnetization will remain uniform. However, when the size of the square is increased, the magnetization can break into subdomains with different—but uniform in each—magnetization. These subdomains will arrange to minimize the dipolar interaction between each domain, roughly mimicking a chequerboard pattern, as shown in Fig. 2.1c. At the boundary between two different domains, the linear transition area where **m** changes from the magnetization of one domain to the magnetization of its neighbour domain is called a domain wall (DW). In terms of energy, ε_{tot} is minimized by a reduction of ε_d at the cost of a slightly larger ε_{ex} and ε_u along the DWs.

2.2 Landau-Lifshitz-Gilbert equation

The concept of magnetic energy minimization described above is suitable for providing the ground, equilibrium state of a magnetic system. However, all the different non-equilibrium behaviours, including the switching events and processes, obey to dynamics that need to be described in time-domain at the sub-nanosecond scale. By analogy with the Larmor precession, it is expected that the magnetic moment inside a system will precess around

any internally generated or externally applied magnetic field. Also, due to the different energy dissipation processes coming into play, an additional damping occurs which helps the system to reach its low energy state. This behaviour of a single magnetic moment $\mathbf{m_s}$ is described by the Landau-Lifshitz (LL) equation

$$\frac{d\mathbf{m_s}}{dt} = -\gamma\mu_0\mathbf{m_s} \times \mathbf{H_{eff}} - \lambda\mathbf{m_s} \times (\mathbf{m_s} \times \mathbf{H_{eff}}) \tag{2.8}$$

in which the first term on the right hand side describes the precession and the second term describes the damping, with γ the gyromagnetic ratio (positive by convention), λ a phenomenological damping parameter (positive to have energy dissipation), and $\mu_0\mathbf{H_{eff}}$ the effective magnetic field causing the precession.

The magnetization dynamics of a mesoscopic system are following the same time evolution. However, the LL equation does not perfectly describe the behaviour of ferromagnets, notably when there is a large damping. The Landau-Lifshitz-Gilbert (LLG) equation is often preferred, which also predicts the precession of the magnetization around effective fields, or, equivalently, in response to the torques. Considering the magnetization $\mathbf{M}$ to be a function of both time and space $\mathbf{M}(\mathbf{r}, t)$, the LLG equation reads as follow

$$\frac{\partial\mathbf{M}}{\partial t} = -\gamma\mu_0\mathbf{M} \times \mathbf{H_{eff}} + \frac{\alpha}{M_S}\left(\mathbf{M} \times \frac{\partial\mathbf{M}}{\partial t}\right) \tag{2.9}$$

with α the Gilbert damping parameter and $M_S = |\mathbf{M}|$ the constant norm of the magnetization vector. The LLG equation can be transformed back to a form similar to the LL equation by replacing the last time derivative of $\mathbf{M}$

by the whole right-hand side in Eq. (2.9), giving

$$\frac{\partial \mathbf{M}}{\partial t} = -\frac{\gamma}{1+\alpha^2}\mu_0 \mathbf{M} \times \mathbf{H_{eff}} - \frac{\alpha\gamma\mu_0}{M_S(1+\alpha^2)}\mathbf{M} \times (\mathbf{M} \times \mathbf{H_{eff}}) \tag{2.10}$$

where the relations between the coefficients in the LL and LLG equations appear clearly, notably with γ being renormalized by $\left(1+\alpha^2\right)$.

The effective field term $\mu_0\mathbf{H_{eff}}$ should actually incorporate all the magnetic interactions within the system. It is deduced from the energy of the system. Considering the magnetization $\mathbf{m}(\mathbf{r})$ at a position $\mathbf{r}$, we define

$$\mathbf{H_{eff}} = -\frac{1}{\mu_0 M_S}\frac{d\varepsilon_{tot}}{d\mathbf{m}}, \tag{2.11}$$

which gives the effective field locally felt by the magnetization. In $\mu_0\mathbf{H_{eff}}$, the fields originating from all energy contributions are to be linearly added, namely,

- the field originating from exchange energy interaction $\mu_0\mathbf{H_{ex}}$, locally given by

$$\mathbf{H_{ex}} = \frac{2A}{\mu_0 M_S}\nabla^2\mathbf{m}; \tag{2.12}$$

- the field originating from the DMI $\mu_0\mathbf{H_{dmi}}$, locally given by

$$\mathbf{H_{dmi}} = \frac{2D}{\mu_0 M_S}\left(\left(\frac{\partial \mathbf{m}\cdot\hat{\mathbf{z}}}{\partial x}\right)\hat{\mathbf{x}} + \left(\frac{\partial \mathbf{m}\cdot\hat{\mathbf{z}}}{\partial y}\right)\hat{\mathbf{y}} - \left(\frac{\partial \mathbf{m}\cdot\hat{\mathbf{x}}}{\partial x} + \frac{\partial \mathbf{m}\cdot\hat{\mathbf{y}}}{\partial y}\right)\hat{\mathbf{z}}\right); \tag{2.13}$$

- the demagnetizing field $\mu_0\mathbf{H_d}$, as defined in §2.1.3;

- any external magnetic field $\mu_0\mathbf{H_{ext}}$ interacting with the magnetic system (due to the Zeeman energy);

- the anisotropy field $\mu_0\mathbf{H_{ani}}$ due to the magnetic anisotropy, which is a function of the magnetization direction $\mathbf{m}$ at $\mathbf{r}$ only. For example, keeping only the K_2 term, we get

$$\mathbf{H_{ani}}(\mathbf{m}) = \frac{2K_2}{\mu_0 M_S}(\mathbf{m}\cdot\hat{\mathbf{u}})\hat{\mathbf{u}}. \tag{2.14}$$

2.3 The macrospin description

Solving numerically Eq. (2.9) for a system discretized into a mesh of finite elements/finite differences, also called micromagnetics, is now easy to perform thanks to the recent progresses in computational power. Such simulations are extremely useful to accurately predict the behaviour of ferromagnetic systems, and will be performed in Chapter 4 to study current-induced switching by spin-orbit torques. In the present chapter, which is only an introduction to the dynamics of magnetic systems, we rather aim at giving a simplified, but physically transparent model to account for the time-domain dynamics of ferromagnets, and apply this model to a basic situation. The simplest assumption that can be done is to consider the magnetization to be uniform inside the whole magnetic body. Such a macrospin approximation is quite realistic for small, monodomain ferromagnets due to their dominating exchange interaction. For the larger magnets however, the picture will unavoidably be inaccurate. However, this oversimplified model is still useful for finding different qualitative behaviours or approximating critical limits of some switching events. As explained above, the modulus of the magnetization is constant over time, hence we are only interested in the direction of $\mathbf{m}$. As $\mathbf{m}$ is considered uniform, the system owns only two degrees of liberty

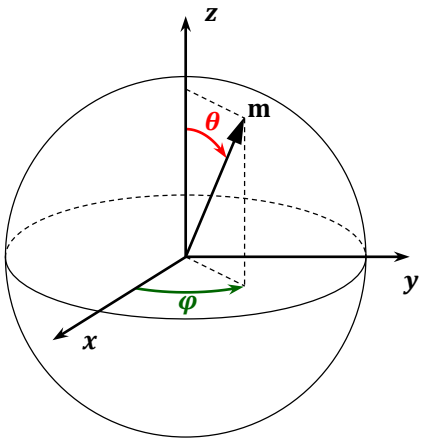

Figure 2.2: Coordinate system and angles: $\mathbf{m}$ is entirely described by the polar angle θ and the azimuthal angle φ.

and is then entirely determined by the position of $\mathbf{m}$ on the unit sphere: the definitions of the two spherical coordinate angles θ and φ describing $\mathbf{m}$ will be kept all along this thesis and are defined in Fig. 2.2. To get some insight into the general form of the solutions of the LLG equation (Eq. (2.9)), we will now cover two common situations: (i) the magnetic relaxation due to anisotropy in the absence of external torques, and (ii) the simplest scheme of spin-transfer torque switching.

We first consider a large ($N_z = 1$), uniformly magnetized thin layer with an interfacial anisotropy perpendicular to the plane ($\hat{\mathbf{u}} = \hat{\mathbf{z}}$) with second order angle dependence only ($K_4 = 0$), as can be found in spin-valves or MTJs. We consider $2K_2 > \mu_0 M_S^2$ so that the magnetization ground state is out-of-plane, as found by comparing Eqs. (2.5) and (2.7). Finding the effective field using Eq. (2.11) and eliminating M_S on both sides, one gets in the absence of any other interactions

$$\frac{d\mathbf{m}}{dt} = -\gamma\mu_0 H_{ani} cos(\theta)\mathbf{m} \times \hat{\mathbf{z}} + \alpha\left(\mathbf{m} \times \frac{d\mathbf{m}}{dt}\right) \tag{2.15}$$

where $H_{ani} = 2K_2/(\mu_0 M_S) - M_S$ is the effective anisotropy finally resulting from both demagnetizing fields and interface interactions. From this dynamic equation, the same two stable positions can be derived from energy minimisation of ε_{tot}, which are $+\hat{\mathbf{z}}$ and $-\hat{\mathbf{z}}$. If the initial magnetization differs from $\pm\hat{\mathbf{z}}$, $\mathbf{m}$ will relax to the closest one by a damped precession around the vertical axis, as shown in Fig. 2.3a, drawn by solving Eq. (2.15).

In the case of spin-transfer torque switching, a spin-current of polarization different from the local magnetization is passed through the FM layer and can possibly switch it due to the torque exerted by this current, called the Slonczewski torque. In a spin-valve for example, which can be in the P or AP states, we are interested in the dynamics of the free layer initially magnetized along $+\hat{\mathbf{z}}$. The current is spin-polarized by the other electrode (the pinned layer) along $\hat{\mathbf{p}} = -\hat{\mathbf{z}}$. In a simple modelling, assuming the full absorption of the spin-current, the Slonczewski torque is given as an additional term in the LLG equation so that

$$\frac{d\mathbf{m}}{dt} = -\gamma\mu_0 H_{ani} cos(\theta)\mathbf{m}\times\hat{\mathbf{z}} + \alpha\left(\mathbf{m}\times\frac{d\mathbf{m}}{dt}\right) + \gamma a_J \mathbf{m}\times(\hat{\mathbf{p}}\times\mathbf{m}) \quad (2.16)$$

where

$$a_J = \frac{\hbar}{2e}\frac{\eta J}{M_S t_{FM}} \quad (2.17)$$

is the strength of the spin torque. The additional Slonczewksi term accounts for the exchange interaction between polarized conduction electrons and the local magnetization [9, 20, 21]: J is the current density, η the polarization of the spin current, and t_{FM} the thickness of the FM layer. As can be seen from the trajectory solution of Eq. (2.16) drawn in Fig. 2.3b, the Slonczewski torque drives $\mathbf{m}$ away from $+\hat{\mathbf{z}}$ during its precession around the

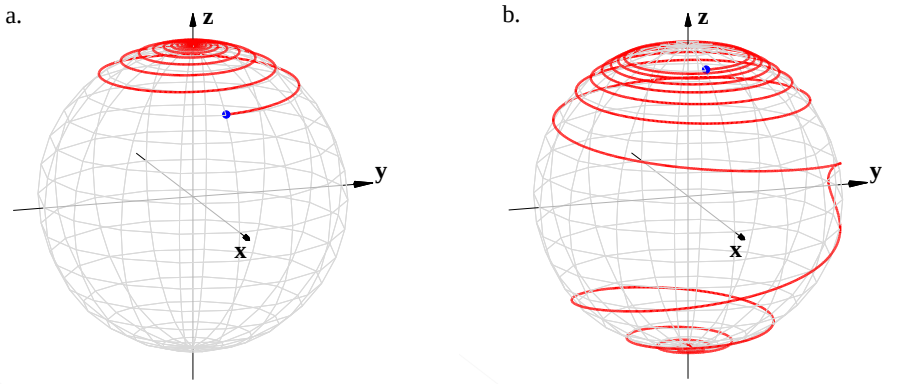

Figure 2.3: Solution trajectories of the Landau-Lifshitz-Gilbert (LLG) equation in the macrospin approximation. a. Typical solution of Eq. (2.15) for an arbitrary initial position (blue dot). b. Typical solution of Eq. (2.16) for an arbitrary initial position (blue dot). In each graph, the red curve is the time evolution of $\mathbf{m}$ on the unit sphere.

vertical direction and helps it to switch to $-\hat{\mathbf{z}}$ by crossing the xy plane.

In this chapter, we have progressively introduced the different magnetic interactions and mechanisms affecting the dynamics of the magnetization in ferromagnetic systems. We have discussed the dynamics in two essential cases: the magnetic relaxation in the absence of currents and the spin-transfer torque switching. We are now ready to approach the main interest of this thesis' work, which deals with spin-orbit-torque-induced dynamics.

Chapter 3
Magnetization switching by spin-orbit torques

In this chapter, we first briefly review the origins of the spin-orbit torques in the most commonly studied system based on heavy-metals (§3.1). As we will see, the spin-orbit torques have particularly interesting properties when they are combined with a uniaxial perpendicular anisotropy. We therefore introduce a systematic study of the phase diagram of the equilibrium solutions of such a system, both under and in the absence of currents (§3.2), which will allow us to describe accurately the switching processes in the following chapters. A review of the understanding of the spin-orbit-torque-induced switching processes is then given in §3.3, before we formulate our approach for the next chapters and applications to spin-orbit-torque-driven magnetic memories (§3.4).

3.1 Origins of spin-orbit torques in magnetic multilayers

Due to relativistic effects in the motion of the electrons in solids, there is a coupling between the spin of the electron and its orbital moment. This spin-orbit interaction is the origin of a means of getting a spin-polarization from a charge current as it couples the crystalline momentum and the spin states, and, therefore, the magnetization. This results in what are called spin-

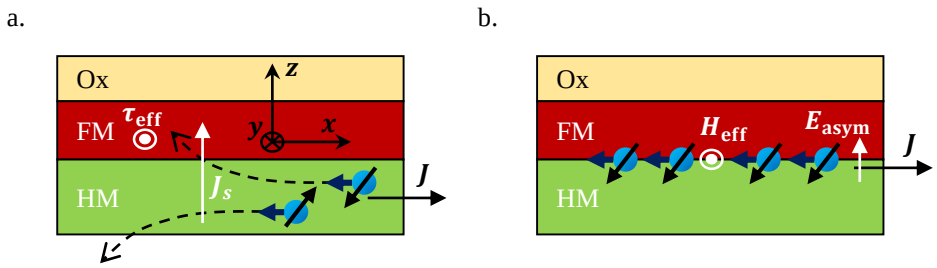

Figure 3.1: a. Schematic picture of the spin-Hall-effect-induced torque, displaying charge current density vector $\mathbf{J}$, spin Hall effect on carrier motion (dashed lines) depending of the electron spin (short black arrows), spin current $\mathbf{J_s}$, and effective torque $\tau_{\mathbf{eff}}$. b. Schematic picture of the Rashba-effect-induced-torque, displaying electron spin-polarization (short black arrows) at the HM/FM interface originating from the symmetry-breaking electric field $\mathbf{E_{asym}}$ and resulting in the effective field $\mathbf{H_{eff}}$.

orbit torques (SOTs). Materials known to exhibit a large spin-orbit coupling and thus large SOTs are, so far, pure [22] or alloyed [23, 24] heavy-metals, two-dimensional electron gases at insulator interfaces [25], semiconductors [26], topological insulator surfaces [27–30], graphene [31], etc. For this work, we will only cover the generation of SOTs in magnetic multilayers incorporating heavy-metals (HMs). We will then often compare SOTs in these systems to STTs in similar magnetic multilayers, allowing for a common comparison ground for the dynamics. The origins of SOTs in HM/FM/oxide[1] heterostructures are still a subject of intense debate: some mechanisms are clearly identified but the roles of each of them in the generation of the final resulting torques remains unclear. Nevertheless, we can mainly distinguish (i) the spin Hall effect [22] and (ii) the Rashba spin-orbit coupling [32, 33].

In the case of the spin Hall effect (Fig. 3.1a), the charge current $\mathbf{J}$ generates a spin current $\hbar/(2e)\mathbf{J_s}$ in the direction perpendicular to the interface [34, 35]. The injected spin-polarized electrons will interact with the magnetization of the FM and exert a torque $\tau_{\mathbf{eff}}$, exactly as in the case of STT.

[1] the oxide layer was originally introduced to protect the FM layer from alteration due to its environment, and may or may not have an effect on the torques

In this situation, the effective torque may be strongly affected by the transparency of the HM/FM interface [36, 37]: if the spin-current generated in the HM cannot pass through the interface, it cannot have an effect on the magnetization. The direction as well as the strength of the spin Hall effect is evaluated by the spin Hall angle θ_{SH}, defined as the ratio of the transverse spin current on the charge current

$$\theta_{SH} = \frac{J_s}{J}. \tag{3.1}$$

For a current J flowing in the x direction (as defined in Fig. 3.1a), a positive spin angle indicates that the top surface of the HM gets a spin-polarization opposite to $\hat{\mathbf{y}}$. For instance, Pt has a positive θ_{SH} of about 0.08–0.3 depending on the interfacial effects affecting the measurements [37, 38], while Ta and W have negative θ_{SH} of about 0.15–0.24 [22, 39] and 0.3–0.4 [40, 41], respectively.

The Rashba effect (Fig. 3.1b) occurs in materials lacking inversion symmetry, where the symmetry breaking at the HM/FM interface creates an electric field $\mathbf{E_{asym}}$ that will interact with the electron motion due to the Rashba spin-orbit coupling [42–44]. This results in an effective field $\mathbf{H_{eff}}$, parallel to the surface and perpendicular to the current, that exerts a torque on the magnetization inside the FM [45]. The Rashba effect is considered to allow SOTs of the same amplitude as the ones originating from the spin Hall effect [46].

Some systems may exhibit only one of these effects, while some other material combinations may show both. Some theories have tried to combine the two mechanisms into one consistent model to evaluate the roles of both spin

Hall effect and Rashba spin-orbit coupling [47, 48] in SOTs. For example, in Ta/CoFeB structures, a recent study found some evidence for the presence of both mechanisms [49]. The torques have both an interface and a bulk origin inside the HM [50, 51]. In these models, it has been found that the SOTs affect the magnetization dynamics in two different ways [39, 52–54]: one very similar to the Slonczewski torque except that $\hat{\mathbf{p}}$ is being replaced by the spin polarization of the injected electrons, $\hat{\sigma} = -\hat{\mathbf{y}}$, and the other one similar to a field directed along $\pm\hat{\mathbf{y}}$. To get the effects of the spin-orbit torques on the equilibrium and dynamics, we replace the STT term given by the last term in Eq. (2.16) by two SOT terms, the Slonczewski-like and the field-like torques, which are given by

$$\tau^{\parallel} = \frac{\gamma\hbar}{2e}\frac{c^{\parallel}J}{M_S t_{FM}}\mathbf{m}\times(\hat{\sigma}\times\mathbf{m}) \tag{3.2}$$

and

$$\tau^{\perp} = \frac{\gamma\hbar}{2e}\frac{c^{\perp}J}{M_S t_{FM}}(\hat{\sigma}\times\mathbf{m}), \tag{3.3}$$

respectively. In Eqs. (3.2) and (3.3), we denote the Slonczewski- and field-like torque coefficients by $c^{\parallel}$ and $c^{\perp}$, respectively. The simple-minded thought that the spin Hall effect would be the origin of the Slonczewski-like torque while the Rashba effect would be the source of the field-like torque is tempting. However, even if this assumption may hold in some particular cases, there is no reason for such a separation to exist when we have a closer look at the torque mechanisms. In general, we need to consider that both mechanisms can generate both forms of torque, as can be understood from the various models describing the SOTs [46, 48]. As a consequence, $c^{\parallel}$ may strongly differ from θ_{SH}, which partly explains the strong controversy on its

value in some systems [22, 39, 52, 55]. Moreover, both $c^{\parallel}$ and $c^{\perp}$ can be modulated by extrinsic parameters such as the spin diffusion length [56], interface quality [37] or electric field [57]. From now on, the term Slonczewski torque will only refer to the spin-orbit-originated Slonczewski-like torque.

3.2 Perpendicular magnetic anisotropy and spin-orbit torques

As we can see from Eqs. (3.2) and (3.3), the SOT magnetization dynamics are induced by an in-plane spin polarization. This situation is analogous to the case of the orthogonal-STT [58] scheme developed as an improvement of the STT scheme. In the orthogonal-STT, the spin valve is kept where the pinned layer and the free layer have their magnetization perpendicular to the plane, but a polariser layer whose magnetization is in-plane is added to the other side of the free layer. As a consequence, the injected spin polarization inside the free layer is rather in-plane than out-of plane. This avoids the cancellation of the torque in the P and AP configurations [the torque is zero if we put $\mathbf{m} = \pm\hat{\mathbf{p}}$ in Eq. (2.16)]. As we can see from Fig. 2.3b, the STT-induced magnetization switching is not direct but proceeds through many precessions because of this cancellation of the torque near the P and AP equilibrium positions: the switching needs to be initiated by thermal excitations away from the equilibrium[2]. On the contrary, when the spin-polarization is in-plane, direct and much faster and reliable switching is demonstrated [59]. Also, the perpendicular magnetic anisotropy allows further downscaling of the magnetic system while keeping its thermal stability [60]. For these reasons, it is interesting to combine perpendicularly

[2]that means that no switching is expected at 0K

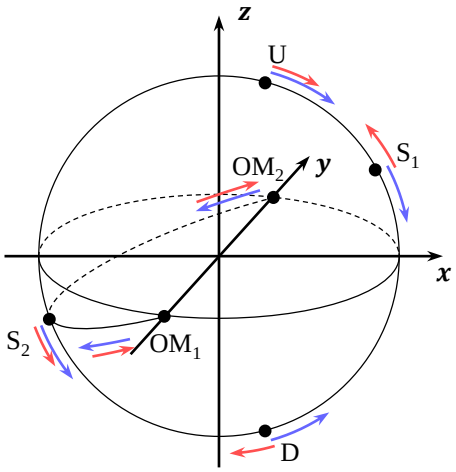

Figure 3.2: The different equilibria U, D, S_1, S_2, OM_1 and OM_2 are shown on the unit sphere. The blue and red arrows indicate their field-induced and spin-orbit-torque-induced displacements. Adapted from [61].

magnetized materials with the spin-orbit torques generated in a HM layer. In terms of magnetic states, this configuration gives rise to more equilibrium positions for $\mathbf{m}$ than in the STT scheme. Before we describe the switching process, we will first identify and name these equilibria, as analysed in a macrospin model by Yan et al. [61], which will be extremely useful in our investigations.

Under the macrospin approximation, it is possible to study analytically the LLG equation [(2.16)] after replacing the STT term by the SOT terms, in order to find the equilibria in the unixaial perpendicular magnetic anisotropy system. As the field-like torque acts exactly as a field in the y direction, the inclusion of the field-like torque term to find the equilibria under constant current or no current is not necessary. Also, $c^{\parallel}$ is taken to be positive. These equilibria are given by the solutions of $\mathbf{H_{eff}} = \lambda \mathbf{m}$, λ being a scalar coefficient expressing the collinearity of the two vectors. We can then further distinguish the stable and unstable equilibria by looking at the solutions for small deviations after linearising Eq. (2.16) around the previously found

equilibrium positions of **m**. We describe the positions of the equilibrium positions on the unit sphere with θ and φ defined in Fig. 2.2 when a field and/or a current can be applied in the x direction. In this case, Yan et al. [61] list three different kinds of equilibria (refer to Fig. 3.2):

- two stable equilibria U and D lying in the xz plane. They verify $\phi = 0$. They are the intuitive 'up' ($\theta = 0$) and 'down' ($\theta = \pi$) stable positions in the absence of currents, and can disappear by merging with the saddle points defined next, depending on applied current and field;

- two saddle points, S_1 in the one hemisphere ($x > 0$) and S_2 in the other hemisphere ($x < 0$);

- and two equilibria lying away from xz plane, referred to as OM_1 and OM_2. They obey a symmetry with regard to xz plane, and share the same polar angle θ with opposite azimuthal angle φ and $-\varphi$, respectively.

In the small current regime, the system has then six equilibrium positions, but only U and D are stable. The effect of the applied field in the x direction is to break the symmetry of the system, so that reversing the current and hence the Slonczewski torque does not give the symmetric equilibria. When the current is increased, U and D are displaced clockwise while S_1 and S_2 shift counter-clockwise along the xz meridian, and OM_1, OM_2 approach $\pm\hat{\mathbf{y}}$ (red arrows in Fig. 3.2). Increasing the field displaces U, D, S_1 and S_2 in the direction of the field, OM_1 and OM_2 in the direction opposite to it (blue arrows in Fig. 3.2). Finally, note that OM_1 become stable at larger positive currents [61].

3.3 Switching processes

In this section, we are interested in the switching processes of perpendicularly magnetized FMs through spin-orbit torque, as demonstrated experimentally in Refs. [62, 63]. We want to determine the switching behaviour of $\mathbf{m}$ when a current is sent for a finite-time.

We first give an explanation based on the macrospin model. As can be seen from the diagram of Fig. 3.2, the equilibria of each pair U/S_1 and D/S_2 get closer when the current is increased. When the torque is large enough, these equilibrium merge and disappear. The magnetization then has to switch to another stable state. In the absence of an applied field, both positions U and D are suppressed concurrently and hence $\mathbf{m}$ switches to the OM_1 position (stable under currents). When the current is reduced to zero, OM_1 becomes unstable and $\mathbf{m}$ has to switch to a stable position again: as the starting point of this relaxation phase is perfectly in-plane, one cannot predict the final state between U or D, that will be decided by the random thermal fluctuations. The switching is therefore non-deterministic.

However, when a field is applied in the x direction, it becomes possible to achieve deterministic switching as the symmetry of the system is broken. Consider that an external field is applied parallel to $+\hat{\mathbf{x}}$. As can be visualized on Fig. 3.2, due to the influence of the field, the pair U/S_1 will merge for a lower current than the pair D/S_2. After suppressing U/S_1, $\mathbf{m}$ can proceed to either D or OM_1, depending on their stabilities. Even if the current is increased, resulting in $\mathbf{m}$ being stabilized at OM_1, the switching is still deterministic because OM_1 is displaced away from the xy plane by the in-plane field. In the present case, $\theta > \pi/2$ so that when the current is reduced,

m relaxes from a position where $m_z < 0$ and ends at the switched position D. Reversing either the current or the field allows the opposite switching operation (from D to U).

In the explanation above, it is implicit that all parameters are modified quasi-statically: the current is not a pulse with short rising and falling edges but is progressively applied, so that the behaviours of the equilibria dominate the process. Dealing with the dynamics of the reversal process will be the focus of Chapter 4, but we already note here that the dynamic behaviour can totally differ from the quasi-static evolution. The reversal process through the intermediary OM_1 state has been discussed numerically by macrospin simulations [64]. Some full micromagnetic simulations later confirmed that this process is expectable and not originating from the approximations of the macrospin model [65]. If the current density is chosen in the proper window, one can observe direct switching (U to D or D to U). The macrospin model then gives in these two cases an intuitive picture of the SOT-induced switching phenomenon, but remains oversimplified. A first limitation is that it does not take into account the field-like torque. Another limitation is that assuming a uniform magnetization excludes the influence of some magnetic interactions, notably the DMI, which exerts a crucial influence for some material combinations, as we explain below.

The field-like torque has been evidenced to be of a large magnitude in diverse systems, and can be even a couple times larger than the Slonczewski torque, notably when the HM is Ta [39, 52, 53, 66]. Because it shifts the U and D positions away from the xz plane, it affects the energy landscape and can favourably or unfavourably affect the switching currents [67]. We also note that the field-like torque will affect the behaviour of the OM_1

equilibrium.

The switching process explained above is well describing the case of a very small ferromagnet that will exhibit coherent magnetization switching and closely follow the macrospin behaviour. This regime is expected to occur when the size of the magnet is of the order of the size of the domain-wall or below, which roughly corresponds to 25–50 nm for perpendicularly magnetized materials [68, 69]. However, for larger systems, another switching process is expected to occur, through nucleation and propagation [70–72]: a small part of the magnet is first reversed and creates a DW, which is pushed by the field and SOTs so that the magnetization reverses everywhere. Such a switching process is, for example, expected in Pt-based systems as the Pt/FM interface creates a large DMI. The DMI favours non-uniform magnetic configurations even more than the demagnetizing fields inside the system. Notably, it is energetically favourable that the edges of the system be tilted outwards or inwards depending on the sign of the DMI in the U or D states. This tilting being added to the one originating from the in-plane field, one side is favoured for nucleation. Switching is therefore possible only in one direction while the opposite switching event is prevented, ensuring a deterministic reversal [71]. Micromagnetic simulations have shown this process to occur even in the short pulse regime [69].

It is worth mentioning here that SOTs—exactly like STTs—do not only allow magnetization switching as shown above, but also provide many other ways of manipulating the magnetic order, among which we can name, for instance, high-velocity domain wall motion, modulation of the magnetization precession, spin-wave generation, etc. This list is far from being exhaustive, as some new possibilities raised by the SOTs are still regularly unveiled. We

will not cover them into details, as this thesis intends to focus on magnetization switching among all the new prospects offered by SOTs. However, some of the different concepts formulated in the following chapters can hopefully be translated to other techniques based on SOTs.

3.4 Spin-orbit-torque-driven magnetic memories

The previous sections briefly exposed the state of the present knowledge of the SOT-induced magnetization switching processes in perpendicularly magnetized FMs. This switching scheme has numerous advantages over the STT scheme. As revealed by the study of the equilibrium positions in §3.2, switching is not obtained from destabilizing an equilibrium but from suppressing it. As a consequence, unlike the STT scheme, the magnetization does not precess around the destabilized equilibrium before it switches, but directly moves towards the new equilibrium position in a time shorter than the precession period. For comparison, the reader may refer to Ref. [73] to get a detailed and up-to-date description of the spin-transfer torque reversal processes in devices. This direct switching is superior to precessional switching in terms of speed and therefore, energy efficiency, as a current is required for a shorter time [74, 75]. Under some conditions that we have seen in §3.3, the switching can be deterministic, as it is in the STT case.

Another considerable advantage of this configuration is that the current is flowing in the plane of the HM/FM layers. As a consequence, the writing current in a spin-valve SOT-based memory cell does not need to flow through the insulating barrier of the MTJ, and a three-terminal device can be build [76], thus avoiding excessive ageing and damaging of the insulator. In this case, only a small current needs to flow through the barrier for reading,

ensuring its reliability over many operation cycles.

Given these strong motivations, it comes as no surprise that a lot of research is directed towards developing SOT-based memories. However, some different issues are still to be tackled before SOTs can be effectively used in memory devices. First, the dynamical regime of the reversal process is still complex as it cannot be easily described by the simple model presented above: in many cases, deterministic dynamic switching—in one nanosecond or less—remains difficult. Notably, the roles of the different torques need to be further identified. Second, the requirement for an external field to be applied to the device is a drawback regarding the practical interest of SOTs: it is possible to integrate a magnet in the layers stack to create such a field, but this approach requires much more engineering of the materials and is hardly scalable. Two recent studies proposed alternative ways to replace the external magnetic field. One is based on a broken lateral inversion asymmetry with the deposition of wedged layers [77]. Another proposal is to engineer a tilted magnetic anisotropy by diagonal etching of the oxide layer [78]. Although effective, these methods require the same amount of or even more engineering to achieve SOT switching without external field.

Dealing with these two concerns being the object of this work, Chapter 4 is dedicated to an exploration of the influence of the field-like torque in the dynamic regime. Notably, it will reveal an efficient switching scheme free of external magnetic fields. Chapter 5 will push forward the theoretical description of the thermally-induced switching processes in the presence of the field-like torque. It can be used in order to study the different current-induced torque terms. Chapter 6 investigates SOT switching in triaxial anisotropy systems. With a simple modification of the device geometry, it is able to

allow for a simple way of obtaining deterministic switching in the absence of external fields.

Chapter 4

Dynamic spin-orbit torque switching without external fields

In this chapter, we study the influence of the field-like torque on the regime of dynamic switching. In §4.1, we analyse qualitatively the roles of both Slonczewski and field-like torques in comparison with their quasi-static behaviour. By solving numerically the equation of motion of the magnetization in the macrospin approximation, it will be shown that in the dynamic regime the interplay of both torques offers an efficient way of switching the magnetization deterministically without the requirement for any external magnetic field (§4.2). The essential role of the rising time of the pulse is studied in §4.3. The switching times will be analysed in §4.4, where the influence of the anisotropy will be considered. In §4.5, we validate our approach by micromagnetic simulations in order to demonstrate the concept in realistic systems. Finally, §4.6 summarizes the significance of this study.

4.1 Nature of the Slonczewski and field-like torques

We begin by analysing the respective behaviours of the Slonczewski and field-like torques in the dynamic regime. We consider the magnetization to obey a macrospin behaviour: this assumption is relevant in the small magnets of 50×50 nm^2 or less, which are of most interest for applications. We describe the evolution of the magnetization by the direction of $\mathbf{m}$ in the

LLG equation [Eq. (2.9)] to which we add the Slonczewski [Eq. (3.2)] and field-like [Eq. (3.3)] torques. An external field H_x can be applied in the x direction. In order to get analytical results, we rescale the terms of Eq. (2.9) in order to obtain a convenient, dimensionless equation of motion. The Slonczewski and field-like torque effective fields are given by

$$H^{\parallel,\perp} = \frac{\hbar}{2e}\frac{c^{\parallel,\perp}J}{\mu_0 M_S t_{FM}}. \tag{4.1}$$

We introduce the values of the effective fields rescaled by the anisotropy with the dimensionless $h_x = H_x/H_{ani}$, $h^{\parallel} = H^{\parallel}/H_{ani}$ and $h^{\perp} = H^{\perp}/H_{ani}$. The time is also rescaled by the natural time unit $t' = \gamma\mu_0 H_{ani} t$ so that we get the dimensionless equation

$$\frac{d\mathbf{m}}{dt'} = (h_x\hat{\mathbf{x}} + \cos\theta\hat{\mathbf{z}}) \times \mathbf{m} + \alpha\mathbf{m} \times \frac{d\mathbf{m}}{dt'} + h^{\parallel}(\mathbf{m} \times \hat{\sigma}) \times \mathbf{m} + h^{\perp}\hat{\sigma} \times \mathbf{m}. \tag{4.2}$$

We finally introduce the characteristic current density

$$J_0 = \frac{2e}{\hbar}\mu_0 M_S t_{FM} H_{ani} \tag{4.3}$$

so that a torque efficiency of 1 results in an effective SOT field of the same strength as the anisotropy field H_{ani} for $J = J_0$. To get exemplary numerical results, we fix for later in this chapter $M_S = 1500$ emu cm^{-3}, $t_{FM} = 1.6$ nm, $H_{ani} = 1000$ Oe. With these realistic parameters, the characteristic current density is $J_0 = 7.28 \times 10^7$ A cm^{-2}, which is experimentally accessible.

The form of the field-like torque in Eq. (4.2) already reveals that it causes the precession of $\mathbf{m}$ around $\hat{\sigma}$: as a consequence, it should be able to induce switching by making $\mathbf{m}$ cross the xy plane [79]. Even if the field-like

torque is not expected to allow quasi-static switching for symmetry reasons, it could allow to switch **m** in the dynamic regime. However, most works in the literature modelled the SOT switching only considering the Slonczewski torque [64, 80]. Another work was focused on small macrospin nanodots like here, but it considered a small field-like torque only in the presence of an external field [81]. In this chapter, we will consider a field-like torque potentially much larger than the Slonczewski torque, as found in some recent experiments [39, 52–54]. We will also eventually remove the assist-field.

We can distinguish between the quasi-static and the dynamic regimes depending on the rising time of the applied current pulse. As we have introduced the natural time unit, it can be seen easily from Eq. (4.2) that in the absence of current-induced torques and external fields, the period of one precession for a simple relaxation around the perpendicular easy-axis is 2π. This time is the characteristic time for the system to follow the externally applied torques. Denoting the rising/falling time of the current impulsion by t'_{rise}, the system will obey a quasi-static evolution if $t'_{rise} \gg 2\pi$. In this case, we are interested in the evolution of the equilibrium positions, which is influenced by the effective fields, so that $h^{\parallel}$ and $h^{\perp}$ are more relevant to the problem. However, if $t'_{rise} \ll 2\pi$, **m** will not follow the equilibria but will lag behind them, which in turn generates some precession around the new equilibria. The final position may be totally different and in this case it is relevant to look at the torques $\tau^{\parallel}$ and $\tau^{\perp}$.

These behaviours are summarised in Fig. 4.1. To obtain the switching trajectories, we solve Eq. (4.2) numerically with a damping parameter $\alpha = 0.01$, and draw the time evolution of **m** on the unit sphere in red during the pulse (including the rising edge), and in blue after the pulse (relaxation phase,

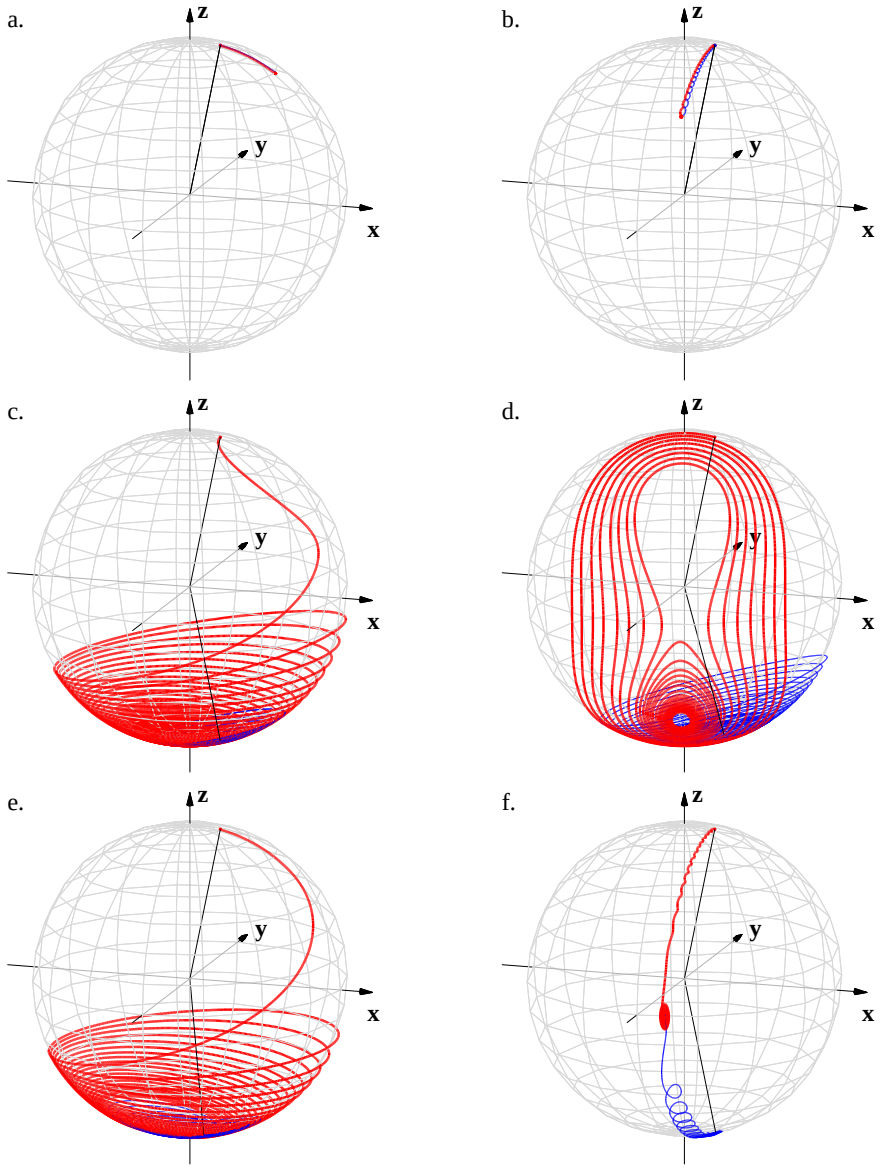

Figure 4.1: Differences between the Slonczewski and field-like torques in the quasi-static and dynamic regime. An in-plane assist field $h_x = 0.2$ is applied. a. $t'_{rise} = 40\pi$, $h^{\parallel} = 0.3$ and $h^{\perp} = 0$. b. $t'_{rise} = 40\pi$, $h^{\parallel} = 0$ and $h^{\perp} = 0.7$. c. $t'_{rise} = 0$, $h^{\parallel} = 0.3$ and $h^{\perp} = 0$. d. $t'_{rise} = 0$, $h^{\parallel} = 0$ and $h^{\perp} = 0.7$. e. $t'_{rise} = 40\pi$, $h^{\parallel} = 0.4$ and $h^{\perp} = 0$. f. $t'_{rise} = 40\pi$, $h^{\parallel} = 0$ and $h^{\perp} = 1.1$. In each case, the red curve corresponds to the time evolution of $\mathbf{m}$ during the current pulse, and the blue curve corresponds to its relaxation.

including the falling edge). The thermal perturbations are not considered in this chapter. A pulse much longer than 2π is applied in each case, but the rising time can be either 40π implying a quasi-static evolution, or 0 (ideally short) implying a dynamic regime. An assist field is applied in the x direction in order to break the symmetry, which allows preferential U to D switching.

In Fig. 4.1a, one can see the effect of the Slonczewski torque in the quasi-static regime. As $h^{\parallel} = 0.3$ is not large enough to induce the switching, $\mathbf{m}$ follows the U equilibrium slowly displaced by the Slonczewski effective field $h^{\parallel}$ in the x direction, and slowly returns towards its initial position during the relaxation phase. Similarly, as shown in Fig. 4.1b, the field-like torque $h^{\perp} = 0.7$ shifts the equilibria towards $\hat{\sigma}$.

Even if these torques are not sufficient to switch the magnetization quasi-statically, the magnetization switches for the same torques in the dynamic regime, as can be seen from Figs. 4.1c,d for the Slonczewski and the field-like torque, respectively. This is because when the effective fields are changed faster than the characteristic time for precession, $\mathbf{m}$ is still located at its initial position when the maximum torque is already applied. In this case, instead of following the displaced equilibria, $\mathbf{m}$ rotates around it, which potentially allows switching by precession. Along the switching trajectory, the Slonczewski torque $h^{\parallel}$ is directed towards $\hat{\sigma}$ and can lead to direct switching to the intermediate state OM_1 (not shown), or in the case where h_x is sufficient like here, to a precessional switching to D (Fig. 4.1c). The field-like torque has the same action as a field: as a consequence, $\mathbf{m}$ precesses around the effective field $h_x\hat{\mathbf{x}} + h^{\perp}\hat{\sigma}$ (Fig. 4.1d). Finally, Figs. 4.1e,f display the quasi-static switching event, with $h^{\parallel} = 0.4$ and $h^{\perp} = 1.1$, respectively. While the action of the Slonczewski torque is to suppress the U position, which leads to switching through a relaxation around D (Fig. 4.1e), the field-like torque rather causes the merging of the U and D equilibria. Due to the assist field, one direction of switching is favoured during the quasi-static relaxation (Fig. 4.1f). Nevertheless, as the starting point of the relaxation is in-plane, the real behaviour would be randomized by the thermal fluctuations

of the system.

From these examples, we can see that on the one hand, the Slonczewski torque is able to provide both quasi-static and dynamic deterministic switching, but it requires an assist-field. If, on the contrary, there is no assist field, $\mathbf{m}$ moves under current to OM_1, which is aligned with $\hat{\sigma}$ as the symmetry is not broken: the final position after the random relaxation from the plane cannot be predicted. On the other hand, the field-like torque is able to generate some precession around $\hat{\sigma}$ in the dynamic regime, even without assist field. However, the final position after the many precession that occur cannot be reliably predicted (in Fig. 4.1d, it could be U as well, depending on small variations of the parameters and thermal fluctuations) and switching is not deterministic. Neither of the two torque terms allows for a reliable switching without assist field. As we will explain in the next section, the combination of these two torques provides a mean of reliably switching the magnetization without external fields in a fast, dynamic regime.

4.2 Varying the torques ratio

The main difference between the quasi-static regime and the dynamic regime is that for the latter, the energy background for $\mathbf{m}$ is modified instantaneously and before $\mathbf{m}$ starts any motion. We first consider the presence of a field-like torque only, in a dissipationless system. The lag of $\mathbf{m}$ behind the equilibria raises the energy of the system relatively to the new energy minima, so that $\mathbf{m}$ precesses around the displaced equilibria on an orbit of equal energy. As the field-like torque corresponds to a field applied parallel to $\hat{\sigma}$, both U and D positions are displaced on the yz meridian ($\varphi = -\pi/2$) towards $\hat{\sigma}$, at $\theta = \arcsin h^{\perp}$ and $\theta = \pi - \arcsin h^{\perp}$, respectively. For $\mathbf{m}$ start-

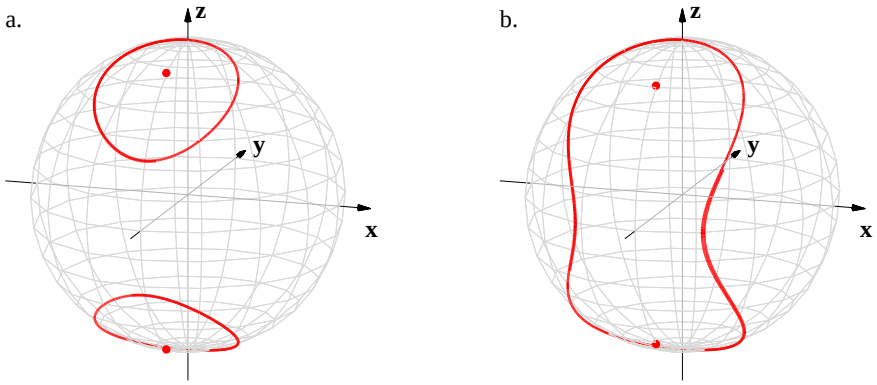

Figure 4.2: Isoenergetic orbits under the influence of the field-like torque in the dynamic regime. The dissipation of the system is suppressed ($\alpha = 0$). a. $t'_{rise} = 0$, $h^{\parallel} = 0$ and $h^{\perp} = 0.45$. b. $t'_{rise} = 0$, $h^{\parallel} = 0$ and $h^{\perp} = 0.55$. In both cases, the isoenergetic orbits for $\mathbf{m}$ starting from $\pm\hat{\mathbf{z}}$ are shown. The displaced U and D equilibria are indicated by the red dots.

ing from U or D, it will precess around the displaced U and D equilibrium, as shown in Fig. 4.2a. However, a change in the behaviour occurs when the field-like torque is sufficiently strong. In this case, as shown in Fig. 4.2b, the two isoenergetic orbits starting from $\pm\hat{\mathbf{z}}$ and winding around the displaced U and D equilibria (represented by the red dots) become large enough to merge together. Therefore $\mathbf{m}$ follows a large orbit which conjugates both U and D equilibria by winding around them as well as OM_1. The two orbits merge when the homoclinic orbits starting from the non-stable equilibrium OM_1 located at $\hat{\sigma}$ reach $\pm\hat{\mathbf{z}}$. This gives us the condition $\varepsilon(\pm\hat{\mathbf{z}}) = \varepsilon(\hat{\sigma})$, verified for $h^{\perp} = 0.5$.

As a consequence, it is possible to switch from U to D and the opposite using the dynamic properties of the field-like torque, as soon as $h^{\perp} > 0.5$. Actually, this dynamic scheme is very similar to the case of field-pulse-induced switching [82]. Different means are available to control the switching in this field-pulse scheme. As the period of one rotation on the orbit is known, it is possible to control the current pulse so that it stops when $\mathbf{m}$ has switched to the opposite equilibrium position. Alternatively, by increasing the Gilbert

damping α, it is possible to reach a regime where $\mathbf{m}$ stabilizes at one particular equilibrium by tuning the energy dissipation, in order to get a deterministic switching whatever the length of the pulse [82]. However, these approaches are hindered by the difficulty of controlling α and the material parameters accurately enough, in a repeatable way in order to get a reliable deterministic switching. The limitation of this scheme can be seen in Fig. 4.3a, which shows the trajectory of $\mathbf{m}$ under the sole field-like torque and in the absence of external fields. Because the damping is too low, many precessions occur around $\hat{\sigma}$, so that the position where $\mathbf{m}$ finally stabilizes cannot be predicted.

We now approach the role of the Slonczewski torque in our dynamic switching scheme. Due to its form in $\mathbf{m} \times (\hat{\sigma} \times \mathbf{m})$, the Slonczewski torque is very similar to the torque originating in the damping process [see Eq. (2.10)], which makes the Slonczewski torque to be sometimes called a damping-like torque. As explained in ref. [38], the Slonczewski torque does not necessarily compete with the damping, but can contribute or oppose to the damping torques given the sign of $\cos\left(\widehat{\hat{\sigma}, \mathbf{m}}\right)$, the cosine of the angle between $\hat{\sigma}$ and $\mathbf{m}$.

As we mentioned in the beginning of the chapter, we now consider the case where both Slonczewski and field-like torques are present, and $\alpha = 0.01$ like in most technologically relevant magnetic materials. The proper balance of the two SOT terms addresses the issues we mentioned above for the field-like torque pulse scheme. We consider different cases for which $c^{\parallel}/c^{\perp}$ is lower than unity but non-zero. The field-like torque still dominates the dynamics, so that the nature of the precession orbits remains unchanged in the first approach. Only the position of U and D are slightly moved towards $+\hat{\mathbf{x}}$,

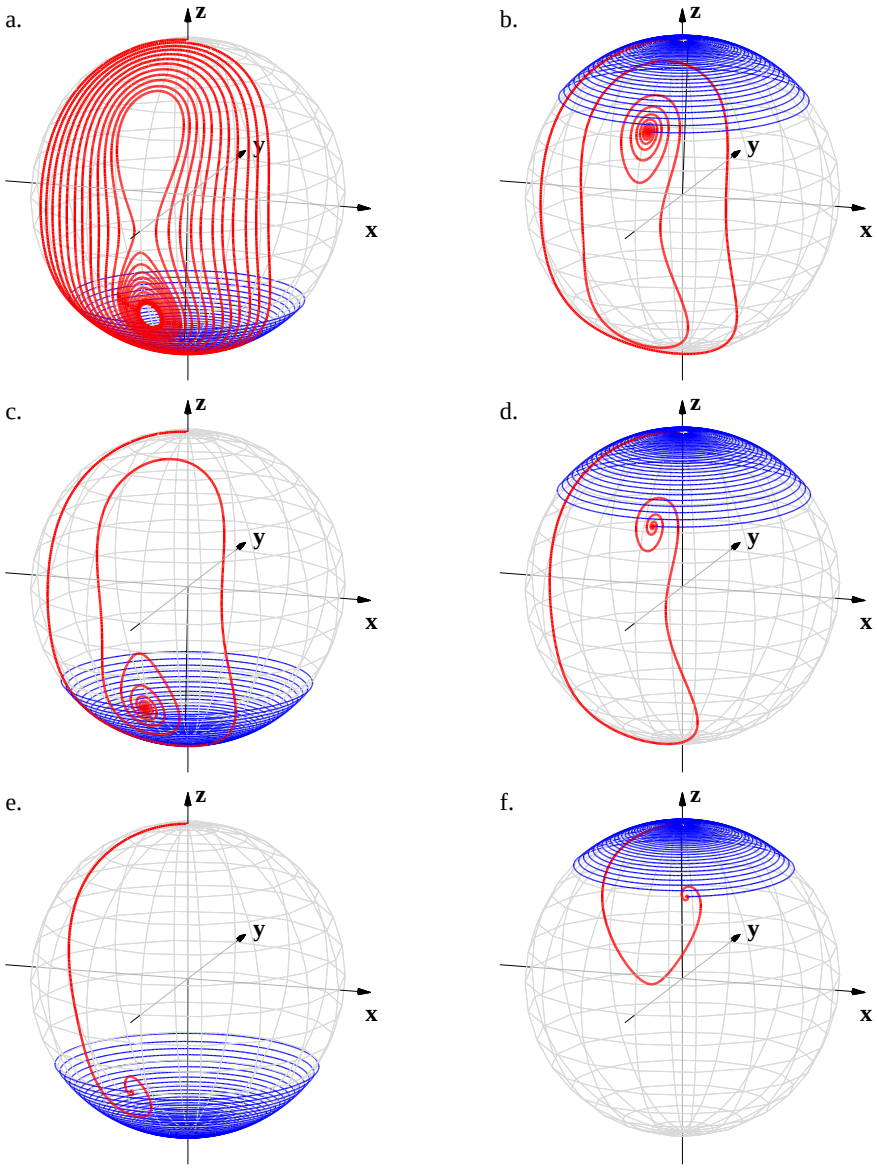

Figure 4.3: Switching trajectories obtained for increasing values of the ratio between the Slonczewski and the field-like torques in the absence of external fields. a. $h^{\parallel} = 0$ and $h^{\perp} = 0.8$. b. $h^{\parallel} = 0.04$ and $h^{\perp} = 0.8$. c. $h^{\parallel} = 0.05$ and $h^{\perp} = 0.8$. d. $h^{\parallel} = 0.1$ and $h^{\perp} = 0.8$. e. $h^{\parallel} = 0.2$ and $h^{\perp} = 0.8$. f. $h^{\parallel} = 0.3$ and $h^{\perp} = 0.6$. In each case, $t'_{rise} = 0$ and the pulse is much longer than 2π: the red curve corresponds to the time evolution of $\mathbf{m}$ during the current pulse, and the blue curve corresponds to its relaxation after the pulse.

which does not affect the general behaviour. As the motion of $\mathbf{m}$ is restrained to the hemisphere for which $y < 0$, the sign of $\cos\left(\widehat{\hat{\sigma}, \mathbf{m}}\right)$ is always positive so that the Slonczewski torque acts as an additional source of damping. By progressively increasing the strength of the Slonczewski torque, the effective damping along the trajectory is also reinforced. As a consequence, the initial

energy supplied by the sharp rising pulse is dissipated faster and **m** precesses for a shorter time before it stabilizes at either U or D. We can define a precession order N which accounts for the rotations of **m** around $\hat{\sigma}$: each time **m** crosses the xy plane, we count one half-turn so that N is an half-integer. Due to the enhanced damping obtained from the Slonczewski torque, it is natural that N decreases with the increasing values of $h^{\parallel}$. This is shown in Figs. 4.3b-f: by increasing $c^{\parallel}/c^{\perp}$ from 0 to 0.05, 0.0625, 0.125, 0.25 and 0.5, N decreases from a very large value in the absence of the Slonczewski torque, to $N = 2$, 3/2, 1, 1/2 and 0. In the particular case of Fig. 4.3e, for which $c^{\parallel}/c^{\perp} = 0.25$, **m** reverses directly from its initial position to the opposite one, without precession because the Slonczewski torque is large enough to prevent **m** from switching back to its initial position. When $c^{\parallel}/c^{\perp}$ is further increased (Fig. 4.3f), the motion of **m** is so damped that it cannot cross the xy plane and switching is not possible. In each case, **m** stabilizes at the unswitched or switched position during the current pulse. The relaxation phase does not affect the switching and **m** relaxes to the side it was stabilized under currents. By changing the damping parameter from $\alpha = 0.001$ to $\alpha = 0.2$, these results are not qualitatively changed. Note however that a high value of α makes the relaxation phase shorter after the current pulse and is thus to be preferred.

The deterministic switching obtained for $h^{\parallel} = 0.2$ and $h^{\perp} = 0.8$ and resulting in $N = 1/2$ (Fig. 4.3e) shows different interesting properties. (i) The switching is deterministic in the absence of assist field: it is the dynamic relation between the torques that results in systematic switching. (ii) The outcome of the switching is not affected by the length of the pulse as soon as it is longer than the time required to stabilize **m** at $z < 0$. Any longer pulse

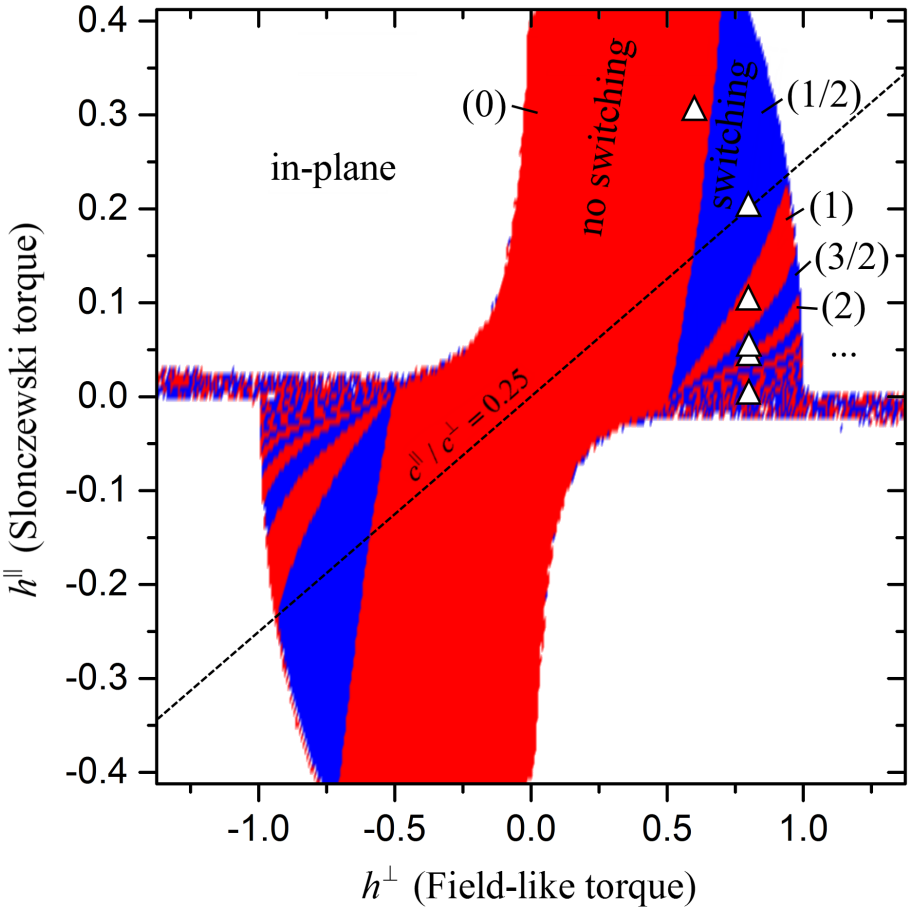

Figure 4.4: Switching outcome as a function of the strength of the field-like and Slonczewski torques, with $t'_{rise} = 0$. The red domains correspond to an unswitched magnetization, the blue domains indicate a switched final state, and the white domains indicate when **m** is driven to the plane under currents, resulting in non-deterministic switching. The dashed line indicates the points where $c^{\parallel}/c^{\perp} = 0.25$. The white triangles are the points corresponding to Figs. 4.3a-f. The numbers into brackets indicate the precession number N within each domain.

works as well so that a precise control of the pulse is not required. (iii) The two states U and D are equivalent in this scheme, and reversing the current does not affect the dynamics as the system is symmetric with respect to the yz plane. As a consequence, both U to D and D to U toggle switching are obtained for the two current polarities, which differs with the quasi-static switching scheme described in §3.3 where the direction of the switching is determined by the sign of $h_x J$.

It is relevant to look at the different switching behaviours for all possible

combinations of the two SOT terms. Figure 4.4 shows the final state after the application of the current pulse to the system, extending the few cases studied in Figs. 4.3a-f. A blue colour indicates that **m** has switched from U/D to the opposite magnetization, while a red colour indicates that the final state is unswitched. For the values of $c^{\parallel}/c^{\perp} < 0.01$, the damping remains too low in the system and the magnetization reversal is not deterministic, resulting in the central part of the figure being composed of mixed blue and red points. When $c^{\parallel}/c^{\perp} > 0.01$, the Slonczewski torque contributes to the damping and reduces N so that the outcome of the switching is deterministic. The lines separating switching and non-switching are therefore obtained numerically as we do not have analytical equations for them.

We distinguish switching via more than one precession ($N = 3/2, 5/2, ...$), unswitched outcome after some precession ($N = 1, 2, ...$), efficient switching via half-precession ($N = 1/2$) and prevented attempts ($N = 0$). When the combined SOT terms are too strong, the U and D position merge in the xy plane. Under currents, **m** will therefore stabilize in-plane, and the subsequent relaxation of **m** from the plane leads to a non-deterministic issue. The corresponding points are drawn in white in Fig. 4.4. They are defined by $h^{\parallel} > 0.5$ and $h^{\perp} > 1$ in the simple case where only one torque is considered, or by lower values when both torque combine. Also, when $c^{\parallel}$ and $c^{\perp}$ have opposite signs, the magnetization easily lies in the xy plane, as can be seen in Fig. 4.4. The behaviour of **m** for the different signs of the field-like torque has been explored in [67].

The most interesting case is definitely $N = 1/2$, as it allows a fast and direct switching. As can be seen from the extent of the blue region (1/2) in Fig. 4.4, switching with $N = 1/2$ is quite robust to any variations of the

ratio of the torques and/or current. It is also very important that for some values of $c^{\parallel}/c^{\perp}$, for example 0.25, no switching back is possible as $N = 0$ or 1/2 whatever the current density is. This feature can be seen from the dashed line in Fig. 4.4. We find that the switching is reliable (N limited to 0 or 1/2), for $c^{\parallel}/c^{\perp} = 0.23$–$0.55$. Such robustness comes from the fact that the damping originates in the current itself: if more current is applied to the system, resulting in a larger initial precession energy, the effective damping is also enhanced. The additional energy is therefore compensated by a larger dissipation and the switching trajectory is almost similar. In this view, this scheme is undeniably superior to the field-pulse scheme, is which the proper current density to be applied is largely dependant on the value of α in the system [82]. The condition $c^{\parallel}/c^{\perp} = 0.23$–$0.55$ can be achieved easily in SOT heterostructures, as the value of $c^{\parallel}/c^{\perp}$ was found in this range for Ta/CoFeB/MgO [39, 52, 66] and Hf/CoFeB/MgO [83], among the material combinations explored so far.

4.3 Influence of the rising time

The condition $c^{\parallel}/c^{\perp} = 0.23$–$0.55$ derived above is found for an ideal pulse without rising time. However, this dynamic switching scheme exploits the initial lag of the magnetization behind the new equilibrium positions displaced by the torques. For a very long rising time, which would correspond to a quasi-static regime, we have seen that a deterministic switching outcome is not expected. We then expect the rising time of the pulse to strongly affect the outcome of the switching: this section is devoted to this effect, as a finite rising time cannot be avoided in real experimental conditions.

We model the same switching event as in Fig. 4.3e, but we now assume

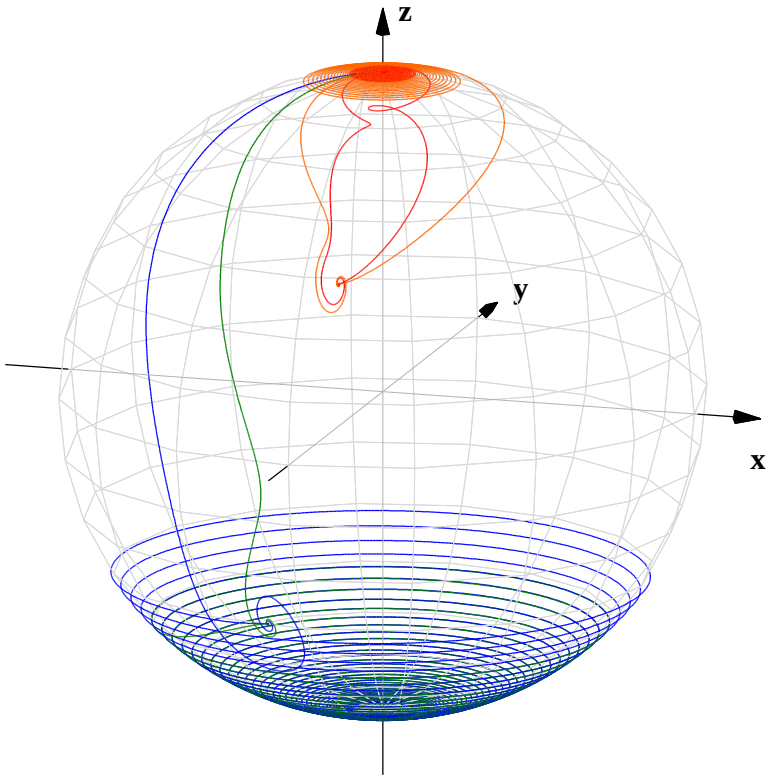

Figure 4.5: Switching trajectories obtained for increasing values of the rising time of the pulse. The different curves correspond to t_{rise} = 50 ps (blue), 200 ps (green), 400 ps (orange) and 800 ps (red). Other parameters are same as in Fig. 4.3e.

different rising times t_{rise} for the pulse. In order to assess the experimental feasibility of our switching scheme, we consider the rising time in picoseconds rather than in the natural time unit t'. The system parameters were defined above. The different switching trajectories for t_{rise} = 50 ps, 200 ps, 400 ps and 800 ps are shown in Fig. 4.5. They correspond to $t'_{rise} = 0.3\pi$, 1.2π, 2.2π and 4.5π, respectively. For t_{rise} = 50 ps, the behaviour is not significantly altered and the trajectory of **m** remains very close to the trajectory for an ideal pulse, because $t'_{rise} \ll 2\pi$. Even for t_{rise} = 200 ps, switching by half-precession is still observed, although the trajectory is modified. However, for the longer rising times **m** behaves similarly as in the quasi-static regime, because $t'_{rise} \approx 2\pi$. As a consequence, **m** shifts significantly towards the dis-

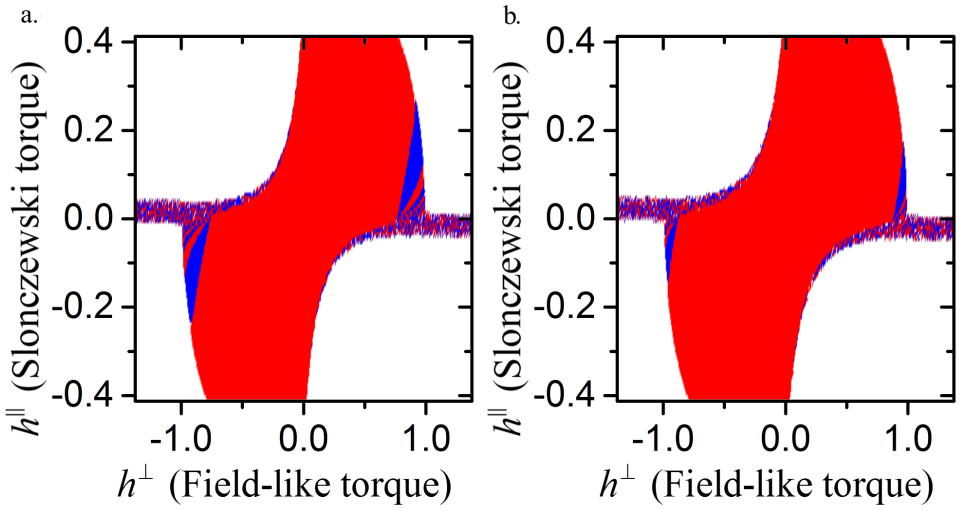

Figure 4.6: Switching outcome as a function of the strength of the field-like and Slonczewski torques for rising times of a. $t_{rise} = 300$ ps and b. $t_{rise} = 1000$ ps. The red domains corresponds to an unswitched magnetization, the blue domains indicates a switched final state, and the white domains indicate when **m** is driven to the plane under currents, resulting in non-deterministic switching.

placed equilibrium position during the rising edge of the current pulse. This affects the initial lag so that the amplitude of the precession is consequently reduced and **m** cannot switch, as it does not even reach the xy plane.

A finite rising time thus modifies the behaviour of the system, because less initial energy is supplied to **m** during the rising edge. In order to compensate, the field-like torque (which shifts the equilibria and supplies some energy to **m**) needs to be increased, while the Slonczewski torque (which dissipates the energy) needs to be reduced. This effect can be seen in Figs. 4.6a,b which show the switching outcome as a function of the amplitude of the SOT terms for rising times of 300 ps and 1000 ps, respectively. For $t_{rise} = 300$ ps ($t'_{rise} = 1.7\pi$), the switched, blue domains (as well as the other domains with $N > 1$) shift outwards (to larger $h^{\perp}$ values) and shrink (corresponding to lower $h^{\parallel}$). For $t_{rise} = 1000$ ps ($t'_{rise} = 5.5\pi$), switching is no longer expected except for very specific parameters and the switching diagram is mostly filled with the red domain $N = 0$. With a good device design and high-quality

electronics, a pulse rise time of 50 ps is achievable [59]. In these conditions, the switching behaviour is not affected and corresponds to Fig. 4.4. We can conclude that our switching scheme can be used to switch the magnetization in experimental conditions.

4.4 Switching times and anisotropy

We now study the switching times achievable within our dynamic scheme, as this is an essential indicator of the performance of magnetization switching. Our definition of the switching time is when $\mathbf{m}$ crosses the xy plane. In the case presented in Fig. 4.3e, where direct switching is achieved via half-precession, $\mathbf{m}$ crosses the xy plane after $t'_{sw} = 0.41$. With the parameters defined above, this corresponds to $t_{sw} = 145$ ps, which is similar to the switching times obtained in the orthogonal spin-torque scheme [58, 59].

In order to reduce the switching time, it is natural to think about increasing the torques. The precession frequency of a magnet is proportional to the applied (effective) field. This can also be seen from Eq. (4.2): a larger $h^{\perp}$ (combined with a larger $h^{\parallel}$ to keep the same torques ratio) would increase the frequency of precession of $\mathbf{m}$ around $\hat{\sigma}$ and, consequently, the switching speed. In principle, the switching speed would then be inversely proportional to the current density J. Unfortunately, this approach cannot work in our scheme. As explained in §4.2, a torque that overcomes the anisotropy drives $\mathbf{m}$ to the plane and suppresses the deterministic switching.

Therefore, increasing the current density only is not a suitable way of reducing the switching times. In the non dimensional Eq. (4.2), one of the scaling factors between t and t' is H_{ani}. H_{ani} also rescales the characteristic current density J_0. As a consequence, by increasing H_{ani} and J by a common

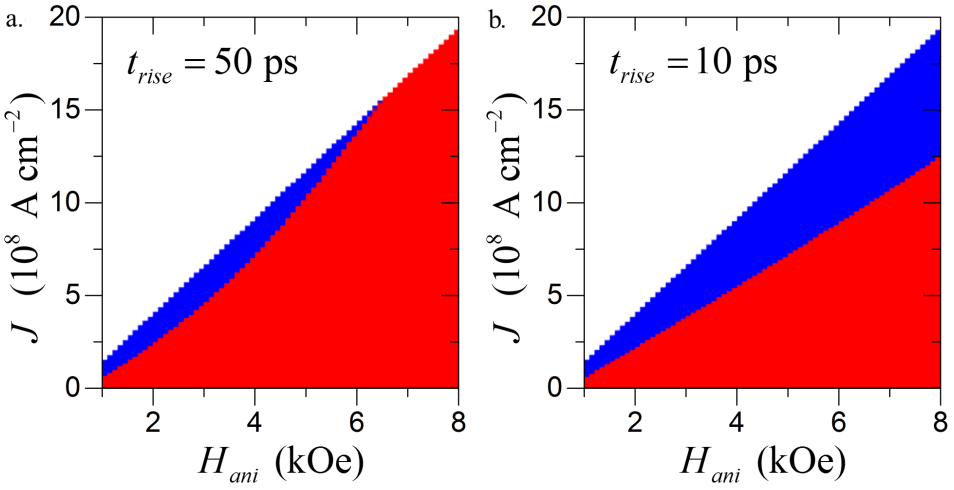

Figure 4.7: Switching outcome as a function of the anisotropy and current density for a. $t_{rise} = 50$ ps and b. $t_{rise} = 10$ ps. The red domains corresponds to an unswitched magnetization, the blue domains indicates a switched final state, and the white domains indicate when **m** is driven to the plane under currents, resulting in non-deterministic switching.

factor, the equation of motion of **m** is self-similar, which means that its non-dimensional form is unchanged[1]. The switching trajectory is therefore identical but covered faster. As long as more current can be applied to the HM, engineering a larger anisotropy of the FM will allow to accelerate the switching, and would also benefit the thermal stability. This principle has nevertheless one requirement: for the trajectory to be identical, the rising time of the pulse should also be reduced by the same factor. However, t_{rise} is an experimental limitation that we cannot avoid: $t_{rise} = 50$ ps cannot be further reduced for applications. By increasing H_{ani}, t'_{rise} is then increasing for the given $t_{rise} = 50$ ps. Once t'_{rise} reaches 2π, the dynamic regime is altered, which prevents switching (as seen in the previous section). We thus need to consider the maximal value of (H_{ani}, J) that will still allow the switching.

To illustrate this point, we simulate the switching for different values of the anisotropy ranging 1000–8000 Oe, comparing two cases: an almost

[1] we remind that $h_x = 0$ in our scheme

ideal $t_{rise} = 10$ ps and a realistic $t_{rise} = 50$ ps. In order to provide typical values for the current densities and anisotropies involved, we define for this part $c^{\perp} = 0.28$ and $c^{\parallel} = 0.07$ (so that $c^{\parallel}/c^{\perp} = 0.25$). Note that the torque coefficients found experimentally range roughly 0.5–3 times these values for Pt, Ta, Hf and W as a HM [22, 37–41, 83]. Thus, these values rather define a lower bound for the switching efficiency of the systems. The results are shown in Figs. 4.7a,b which map the outcome of the switching (the previous colour code is used) for different currents and anisotropies in the cases of $t_{rise} = 10$ ps and $t_{rise} = 50$ ps, respectively. The requirement that J should be increased proportionally to H_{ani} can be seen from the shape of the blue domain. Moreover, the limitation in the increase of J at a given H_{ani} appears as the white area boundary on top of the blue domain.

In addition, looking at the switched blue domain in Fig. 4.7a shows the limitation mentioned above on the maximal value of H_{ani} at a given t_{rise}. When H_{ani} is increased from 1000 Oe to 8000 Oe, t'_{rise} increases from 0.28π to 2.25π. For $H_{ani} > 6500$ Oe, $t'_{rise} \approx 2\pi$, and switching is prevented. As a consequence, the blue domain reduces and finally disappears, being replaced by the red colour corresponding to a failed switching. On the contrary, when t_{rise} is set to 10 ps, t'_{rise} spans 0.06–0.45 for H_{ani} ranging 1000-8000 Oe. Switching is not altered as $t'_{rise} \ll 2\pi$: as can be seen in Fig. 4.7b, the blue domain is preserved even at high anisotropies.

In the range of anisotropies that allow switching, we should then be able to reduce the switching times. In order to keep $h^{\perp} = 0.8$ and $h^{\parallel} = 0.2$, as explained above, we could apply $J = 2.1 \times 10^8$ A cm^{-2} for $H_{ani} = 1000$ Oe and increase both values proportionally. However, we have to consider the effect of the rising time of the pulse. Figure 4.7a shows that the window of

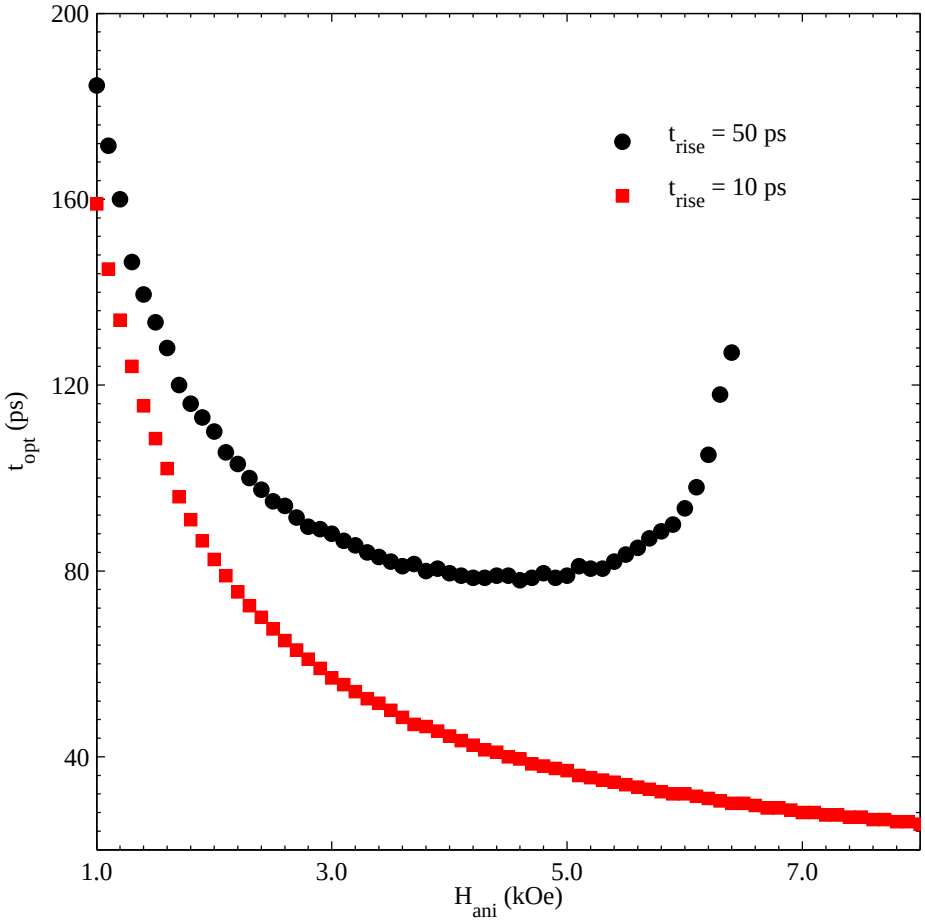

Figure 4.8: Switching times as a function of the anisotropy for $t_{rise} = 50$ ps (black dots) and $t_{rise} = 10$ ps (red squares).

currents allowing proper switching reduces for the higher anisotropies. As it is preferable to ensure the most reliable behaviour, it is suitable to define an optimal current which would fall in the centre of this window, in order to avoid any unexpected outcome of the switching. For each value of the anisotropy, we apply this optimal current density and look at the switching time t_{opt} at this particular current density. The evolution of t_{opt} with the anisotropy is shown in Fig. 4.8 for both $t_{rise} = 50$ ps and $t_{rise} = 10$ ps. As expected, the switching current decreases as $1/H_{ani}$ for the ideal case where $t_{rise} = 10$ ps. For the realistic case of $t_{rise} = 50$ ps, the switching time behaves differently when the anisotropy increases. The switching time decreases as $1/H_{ani}$ for the lowest anisotropies only. However, t_{opt} reaches

a minimal value $t_{opt} \approx 80$ ps at $H_{ani} = 4000$ Oe before it increases with H_{ani}. Once again, this limitation comes from the perturbation due to the finite rising time: when $t'_{rise} \approx 2\pi$, t_{opt} diverges and switching is no longer achievable for $H_{ani} > 6500$ Oe.

Finally, we conclude that given the constraint of the shortest achievable rising time of the pulse, J and H_{ani} can be adjusted together to reach a minimal switching time. It is of much interest that, as long as t_{opt} does not reach its minimum, it evolves as $1/J$ (or $1/H_{ani}$). Increasing the current and the anisotropy concurrently reduces the switching time, but does not increase the total energy required for switching, which is proportional to both time and current. Therefore, the only limitation will come from the maximum current density, as the 7–8$\times 10^8$ A cm^{-2} required for the minimum t_{opt} found in 4.7a—with $c^{\perp} = 0.28$ and $c^{\parallel} = 0.07$—is too high. This limitation can be overcome by the choice of materials with the highest torque efficiencies, as we remind that the values we have chosen here were rather a lower bound.

4.5 Validation by micromagnetic simulations

In the previous sections of this chapter, an essential assumption is that the FM behaves coherently, following the macrospin model. In the present section, we aim at evaluating the validity of this assumption depending on the device size and also on the magnitude of the DMI, which promotes non-uniform magnetization patterns and could thus influence the switching [70]. We perform micromagnetic simulations with the software OOMMF [84] including all the terms introduced in §2.1. The cell size is taken as $2.5 \times 2.5 \times 0.8$ nm^{-3}. We take an exchange stiffness $A_{ex} = 30$ pJ m^{-1} [16]. The DMI constant D differs by some orders of magnitude depending on the material: it

was found that $|D| \approx 0.053$ mJ m^{-2} for Ta/CoFe/MgO heterostructures but $|D| \approx 1.2$ mJ m^{-2} for Pt/CoFe/MgO [85]. For Hf- and W-based heterostructures, different thickness-dependant values of $|D|$ range 0–0.5 mJ m^{-2}. As a consequence, a reasonable value of the DMI in our system would be 0.5 mJ m^{-2}, remembering that it may be larger for Pt, but much lower for Ta.

Simulations of SOT-induced switching are performed for various current densities with two study parameters: the first one is the size of the system ($w \times w = 50 \times 50$ nm^{-2}, 100×100 nm^{-2} and 200×200 nm^{-2}) and the second one is the strength of the DMI ($|D| = 0$ or 0.5 mJ m^{-2}). In order to compare devices with the same effective anisotropy, we compensate the increasing demagnetizing fields in the larger samples by a larger K_2 in order to get $H_{ani} = 1000$ Oe in each square magnet. No assist field is applied. Two parameters are modified in this part: first, α is set to 0.3 during the relaxation phase in order to accelerate the convergence and reduce the computation time and second, the torques ratio is chosen as $c^{\parallel}/c^{\perp} = 0.3$ to avoid switching back from the edges, which have a lower effective anisotropy due to the non-uniformity of the demagnetizing field. The results of the simulations are shown in Figs. 4.9a-f. The green circles indicate the mean value of the out-of-plane component of $\mathbf{m}$ while the red stars indicate its value after the relaxation phase.

Considering no DMI and the magnet size of 50×50 nm^2 that we mentioned earlier, the behaviour simulated by micromagnetic simulations accurately reproduces the coherent switching described by the macrospin model. If we vary the torques ratio, we find the different regimes with $N = 0$, 1/2, 1, etc. As shown in Fig. 4.9a, for $c^{\parallel}/c^{\perp} = 0.3$ we get only one regime of switching without possible switching back, and the switched state has a coherent

magnetization, as can be seen from the inset. After relaxation, the magnetization is effectively switched. For too high current densities, however, deterministic switching is suppressed, as expected from §4.2. Increasing the size of the magnet to 100×100 nm^2 and 200×200 nm^2, a similar behaviour is observed. However, due to the growing non-uniformity of the demagnetization effects in magnets of increasing sizes, their central part is magnetized more and more in the plane, as can be seen from the growing white areas in the insets of Figs. 4.9a-c. Because of $\mathbf{m}$ being in the plane at the end of the pulse, the relaxation phase may be affected by the thermal fluctuations and could lead to non-deterministic switching. As a consequence, a size of 100×100 nm^2 seems to be a maximum size in order to achieve deterministic dynamic switching of the magnetization using our scheme. Considering the DMI now, the size of the system is even more critical. As can be seen from Fig. 4.9d, for a size of 50×50 nm^2 the deterministic, coherent switching regime is restrained to the lower current densities only [inset (i)]. If the current density is too high [inset (ii)], the DMI promotes the formation of a DW, as the effective anisotropy felt by $\mathbf{m}$, getting closer to the plane, reduces[2] and thus cannot oppose the DMI anymore. When the size of the magnet is increased to 100×100 nm^2 or 200×200 nm^2 in the presence of the DMI, the magnetization is reversed through incoherent motion, which leads to a non-uniform final state (Figs. 4.9e,f): the regime of deterministic switching is disrupted.

Finally, the use of micromagnetic simulations confirms that our dynamic switching scheme can be applied to small-sized, monodomain ferromagnets not larger than 100×100 nm^2. However, it is a requirement that the DMI

[2] it is a function of $\cos\theta$, see Eq. (2.15)

keeps a low value in our system ($|D| \ll 0.5$ mJ m^{-2}), as it has a detrimental influence on the deterministic switching.

4.6 Conclusions

By firstly considering the behaviours of both the Slonczewski and field-like torques separately, we have described their different roles in the dynamic regime and how they differ from their quasi-static behaviour. By combining the two torques, deterministic switching outcomes can be obtained, even without applying an external assist field to the system. Notably, for a ratio of the Slonczewski torque to the field-like torque ranging 0.23–0.55, direct switching via half-precession is observed without switching back for a large range of current densities, and even in the absence of external fields. This new switching scheme remains reliable whatever the length of the current pulse applied to the system; however, the rising time of the pulse is a critical factor that limits the switching times and even the possibility of switching in the extreme cases. We have explored a way of reducing the switching time down to 80 ps in realistic conditions by concurrently increasing the anisotropy of the system and the applied current, which does not increase the energy required to switch the magnetization. Finally, we have conducted micromagnetic simulations in order to find the requirements of this switching scheme regarding the device size and the magnitude of the Dzyaloshinskii-Moriya interaction. This method is applicable to technologically important systems of sizes below 100×100 nm^2, at the condition that they do no exhibit a significant Dzyaloshinskii-Moriya interaction. Ta-based systems would then constitute an ideal candidate for the implementation of this method, as Ta has been shown experimentally to generate torques in a wide range of ratios—

adjustable for our purposes to 0.23–0.55 by tuning its thickness [52]—high torque efficiencies, and a negligible Dzyaloshinskii-Moriya interaction ($|D| \approx$ 0.053 mJ m^{-2} [85]). Given the high-paced on-going research on spin-orbit torque heterostructures, there is no doubt that more material combinations compatible with our scheme will emerge. The solution provided here is thus satisfying for fast and reliable spin-orbit torque switching in magnetic materials as it avoids the undesirable requirement of applying an external assist field.

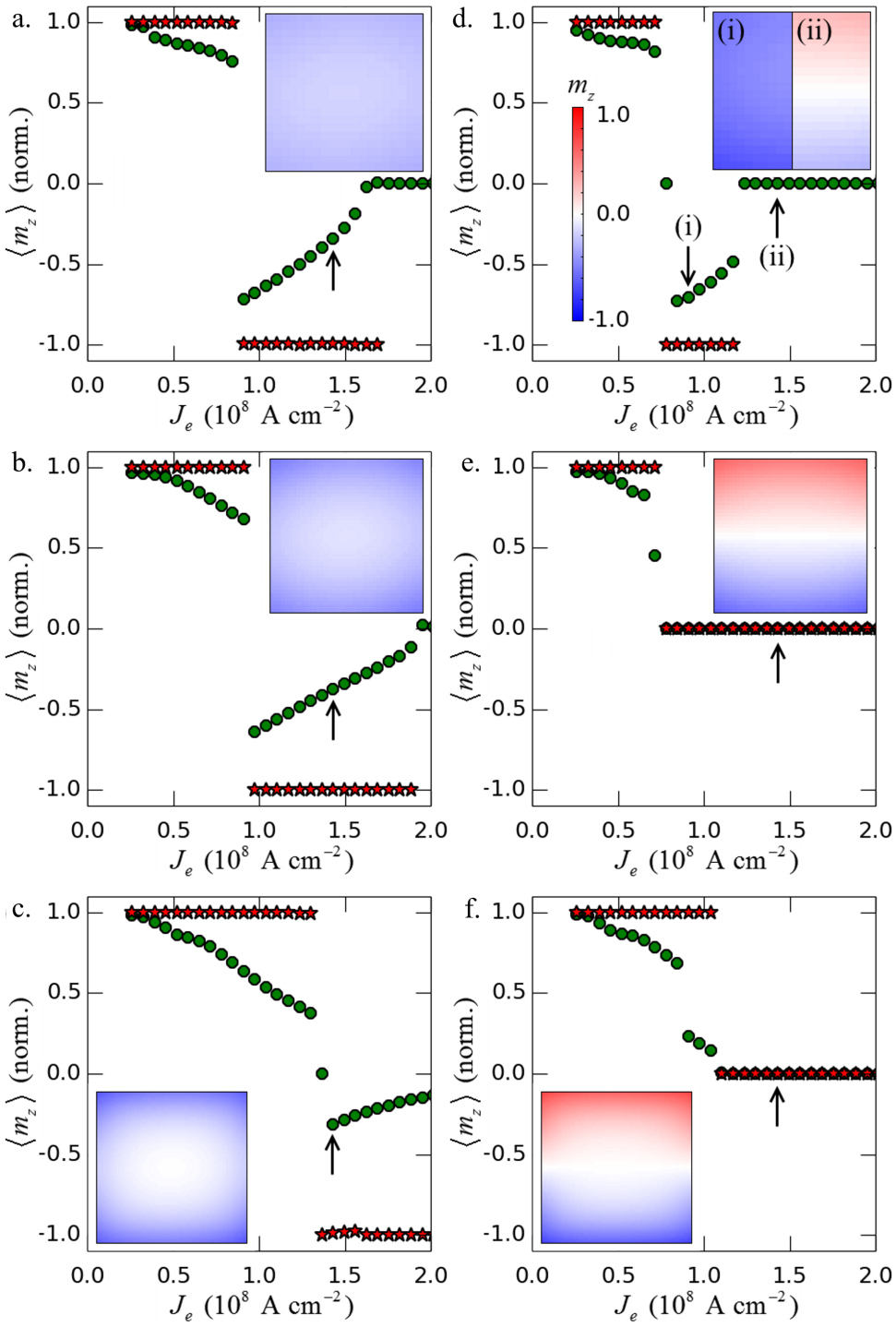

Figure 4.9: Micromagnetic simulations of dynamic SOT switching for different sizes and strengths of the DMI. $|D| = 0$ mJ m^{-2} for a. 50×50 nm^2, b. 100×100 nm^2 and c. 200×200 nm^2. $|D| = 0.5$ mJ m^{-2} for d. 50×50 nm^2, e. 100×100 nm^2 and f. 200×200 nm^2. The green circles (red stars) indicate the mean value of $\mathbf{m} \cdot \hat{\mathbf{z}}$ just before relaxation (after relaxation). The inset in each panel corresponds to a top view of the magnet just before relaxation, showing $\mathbf{m} \cdot \hat{\mathbf{z}}$ as coded on the colour scale in d., for $J = 1.43 \times 10^8$ A cm^{-2} (black arrows). Only for d., the inset is split into two parts (i) and (ii) corresponding to the current densities $J = 0.91 \times 10^8$ A cm^{-2} and $J = 1.43 \times 10^8$ A cm^{-2}, respectively (two black arrows).

Chapter 5

Spin-orbit torques in the thermal regime

In this chapter, we are interested in the behaviour of the magnetization for currents under their critical value for switching. In this regime, the magnetization can be switched due to the thermal activation processes (§5.1), well described by the Fokker-Planck analysis. Using the formalism of the Hamiltonian-Langevin equations, we find the thermal barrier under the influence of both Slonczewski and field-like torques (§5.2). We will then be able to identify the influence of the field-like torque on the regime of thermally activated reversals (§5.3). Finally, we will investigate the dependence of the thermal barrier with respect to the in-plane angle of the assist field, as it provides a means of evaluating the amplitude of the field-like torque (§5.4).

5.1 Thermal processes and Fokker-Planck equation

Even when the current applied to the system is under the critical value required to observe a magnetization reversal (in the sense of a direct or precessional switching, as seen in the previous chapters), the magnet can spontaneously switch because of random thermal fluctuations that can punctually contribute to raise the energy of the magnet above the switching point. In order to model the effects of thermal fluctuations on the system, we can consider that a purely random field acts on the magnetization. This is because

the thermal excitation has correlation times much shorter than the time needed for the magnet to reorientate, therefore it appears as purely random in the equations of motion [86]. The equation of motion is to be modified by the inclusion of a random Langevin field $\mathbf{H_L}$, which will modify the evolution of $\mathbf{m}$ as a stochastic process. It then appears that for the thermally activated switching processes, we cannot define a perfectly known position of $\mathbf{m}$ as it evolves randomly over time. In fact, the instantaneous direction of the magnetization is always subject to the deviations due to thermal fluctuations. Assuming that the magnetic system is small enough, we can keep the previous description of $\mathbf{m}$ based on the two degrees of freedom θ and φ, but now the temperature is no longer neglected. A better description of the system is then to define the probability function $W(t, \theta, \varphi)$ describing $\mathbf{m}$ by the probability of finding it at a position (θ, φ) at a time t. This probability density W should be integrable on the unit sphere, and at any time t its integration over the whole sphere gives a cumulate probability 1. To note, it is also possible to simulate the dynamics perturbated by the random thermal fluctuations by adding the Langevin field to the LLG equation, or equivalently [87], by performing time-quantified Monte-Carlo simulations of many switching events. However, to find the large effective energy barriers, some corresponding to switching times of several days or years, it would be required to run billions of steps for each simulation. For this reason, a description in terms of probability density is preferred, which, moreover, allows to directly find the energy barriers by the treatment presented in §5.2.

The evolution of the system is then given by a sum of drift and diffusion terms. The time evolution of an individual $\mathbf{m}$ at a position (θ, φ) affects the probability function, as this individual $\mathbf{m}$ will move somewhere else following

the dynamic terms of the LLG equation. This creates a probability current density which constitutes the drift term. The drift probability density current is obtained from the continuity equation and contributes to $\partial W/\partial t$ as $-\nabla \cdot \mathbf{J_{drift}}$, given by

$$-\nabla \cdot \left(\frac{d\mathbf{m}}{dt}W\right) = -\left(\frac{1}{\sin\theta}\frac{\partial}{\partial\theta}\sin\theta\frac{d\theta}{dt}W + \frac{1}{\sin\theta}\frac{\partial}{\partial\varphi}\sin\theta\frac{d\varphi}{dt}W\right) \tag{5.1}$$

where $d\theta/dt$, $d\varphi/dt$ are obtained from the LLG equation.

Moreover, because of thermal fluctuations, an initially concentrated probability function will diffuse in space. In terms of Langevin dynamics, the random field $\mathbf{H_L}$ that we introduced above is normally distributed around 0 and defined by the statistical average

$$\langle \mu_0 H_{L,i}(t)\mu_0 H_{L,j}(t')\rangle = \frac{2D}{\gamma^2}\delta_{ij}\delta(t-t') \tag{5.2}$$

which indicates that it is isotropic (i and j are Cartesian coordinates) and not correlated at the time scale of the system. We define the diffusion coefficient, $D = \alpha\gamma k_b T/(M_S V)$[1]. These thermal fluctuations contribute to $\partial W/\partial t$ as $-\nabla \cdot \mathbf{J_{diff}}$, given by

$$\nabla \cdot \left(\frac{D\nabla W}{1+\alpha^2}\right) = \frac{1}{\sin\theta}\frac{\partial}{\partial\theta}\frac{D\sin\theta}{(1+\alpha^2)}\frac{\partial W}{\partial\theta} + \frac{1}{\sin\theta}\frac{\partial}{\partial\varphi}\frac{D(\sin\theta)^{-1}}{(1+\alpha^2)}\frac{\partial W}{\partial\varphi}. \tag{5.3}$$

Finally, both drift and diffusion terms are integrated into the Fokker-Plank equation, a partial differential equation which gives the time evolution of

[1] The standard deviation of $\mu_0\mathbf{H_L}$ during a time ΔT, which allows to solve the LLG equation including the thermal fluctuation field, is then simply given by $\sigma_{\mu_0 H_i} = \sqrt{2D/(\gamma^2\Delta T)}$ for all x, y and z components.

$W(t, \theta, \phi)$ and reads as

$$\frac{\partial W}{\partial t} = -\nabla \cdot \mathbf{J_{drift}} - \nabla \cdot \mathbf{J_{diff}}. \tag{5.4}$$

More details about the derivation of the Fokker-Planck equation can be found, for instance, in Refs. [73, 88] which determine all these terms for the similar case of a system subject to STT. Given the uniaxial symmetry of our system, it is convenient to rewrite the Fokker-Planck equation in canonical coordinates. Following Ref. [89], we introduce the Lagrangian density

$$L = -\frac{M}{\gamma}\dot{\varphi}(\cos\theta - 1) - E \tag{5.5}$$

and the canonical coordinates $q = \varphi$ and $p = \partial L/(\partial \dot{q}) = -(M/\gamma)(\cos\theta - 1)$. The first term in Eq. (5.5), corresponding to $p\dot{q}$, is the Berry phase: refer for instance to Ref. [90] for a more comprehensive introduction of the Lagrangian density. We also define $g = \sin\theta$ and transform Eq. (5.4) into

$$\begin{aligned}\frac{\partial W}{\partial t} = &-\frac{\partial}{\partial q}\left(\frac{dq}{dt}W\right) + \frac{D}{1+\alpha^2}\frac{\partial}{\partial q}\left(g^{-2}\frac{\partial}{\partial q}W\right) \\ &-\frac{\partial}{\partial p}\left(\frac{dp}{dt}W\right) + \frac{D}{1+\alpha^2}\left(\frac{M}{\gamma}\right)^2\frac{\partial}{\partial p}\left(g^2\frac{\partial}{\partial p}W\right).\end{aligned} \tag{5.6}$$

5.2 Thermal barrier under currents

The calculation of the switching barrier under spin-orbit torques has been made in Ref. [70], but without accounting for the field-like torque. In this section, we extend these derivations to include the field-like torque term, as we aim at evaluating its influence on the switching barriers. In Ref. [89], two assumptions are made for the problem which we will follow closely. First

assumption, the thermal energy k_bT is assumed to be low with respect to the barrier energy (WKB approximation, [91]). Following Ref. [89], we then define the Hamiltonian density derived from (5.6) as

$$\begin{aligned}\mathcal{H} = & \frac{dq}{dt}\frac{\partial S}{\partial q} + \alpha g^{-2}\left(\frac{\partial S}{\partial q}\right)^2 \\ & + \frac{dp}{dt}\frac{\partial S}{\partial p} + \alpha g^{2}\left(\frac{M}{\gamma}\right)^2\left(\frac{\partial S}{\partial p}\right)^2\end{aligned} \tag{5.7}$$

where S is an effective action. The corresponding Lagrangian density is given by

$$\mathcal{L} = -\dot{q}\lambda_q - \dot{p}\lambda_p - \mathcal{H} \tag{5.8}$$

where $\lambda_q = -\partial S/\partial q$ and $\lambda_p = -\partial S/\partial p$ are the counting variables conjugated to q and p, respectively.

We now use the LLG equation to find $\dot{\theta} = d\theta/dt$, $\dot{\varphi} = d\varphi/dt$. Using Eq. (2.11) to relate the effective field $\mathbf{H_{eff}}$ to the energy density, we find

$$\begin{aligned}(1+\alpha^2)\dot{\theta} = & \frac{-\gamma}{M_S g}\frac{\partial \varepsilon}{\partial \varphi} - \frac{\alpha\gamma}{M_S}\frac{\partial \varepsilon}{\partial \theta} \\ & + \gamma \underbrace{\mu_0\left[-\left(H^{\perp} - \alpha H^{\parallel}\right)\cos\varphi - \left(H^{\parallel} + \alpha H^{\perp}\right)\cos\theta\sin\varphi\right]}_{B_p} \\ (1+\alpha^2)g\dot{\varphi} = & \frac{\gamma}{M_S}\frac{\partial \varepsilon}{\partial \theta} - \frac{\alpha\gamma}{M_S g}\frac{\partial \varepsilon}{\partial \varphi} \\ & + \gamma \underbrace{\mu_0\left[-\left(H^{\parallel} + \alpha H^{\perp}\right)\cos\varphi + \left(H^{\perp} - \alpha H^{\parallel}\right)\cos\theta\sin\varphi\right]}_{B_q}.\end{aligned} \tag{5.9}$$

Rewriting these two equations in the (q,p) phase space, one gets

$$\begin{aligned}\dot{q} = & \frac{1}{1+\alpha^2}\frac{\partial \varepsilon}{\partial p} - \frac{\alpha\gamma g^{-2}}{(1+\alpha^2)M_S}\frac{\partial \varepsilon}{\partial q} + \frac{\gamma g^{-1}}{1+\alpha^2}B_q \\ \dot{p} = & \frac{-1}{1+\alpha^2}\frac{\partial \varepsilon}{\partial q} - \frac{\alpha M_S g^2}{(1+\alpha^2)\gamma}\frac{\partial \varepsilon}{\partial p} + \frac{M_S g}{1+\alpha^2}B_p.\end{aligned} \tag{5.10}$$

Second assumption, α (≈ 0.01 in FMs) is considered low as well. Only a small

portion of the energy is dissipated during the thermally activation process. Following [89] again, we can rewrite the Lagrangian density as

$$\mathcal{L} = -\frac{d\varepsilon}{dt}\lambda_\varepsilon - \mathcal{H}_\varepsilon, \tag{5.11}$$

which means that the thermal fluctuations on the isoenergetic curves are neglected. The Lagrangian is split into a non-perturbative part

$$\mathcal{L}_0 = -\lambda_q\left(\dot{q} - \frac{1}{1+\alpha^2}\frac{\partial\varepsilon}{\partial p}\right) - \lambda_p\left(\dot{p} + \frac{1}{1+\alpha^2}\frac{\partial\varepsilon}{\partial q}\right) \tag{5.12}$$

and a perturbative part

$$\begin{aligned}\mathcal{L}_1 = &-\frac{\lambda_q\alpha\gamma g^{-2}}{(1+\alpha^2)M_S}\frac{\partial\varepsilon}{\partial q} + \frac{\lambda_q\gamma g^{-1}}{1+\alpha^2}B_q - \frac{\lambda_q^2\alpha g^{-2}}{1+\alpha^2} \\ &-\frac{\lambda_p\alpha M_S g^2}{(1+\alpha^2)\gamma}\frac{\partial\varepsilon}{\partial p} + \frac{\lambda_p M_S g}{1+\alpha^2}B_p - \frac{\lambda_p^2\alpha g^2}{1+\alpha^2}\left(\frac{M_S}{\gamma}\right)^2.\end{aligned} \tag{5.13}$$

As $\mathcal{H}_\varepsilon = -\mathcal{L}_1$, with the canonical transformation $\lambda_q = \frac{\partial\varepsilon}{\partial q}\lambda_\varepsilon$, $\lambda_p = \frac{\partial\varepsilon}{\partial p}\lambda_\varepsilon$, we get the Hamiltonian density

$$\begin{aligned}\mathcal{H}_\varepsilon = &\lambda_\varepsilon\frac{\partial\varepsilon}{\partial q}\left[\frac{\alpha\gamma g^{-2}}{(1+\alpha^2)M_S}\frac{\partial\varepsilon}{\partial q} + \frac{\gamma g^{-1}}{1+\alpha^2}B_q\right] + \lambda_\varepsilon^2\frac{\alpha g^{-2}}{1+\alpha^2}\left(\frac{\partial\varepsilon}{\partial q}\right)^2 \\ &\lambda_\varepsilon\frac{\partial\varepsilon}{\partial p}\left[\frac{\alpha M_S g^2}{(1+\alpha^2)\gamma}\frac{\partial\varepsilon}{\partial p} - \frac{M_S g}{1+\alpha^2}B_p\right] + \lambda_\varepsilon^2\frac{\alpha g^2 M_S^2}{(1+\alpha^2)\gamma^2}\left(\frac{\partial\varepsilon}{\partial p}\right)^2\end{aligned} \tag{5.14}$$

in which the counting variable λ_ε actually describes the switching path in the energy space. The terms in $\lambda_\varepsilon H_{p,q}$, $\lambda_\varepsilon\alpha$ and $\lambda_\varepsilon^2\alpha$ describe the energy contributions from the SOT, from the damping and from the thermal fluctuations, respectively.

As we are in the low temperature limit, in order to obtain the switching barrier one can integrate the Lagrangian density along the optimal switching path [89]. It is obtained here by approximating that it remains along

the solution trajectory of the LLG equation without thermal activation, or, equivalently, by the set of positions (θ, φ) verifying $\mathcal{L}_0 = 0$. Along this trajectory, the optimal path in energy space corresponds to the values of $\lambda^*_\varepsilon(\theta, \varphi)$ that are the non-trivial solutions of $\mathcal{H}_\varepsilon = 0$. Our treatment cannot follow the one made in Ref. [70], as in the presence of the field-like torque, the switching trajectory is not restrained to the xz plane. Moreover, in our case we consider (in prevision of §5.4) a possible rotation of the external assist field $\mathbf{H_{ip}}$ in the xy plane, by an angle β separating x and $\mathbf{H_{ip}}$. Summing the energy contributions coming from both anisotropy and in-plane field, and using the reduced notations as in Chapter 4, we get the system's energy density

$$\varepsilon = -\mu_0 H_{ani} M_S \left(h_{ip} \sin\theta \cos(\varphi - \beta) + \frac{\cos^2\theta}{2} \right), \tag{5.15}$$

and its derivatives in terms of the canonical coordinates

$$\begin{aligned} \frac{\partial \varepsilon}{\partial q} =& \mu_0 H_{ani} M_S (h_{ip} \sin\theta \sin(\varphi - \beta)) \\ \frac{\partial \varepsilon}{\partial p} =& -\frac{\mu_0 H_{ani} \gamma}{g} (h_{ip} \cos\theta \cos(\varphi - \beta) - \cos\theta \sin\theta). \end{aligned} \tag{5.16}$$

The switching trajectory in (θ, φ) coordinates is found by solving

$$\begin{aligned} -h_{ip} \sin(\varphi - \beta) - h^\perp \cos\varphi - h^\parallel \cos\theta \sin\varphi = 0 \\ -h_{ip} \cos(\varphi - \beta) \cos\theta + \cos\theta \sin\theta + h^\perp \cos\theta \sin\varphi - h^\parallel \cos\varphi = 0 \end{aligned} \tag{5.17}$$

and along this trajectory, we know explicitly $\mathcal{H}_\varepsilon$ from Eqs. (5.14) and (5.16) together, allowing to find $\lambda^*_\varepsilon(\theta, \varphi)$. A value of $\lambda^*_\varepsilon > 0$ indicates that the torques dominate over the damping, and that the system evolves naturally (dissipating some energy), while a value of $\lambda^*_\varepsilon < 0$ indicates that the damping is stronger than the torques, and that the system evolves under thermal

activation (acquiring thermal energy from the environment). If $\lambda_\varepsilon^* > 0$ along the switching trajectory, no thermal activation is required, and the system switches directly. However, if $\lambda_\varepsilon^* < 0$ on a part of the trajectory, this part constitutes the barrier. The overall switching barrier energy is then finally obtained by integrating λ_ε^* along the barrier part of the optimal path

$$E_b = V \int_{E_{min}}^{E_{max}} dE \lambda_\varepsilon^*, \tag{5.18}$$

with V the volume of the magnet, and $\Delta = E_b/(k_b T)$ the thermal stability coefficient. Finally, to check the correctness of the code obtained from the above derivations, we compared its results with the results of Ref. [80] in the case without field-like torque, and found identical optimal paths and switching barriers.

5.3 Field-like torque influence on thermal regime

In the present section, we use the results of §5.2 in order to evaluate the influence of the field-like torque on Δ. Under the presence of an assist field $H_x\hat{\mathbf{x}}$, we compare the switching barriers with and without a field-like torque. An assist-field is applied in the x direction and its amplitude is varied over the range $h_{ip} = 0.10$–0.46. At each field value, we look for the thermal barrier dependence on J. We obtain the maps of $\Delta(J, h_{ip})$ for $c^{\parallel} = 0.07$ and three values of $c^{\perp} = 0$, 0.07, 0.28, which are drawn in Figs. 5.1a-c. The maps were found similar for the negative values of the torques ratio. By definition, the barrier reaches 0 at J_c, the critical switching current.

It is noticeable that the presence of the field-like torque not only affects J_c, as expected from [67], but also modifies the current dependence of the

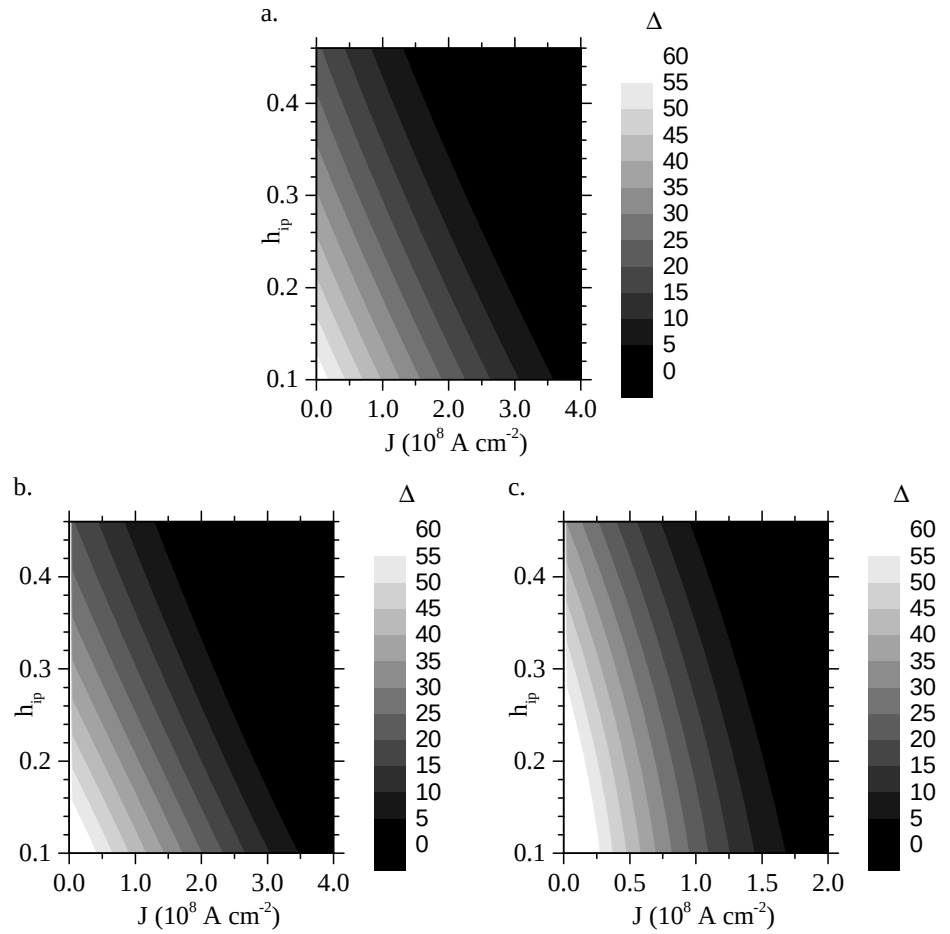

Figure 5.1: Evolution of the barrier height with the amplitude of the assist field for different torques ratios. $c^{\parallel} = 0.07$ and a. $c^{\perp} = 0$. b. $c^{\perp} = 0.07$. c. $c^{\perp} = 0.28$.

thermal barrier at the same time as their height. Particularly in the case of $c^{\parallel} = 0.07$ and $c^{\perp} = 0.28$, the isobarrier lines in Figs. 5.1c are incurved and do not exhibit the similar linear relations compared to other cases. We have to note that some error unavoidably comes from the approximation made in §5.2 that the optimal switching path is restrained along the set of positions (θ, φ) verifying $\mathcal{L}_0 = 0$. Notably, for the low values of the current density J, a more direct path to the switched region may exist. However, for the larger values of the current, the torque dominates and this picture is quite accurate. Thus, we can explain this modification of the relationship between Δ, J and h_{ip} by the fact that the field-like torque dramatically modifies the

switching paths.

A direct application of the relations derived here between the barrier height and the field-like torque is to characterize the SOTs. In order to find whether the field-like torque is present in a system and contributes to the switching or not, the dependence of the assist field to the torque constitutes a criterion. This could then provide an analysis for the results of thermally activated SOT switching [92]. In the view of applications, finding the data retention properties under currents and fields is essential as suggested in [70], in particular for mixed SOT-STT cases [93]. Interestingly, as can be seen by comparing Figs. 5.1a,c, the current dependence is reinforced by the field-like torque in a manner that the thermal barrier is higher at low current, but lower at high current. Such a property may be useful to avoid the cross-talk errors due to the thermally activated switching of half-selected bits.

5.4 Finding the right assist field angle

In this section, the dependence of the thermal activation barrier on the angle of the assist-field is investigated. From §5.3, we have understood that even if the field-like torque can greatly reduce the switching currents, it also has a tendency to curve the originally linear decrease of the barrier with currents and fields. By varying the angle β, the switching can be optimized. Δ is computed as in §5.3, but instead of varying the amplitude of the assist-field, $h_{ip} = 0.2$ is fixed and the in-plane field angle β is varied. The maps of $\Delta(J, \beta)$ for $c^{\parallel} = 0.07$ and three values of $c^{\perp} = 0$, 0.07, 0.28 are shown in Figs. 5.2a-c.

Not only Δ is found to be significantly dependant on β, but also the critical current value J_c. The larger the field-like torque, the more the in-

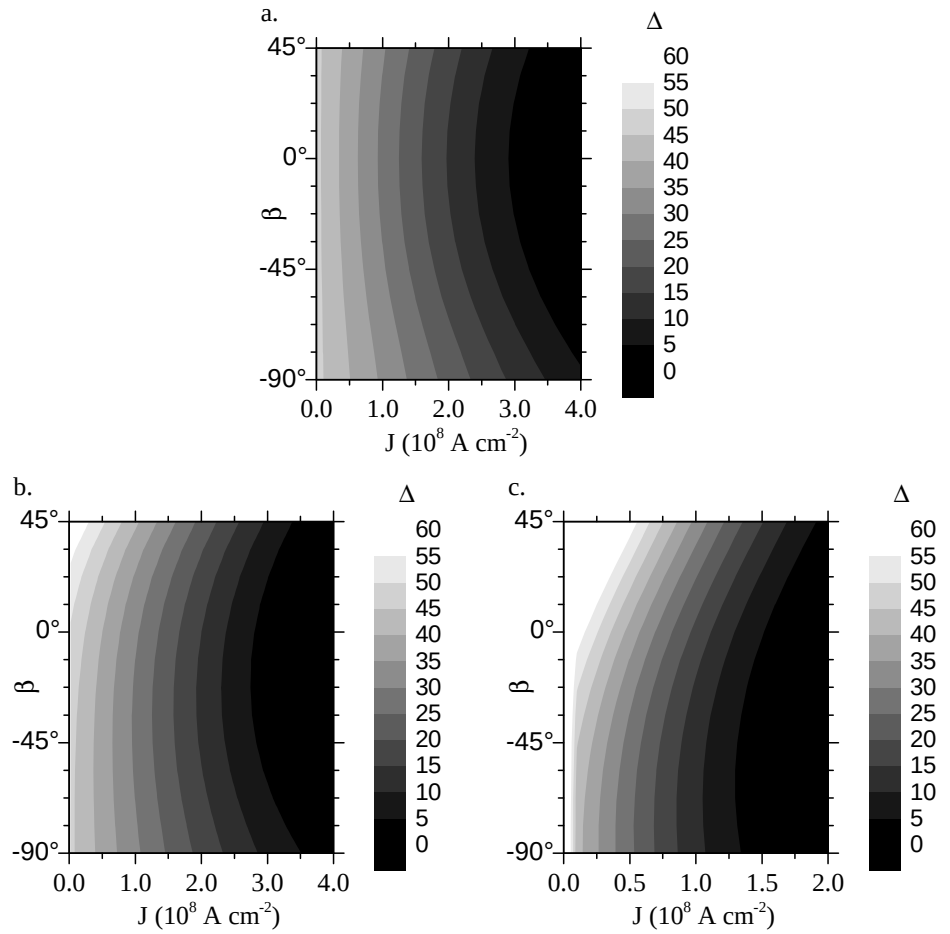

Figure 5.2: Evolution of the barrier height with the angle of the assist field for different torques ratios. $c^{\parallel} = 0.07$ and a. $c^{\perp} = 0$. b. $c^{\perp} = 0.07$. c. $c^{\perp} = 0.28$.

plane assist-field needs to be accordingly rotated. Actually, it is necessary that the direction of the assist field and the direction of the sum of the torques $\mathbf{h}^{\parallel} + \mathbf{h}^{\perp}$ be matched: if they point to different directions, they will compete against each other during the switching process, and increase the energy cost of crossing the barrier.

This point is illustrated in Figs. 5.3a,b: they present a mapping of the energy density ε on the unit sphere, from the lowest energy (dark blue) to highest energy (dark red) on a linear scale, for $\beta = 0$ and $-67.5°$, respectively. $J = 1.5 \times 10^8$ A cm^{-2} and the torques are $c^{\perp} = 0.28$ and $c^{\parallel} = 0.07$. The black line is the trajectory of $\mathbf{m}$ shifted from U without current to U under

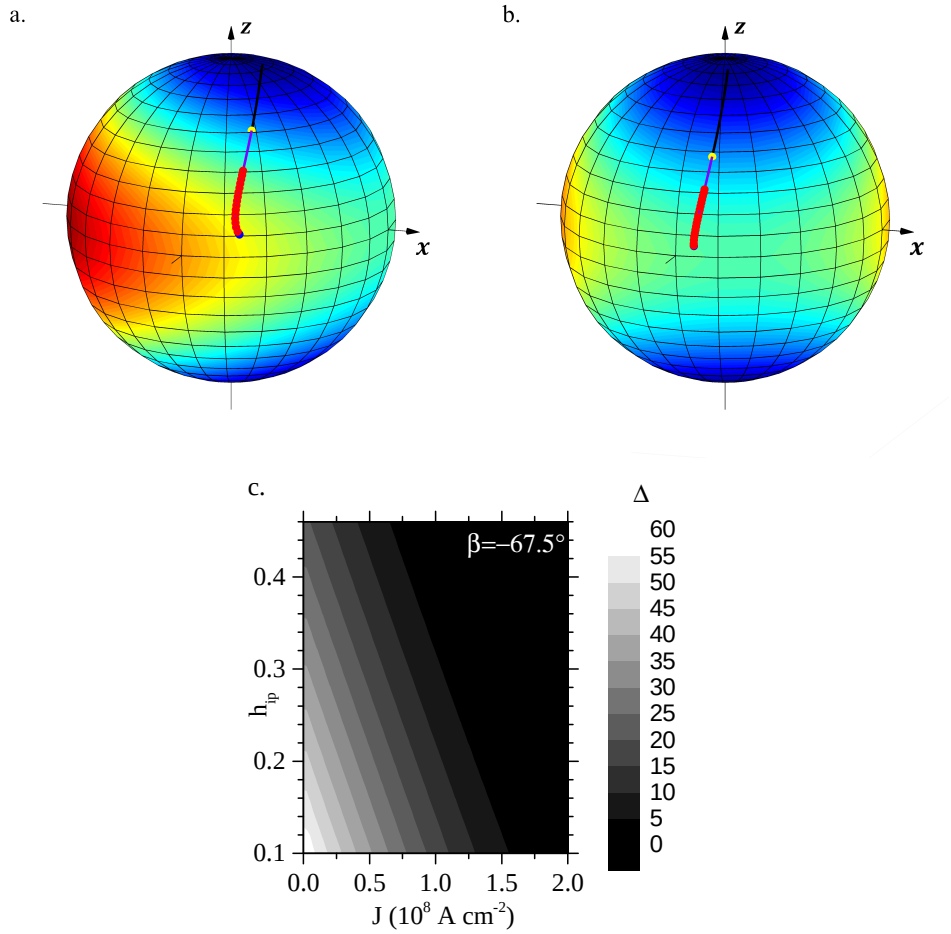

Figure 5.3: Evolution of the barrier height with the magnitude of a rotated in-plane assist field in the case of a significant field-like torque, $c^{\perp} = 0.28$ and $c^{\parallel} = 0.07$. a. Energy density and switching path for $h_{ip} = 0.2$, $\beta = 0°$. b. $h_{ip} = 0.2$, $\beta = -67.5°$. The dark line is the quasi-static trajectory for the current increased from 0 to J and the purple line is the thermally-activated switching path from the displaced U position (yellow point). The outcome of any relaxation along the switching path is color-coded by red(unswitched)/blue(switched) points. c. $\Delta(J, h_{ip})$ for $\beta = -67.5°$.

current (yellow dot) when the current density is slowly increased to J under the critical current. The thermally-activated switching path found from Eq. 5.17 is drawn in purple. Along the thermally-activated switching path, the red/blue dots indicate the final state U or D if $\mathbf{m}$ relaxes from this point under J. As expected, only the extremal point of the thermally-activated switching path, being the top of the energy barrier, allows relaxation to D as denoted by its blue colour.

In the absence of the field-like torque, for an external field aligned with

the current, the switching path belongs to the meridian plane xz [70] and thus has to cross over the lowest energies, being driven close to the saddle point S_1. Under the influence of the field-like torque however, the switching path (in purple in Fig. 5.3a) is driven away from S_1 and is driven to positions of a higher magnetic energy. This causes an increase of the thermal barrier due to field misalignment. Rotating the in-plane field brings the saddle point close to the switching path again and decreases the energy barrier (Fig. 5.3b). As a consequence, the barrier height also recovers its almost linear dependence on the field magnitude, as can be seen from Fig. 5.3c. Under the influence of the field-like torque, aligning the assist field with the direction of the current does not leads to the best switching efficiency. Note that choosing $\beta = -\arctan\left(-c^{\perp}/c^{\parallel}\right)$ roughly allows to get close to the minimum value of Δ and J_c. This angular dependence can also be used to find the components of the SOTs: by varying the angle of the assist-field, it is possible to observe the influence of the field-like torque on the switching and thus to quantify it, by fitting the observed angular dependence to the present model.

5.5 Conclusions

In this chapter, the equations describing the height of the energy barrier for the thermally activated SOT switching were derived in the presence of both Slonczewski and field-like torques, considering in addition the possible rotation of the assist-field. It has been shown that the field-like torque modifies the switching path and thus can decrease the energy barrier as well as the critical current J_c. Moreover, it is obtained by an angular dependence study that aligning the assist-field with the current direction is not necessarily the optimal choice in the presence of a field-like torque. Both the

switching barrier and critical current can be further reduced by rotating the assist-field in the plane. The field magnitude and angle dependence of the $\Delta(J)$ plots can thus be used to study the field-like terms in the SOTs and quantify the torques ratio. This method is not redundant with the vector second-harmonic measurements of the SOTs [39, 52, 53], but rather complementary: with the vector measurements, a local value of the torque is derived at the position of $\mathbf{m}$ imposed by the external field: such measurements can be tedious in the cases where all positions are to be measured to find the angular dependence. With the method proposed in this chapter, a simple evaluation of the average value of $c^{\parallel}$ and $c^{\perp}$ along the switching path is done, which is more relevant for switching phenomena. Indeed, in the previous treatment of the problem of the thermally-activated SOT switching, the possible angular dependence of the SOTs terms—having $c^{\parallel}$ and $c^{\perp}$ varying with θ and φ [39, 94, 95]—has been neglected. For materials that present such an angular dependence, finding an average value is definitely useful but it would be much relevant as well to include the angular dependence explicitly in the derivations presented in this chapter in order to get a refined and more quantitative model, which is left for future works.

Chapter 6

Triaxial anisotropy in spin-orbit torque devices

This last chapter presents a study of the SOT switching in triaxial anisotropy devices. It was found in earlier studies that breaking the symmetry of the layered systems is necessary in order to achieve deterministic switching in the absence of external fields [77, 78]. The approach presented here consists in shaping the magnet in a way that breaks the symmetry (§6.1). By analysing the switching under the simple assumption of a macrospin system, it is found that such a system works in principle (§6.2). The main focus of this chapter however deals with the experimental investigation of this proposed switching scheme (§6.3) which, even if it does not simply fall into the perfect behaviour described in §6.2, shows the features that can be expected from a system of a broken symmetry.

6.1 Principle of triaxial anisotropy in ellipse-shaped devices

In the usual SOT switching scheme, where the magnet possesses a uniaxial magnetic anisotropy, it is customary to apply an external assist field parallel to the current in order to break the symmetry of the system. In Chapter 4, we have defined a way of exploiting the combined dynamics of the two SOT

terms in order to achieve deterministic switching. In this chapter, we also aim at eliminating the assist field to simplify the engineering of the structures, but we would like our method to be compatible with the quasi-static regime, so that simple measurements and comparison with the conventional scheme can be done. Deterministic switching cannot be achieved if the reversal processes are identical for U and D states, and for both current directions [77, 78]. As a consequence, we need to break the symmetry of the system.

To do this, we propose to use the shape anisotropy in a perpendicularly magnetized FM layer, which can be patterned easily as an ellipse. However, the shape anisotropy by itself cannot be the equivalent of the assist field. As can be understood from Eq. 2.5, the shape anisotropy is indeed a quadratic function of the angle with the long direction of an elongated shape, and does not have the form of a field. If one tries to add a shape anisotropy along the current direction to mimic the assist field, this anisotropy—due to its quadratic form—will act as a reversible assist field. Such an anisotropy field helps switching when the current flows in one direction, and reverses when the current flows in the opposite direction, which also helps switching. The sign of $h_x J$ is constant for both U and D states, and for both current directions. In other terms, the symmetry is not broken, as can be seen from Fig. 6.1a.

In order to break the symmetry of the system, we rather have to rotate the long axis of the ellipse in the layer plane. We denote the rotation angle between the long axis of the ellipse, $\hat{\mathbf{u}}$, and $\hat{\mathbf{x}}$ by Φ. We note $\hat{\mathbf{v}}$ the direction of the short axis. As can be seen from Fig. 6.1b, the inversion symmetry is broken by this rotation. The shape anisotropy is no longer uniaxial as

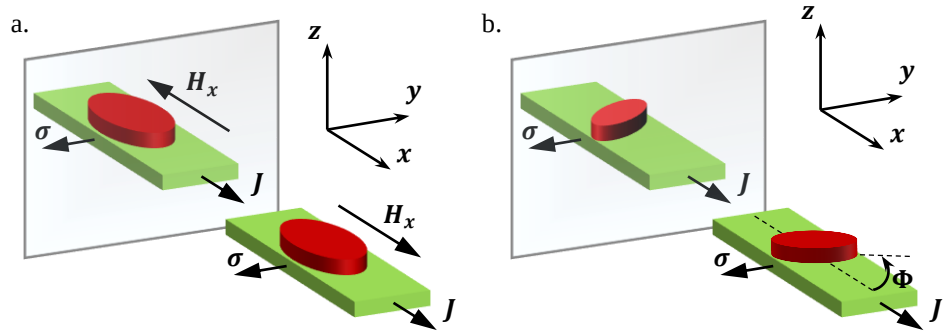

Figure 6.1: a. Schematic of an SOT device with an in-plane shape anisotropy aligned with the current direction. The mirrored image shows an identical device, except if an external field is applied. b. Schematic of an SOT device with an in-plane shape anisotropy rotated with respect to the current direction. The mirrored image shows a different device. In each case the green material is the HM while the red one is the FM.

$N_z > N_v > N_u$ and

$$\varepsilon_d = \frac{\mu_0}{2} M_S^2 \Big[N_u (\mathbf{m} \cdot \hat{\mathbf{u}})^2 + N_v (\mathbf{m} \cdot \hat{\mathbf{v}})^2 + N_z (\mathbf{m} \cdot \hat{\mathbf{z}})^2 \Big] - K_2 (\mathbf{m} \cdot \hat{\mathbf{z}})^2. \quad (6.1)$$

We consider a uniform magnetization inside the magnet, and the interfacial magnetic anisotropy to be larger than all other terms. Using the notations defined in §2.3, we can rewrite the effective field in Eq. (4.2) by finding the derivatives of the energy density

$$\frac{-1}{\mu_0 M_S} \frac{\partial \varepsilon_d}{\partial \theta} = M_S \left[N_z - N_u \cos^2(\varphi - \Phi) - N_v \sin^2(\varphi - \Phi) - \frac{2K_2}{\mu_0 M_S} \right] \sin\theta \cos\theta \quad (6.2)$$

$$\frac{-1}{\mu_0 M_S sin\theta} \frac{\partial \varepsilon_d}{\partial \phi} = M_S (N_u - N_v) \sin\theta \cos(\varphi - \Phi) \sin(\varphi - \Phi) \quad (6.3)$$

which gives us two components of the anisotropy

$$\mathbf{H_a} = \left[\frac{2K_2}{\mu_0 M_S} - (N_z - N_u) M_S + (N_v - N_u) M_S \sin^2(\varphi - \Phi) \right] \cos\theta \hat{\mathbf{z}} \quad (6.4)$$

$$\mathbf{H_b} = -(N_v - N_u) M_S \cos(\varphi - \Phi) \sin(\varphi - \Phi) \sin\theta \hat{\mathbf{z}} \times \hat{\mathbf{m}} \quad (6.5)$$

We finally decompose these terms using $H_{ani} = 2K_2/(\mu_0 M_S) - (N_z - N_u)M_S$ and $H_{sh} = (N_v - N_u)M_S$ to obtain the reduced anisotropies (non dimensional parameters, as in Chapter 4)

$$\mathbf{h_a} = \left(1 + h_{sh}\sin^2(\varphi - \Phi)\right)\cos\theta\hat{\mathbf{z}} \tag{6.6}$$

$$\mathbf{h_b} = -h_{sh}\frac{\sin(2(\varphi - \Phi))\sin\theta}{2}\hat{\mathbf{z}} \times \hat{\mathbf{m}} \tag{6.7}$$

One can verify that we find the same orthogonal components using Eq. (2.4). The shape anisotropy slightly modulates the perpendicular anisotropy depending on the azimuthal angle, but more importantly it generates an additional torque term when $\mathbf{m}$ is close to the plane that makes $\mathbf{m}$ align with $\hat{\mathbf{u}}$.

6.2 Asymmetric destabilization of the equilibria

We now look at the influence of this additional shape anisotropy on the switching regimes. We consider, like in Chapter 4, $M_S = 1500$ emu cm^{-3}, a weak perpendicular magnetization $H_{ani} = 1000$ Oe and a thickness $t_{FM} = 1.6$ nm. By choosing a rather low perpendicular magnetic anisotropy, we aim at amplifying the effects of the shape anisotropy. The size of the elliptical shape defines its demagnetizing factors: we summarize the values of N_u and N_v obtained from the approximation that they have a prismatic shape and the deduced values of h_{sh} according to Ref. [96] in Table 6.1.

Size	400×200 nm^2	200×100 nm^2	100×50 nm^2
N_u	0.00736	0.01295	0.02241
N_v	0.01499	0.02648	0.04592
h_{sh}	0.144	0.255	0.443

Table 6.1: Values of the demagnetizing factors and reduced anisotropy for different ellipse sizes.

Before we perform any numerical simulations, one can expect two effects of the shape anisotropy.

1. The action of the anisotropy should be similar to that of an assist field. As a consequence, different threshold currents should appear for U to D and D to U switching.

2. The equilibrium positions of the magnetization should be shifted. However, Eq. (6.6) and (6.7) suggest that the additional anisotropy have a stronger effect when $\mathbf{m}$ is close to the plane. We expect a large displacement of OM_1 and OM_2, but a smaller shift for U and D. At zero current, U and D will not be displaced from $\pm\hat{\mathbf{z}}$.

To verify these two properties, the switching loops are simulated by applying sweeps of current pulses much longer than the dynamic regime, from $-1.2J_0$ to $1.2J_0$. The size is chosen as 200×200 nm^2 for circles and 200×100 nm^2 for ellipses, with $h_{\parallel} = 0.5$ and $h_{\perp} = 0$. $m_z = \mathbf{m}\cdot\hat{\mathbf{z}}$ is shown in Figs. 6.2a-f for a circular device under no field and $h_x = 0.1$ (Figs. 6.2a,b), and for ellipse shaped devices with $\Phi = 0$, 90, 45 and $-45°$ rotation without field (Figs. 6.2c-f). The initial state can be either U (upwards triangles) or D (downwards triangles). In the case of a circular device, as shown in Fig. 6.2a, all switching thresholds are symmetric and switching cannot be deterministic. The action of the external assist field is to modify the switching thresholds of U and D in order to get deterministic switching (Fig. 6.2b). As expected from our analysis above, shaping a secondary anisotropy which does not break the symmetry is inefficient to provide deterministic switching. The switching thresholds are slightly modified, reduced for $\Phi = 0°$ (Fig. 6.2c), and increased for $\Phi = 90°$ (Fig. 6.2d), but still symmetric. On the

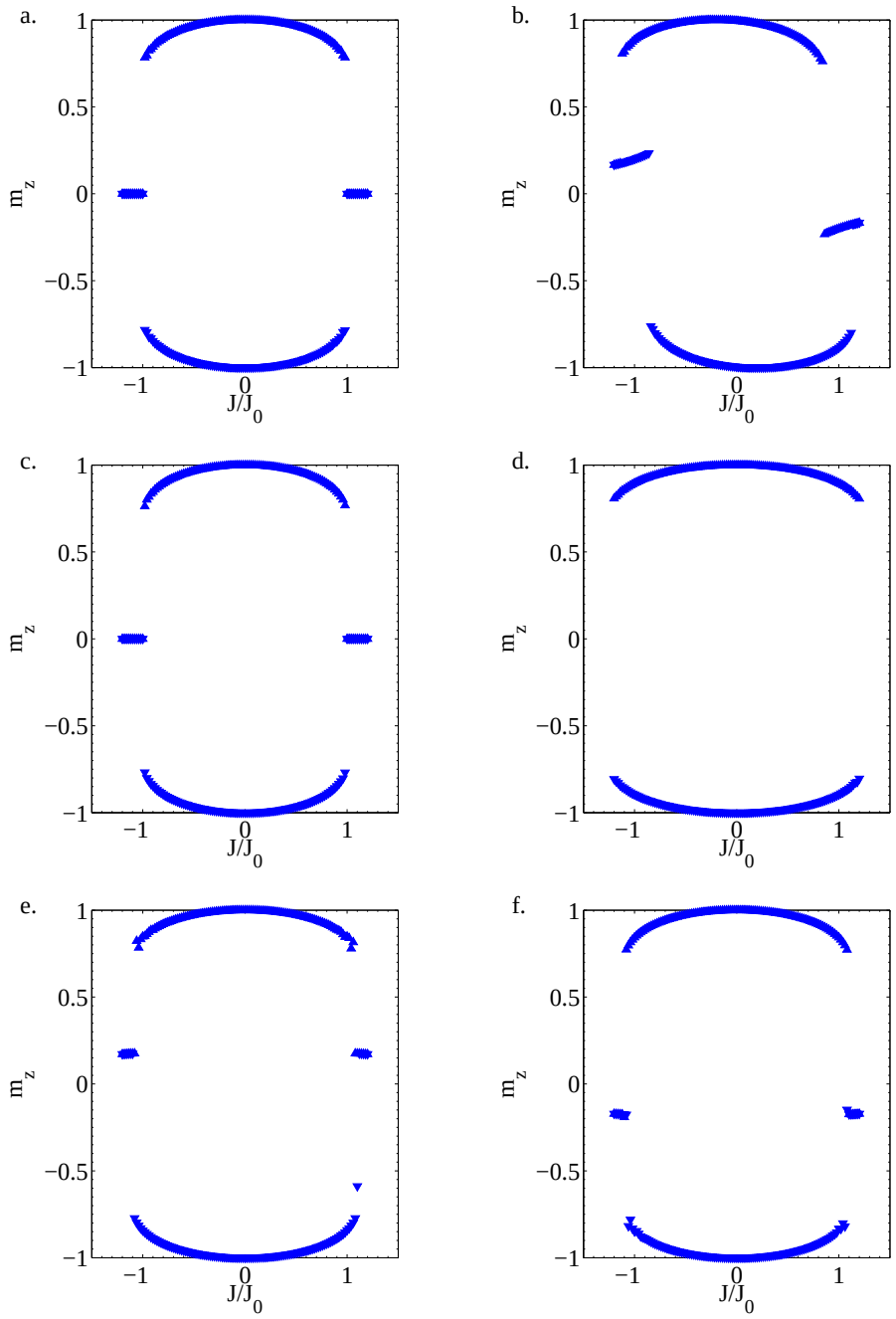

Figure 6.2: Vertical component $m_z = \mathbf{m} \cdot \hat{\mathbf{z}}$ of the magnetization under current in ellipse-shaped devices. a. Circle device, $h_x = 0$. b. Circle device, $h_x = 0.1$. c. Ellipse device, $\Phi = 0°$. d. Ellipse device, $\Phi = 90°$. e. Ellipse device, $\Phi = 45°$. f. Ellipse device, $\Phi = -45°$. The upwards triangles indicate an initial state U, the downwards triangles indicate an initial state D.

contrary, tilting the ellipse modifies the symmetry of the system which gives asymmetric switching thresholds (of a few percent). It is also observed that the position of the OM_1 equilibrium is modified and moves to $z > 0$ for $\Phi = 45°$ (Fig. 6.2e) or to $z < 0$ for $\Phi = -45°$ (Fig. 6.2f). This allows

deterministic relaxation from this state.

6.3 Experimental investigation

To verify the applicability of this principle, we proceed to the experimental verification of the SOT switching properties of ellipse-shaped devices. As we have learned from our study of the DMI in §4.5, its influence opposes the coherent switching behaviour, therefore it is not desirable if we want to observe the properties of a system with uniform magnetization. This reason leads to the choice of Ta for the HM layer, as the DMI is known to be weak in Ta/HM structures [85]. The full multilayer stack is deposited by dc-magnetron sputtering and composed of (Si substrate)/Ta(6)/CoFeB(1)/MgO(2)/SiO_2(3), the numbers into brackets being the thicknesses in nanometres. After deposition, the films exhibit perpendicular magnetic anisotropy. Hall bar crosses with 900 nm-wide arms are patterned by electron beam lithography and ion beam etching. After this, a second electron beam lithography process is used in order to define the pattern of the FM, followed by another etching step down to the Ta layer. We define three types of devices: the usual circular dots corresponding to uniaxial anisotropy systems (300 nm diameter), ellipse-shaped dots with the long axis aligned with the current (300 nm $\times$150 nm), and ellipse-shaped dots whose long axis has been rotated by 45° (also 300 nm $\times$150 nm). A top view of the different devices geometry, with the definition of the measurement currents J_x and J_y, is shown in Fig. 6.3.

We first verify the magnetic properties of the devices by measuring their anomalous Hall resistance (AHR) while sweeping an external magnetic field H_{ext}. The AHR adds a shift to the value of the Hall resistance that is

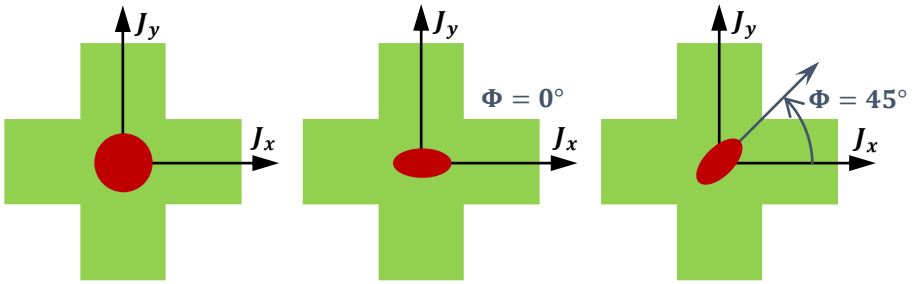

Figure 6.3: Schematic (top view) of the geometry of the devices and definition of the measurement currents.

proportional to the vertical component of the magnetization, allowing us to distinguish between the U and D states. We report one example of AHR loop measurements in both out-of-plane and in-plane configurations. Measurement of the AHR is made in the Hall cross using a sinusoidal waveform current generator and synchronous lock-in detection, keeping a small current value in order to avoid any effect of the torques. As shown in Fig. 6.4a, the devices exhibit a good perpendicular magnetic anisotropy, as only the U and D states appear on the AHE loop. The AHR measured while applying an in-plane field (with a small tilt angle of 2° to avoid the formation of inhomogeneous domains, Fig. 6.4b) gives a good estimate of the effective anisotropy: by fitting the AHR to $\sin\theta = H_{ext}/H_{ani}$, we find $H_{ani} = 750$ Oe. After doing this, the magnetic field is precisely aligned in the plane, and parallel to the current in the x direction, by finding the centred AHR loop at $\pm 0.1°$.

The field being precisely aligned, it is possible to measure the SOT switching under an assist field. The measurement is similar to the previous one, but it is the applied current J_x that is swept instead of the field, which is fixed. In order to avoid accumulated Joule heating, the Hall resistance is measured for single pulses (200 µs) of varying amplitudes. The switching loops for circular devices are shown in Figs. 6.5a-d. As expected, an hysteresis switching

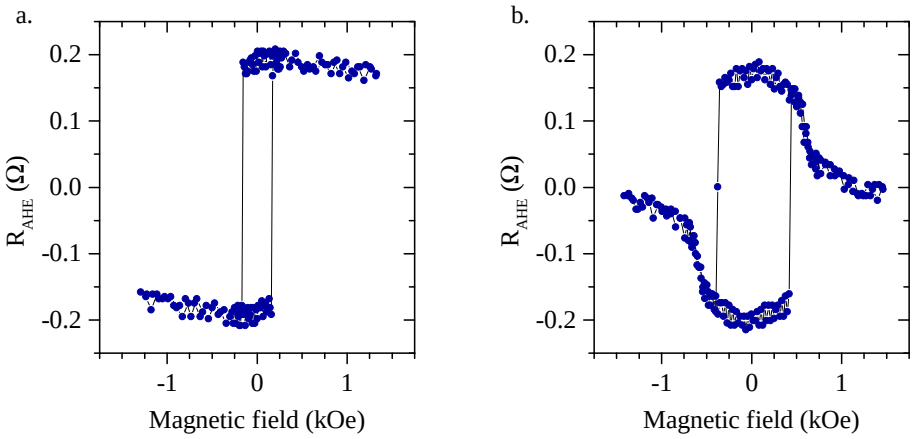

Figure 6.4: a. Out-of-plane and b. In-plane field swept anomalous Hall resistance measurements.

loop is obtained which shows deterministic switching. Moreover, the direction of the switching loop is changed from anticlockwise to clockwise when the field is reversed (Figs. 6.5a-b), which is an evidence of SOT switching. When the assist field is reduced, the switching current increases, which is also expected, and the deterministic switching is less obvious, as can be seen from Figs. 6.5c-d in which R_{AHE} gets closer to zero at high currents.

The same measurements are performed for the rotated ellipse samples and their SOT switching loops are reported in Figs. 6.6a-d. One can notice the successful patterning of the ellipse shape, as the loops exhibit a reduction by a factor of two in the AHR, which reflects the reduction by a factor of two in the device area. No significant differences between the behaviour of the ellipse-shaped and circular devices are present however. This failure to observe any asymmetry in the switching currents may be due to the fact that the assist field dominates the behaviour of the devices or to a reversal mechanism differing from a coherent reversal: in the case of a domain nucleation followed by propagation, the effect of the anisotropy would be extremely reduced.

In order to clarify this point, the SOT-switching loops in the absence of

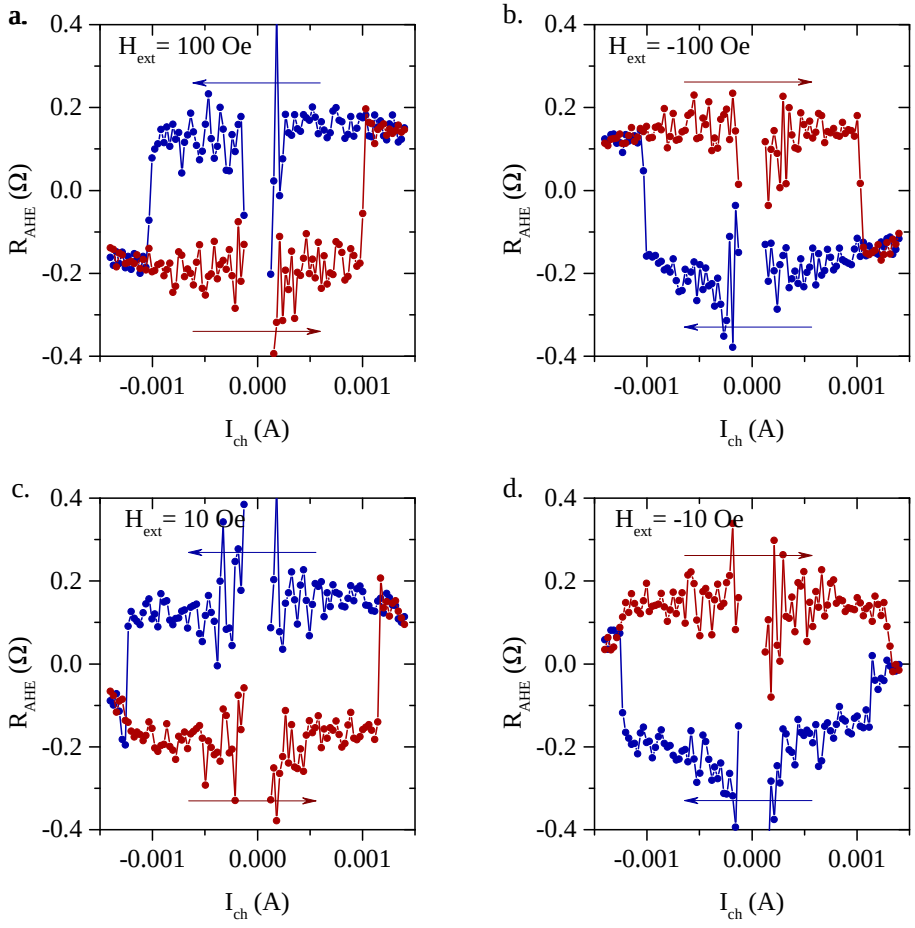

Figure 6.5: Spin-orbit torque current-induced switching loops of circle devices in the presence of different assist fields. a. 100 Oe. b. −100 Oe. c. 10 Oe. d. −10 Oe. The blue points are obtained for a decreasing sweep and the red ones are obtained for an increasing sweep of the current.

external fields are measured. To exclude the possibility of a remanent field in the setup acting as an assist field, the device is rotated from 0 to 180° by 30° steps, and measured at each position. In the case where the switching loop would be determined by an external field, a rotation of 180° of the sample should reverse the loop, which is not observed here as all loops are found similar. The measurements are performed for two different configurations with J flowing along x and J flowing along y (see Fig. 6.3). This allows to measure circular samples (Figs. 6.7a,b) and ellipse samples with $\Phi = 0°$ (Fig. 6.7c), 90° (Fig. 6.7d), 45° (Fig. 6.7e) and −45° (Fig. 6.7f). Also, as non-deterministic outcomes can be expected, the current is swept from zero

to the large positive values, back to the large negative values, and in several cycles in order to complete the loop.

The first noticeable point is that the circular devices and the rotated ellipses show switching hysteresis loops, while the ellipses without rotation do not. For $\Phi = 0°$ the behaviour is non-deterministic with half probability of **m** being up and half probability of being **m** being down at low currents (Fig. 6.7c). For $\Phi = 90°$, only one state is observed. As a perturbation coming from an external assist field is excluded, these effects originate from the devices themselves, even in the circular devices whose symmetry is presumably

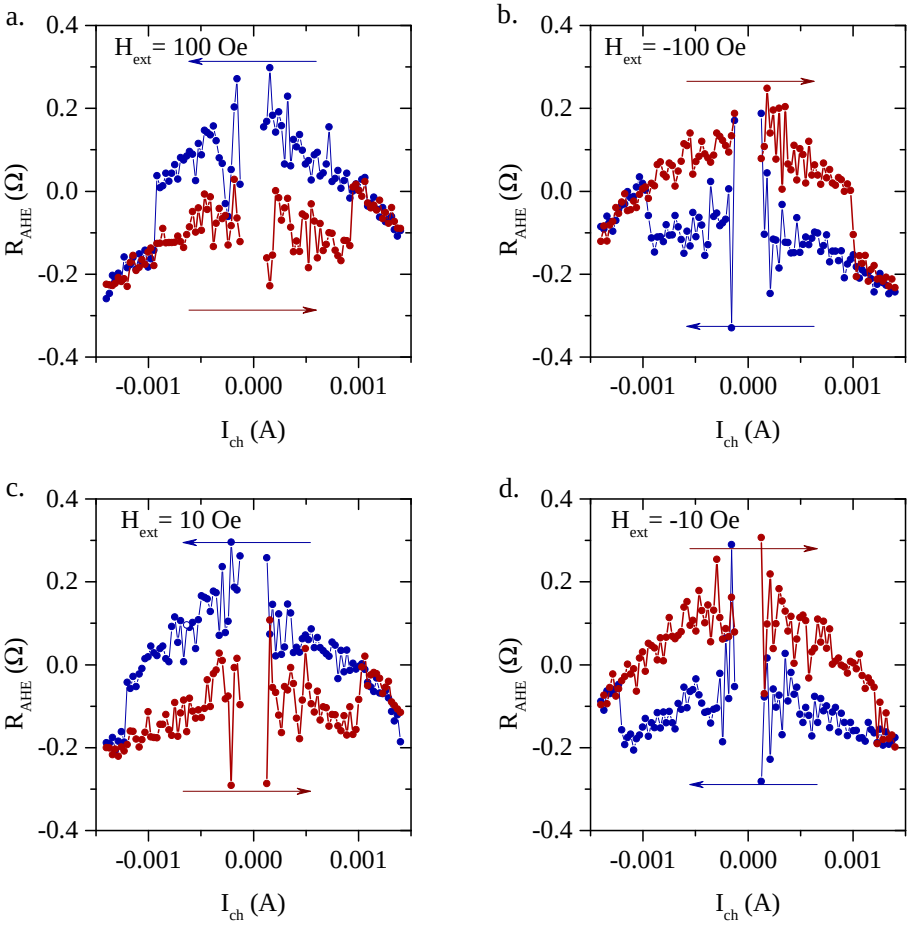

Figure 6.6: Spin-orbit torque current-induced switching loops of ellipse devices (45° rotation) in the presence of different assist fields. a. 100 Oe. b. −100 Oe. c. 10 Oe. d. −10 Oe. The blue points are obtained for a decreasing sweep and the red ones are obtained for an increasing sweep of the current.

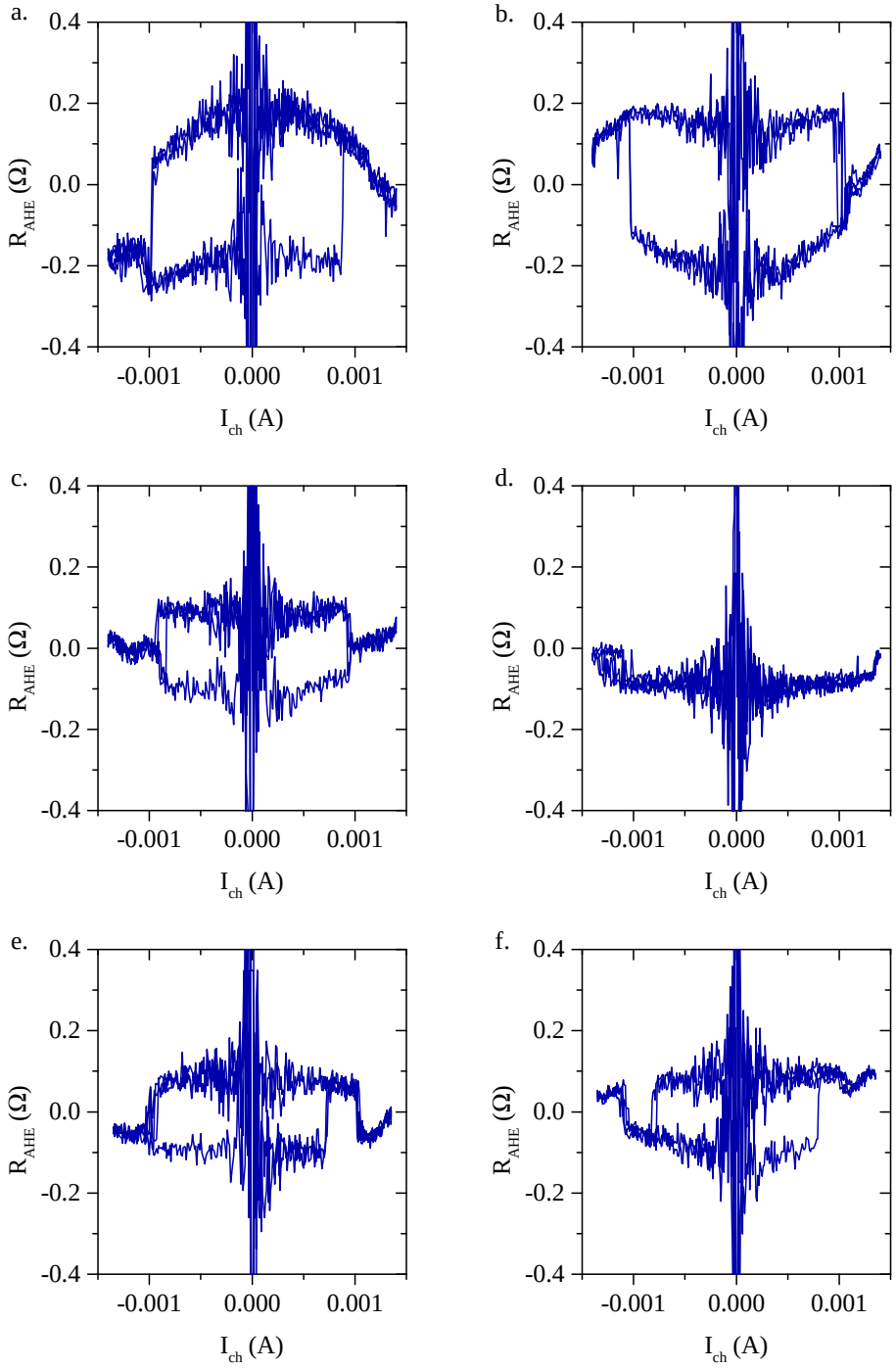

Figure 6.7: Spin-orbit torque current-induced switching loops at zero field. a. Circle, J along x. b. Circle, J along y. c. Ellipse, J along x (0° rotation). d. Ellipse, J along y (90° rotation). e. Rotated ellipse, J along x (45° rotation). f. Rotated ellipse, J along y (−45° rotation).

unbroken. One can imagine that any imperfection of the system originating from the fabrication process, such as non-uniform anisotropy, uneven M_S, current inhomogeneities, misalignment of the dot position, etc. would

favour one switching direction. Unfortunately, these effects cannot be easily controlled: measurements on different circular devices show an opposite direction of the switching loops. In addition, the loop is sometimes reversed when the current direction is changed from x to y in the same device, and sometimes not, supporting that the origin of the switching direction is related to defects.

For the non-rotated ellipses, the measurements are not fully consistent with the macrospin analysis of §6.2. The switching thresholds for a 0° rotation are indeed reduced, and can explain the non-deterministic switching with centred $m_z = 0$. On the contrary, assuming a macrospin behaviour the switching thresholds for a 90° rotation are supposed to be increased. They are found larger for the state presented here, as shown in Fig. 6.7d. However, other loops measured for a manually prepared opposite initial state (not shown) reveal that the switching threshold is reduced for the other state. Such behaviours cannot be explained by the macrospin analysis and may originate from non-uniform switching processes, which we will not analyse here. In the case of the rotated ellipses, unpredictable switching loops similar to the ones found in the circular samples are observed. The few percent of switching currents asymmetry are not sufficient to ensure deterministic switching. However, in addition to them, a second switching occurs at larger current densities (for example, at $I_{ch} = 1$ mA in Fig. 6.7e). In the case of a 45° rotation of the ellipse (Fig. 6.7e), one state (low R_{AHE}) is favoured for both current polarities, and in the case of a $-45°$ rotation (Fig. 6.7f), it is the opposite state (high R_{AHE}), as was analysed in §6.2. As a consequence, this switching characteristic allows deterministic switching of the ellipse from U to D in one case and from D to U in the other case.

6.4 Conclusions and remaining works

The analysis of the critical switching currents and equilibria in triaxial anisotropy devices with a rotated main axis shows that deterministic switching can be achieved even in the absence of external magnetic fields. It is verified by experiments, even if the system does not behave as a perfect macrospin system, that it is possible to exploit the anisotropy of the system to switch its magnetization deterministically at high currents.

However, an issue arises from this geometry, as the switching is found not to be bipolar anymore. In usual uniaxial systems under an assist field, reversing the current allows to achieve the opposite switching event. On the contrary, in the case of a triaxial anisotropy in a rotated ellipse, either in the case of $\Phi = 45°$ or $\Phi = -45°$, only one switching D to U or U to D is obtained whatever the current polarity is, where the opposite switching direction is prevented. Because Φ is fixed while fabricating the device, it is a priori not possible to use these ellipse-shaped devices for memory applications, which require bipolar switching. To circumvent this issue, an alternative device geometry can be employed, where the current can be injected into the HM along two orthogonal directions. Fig. 6.3 actually displays a schematic of such a 4-terminal device.

However, some of the results presented above cannot be explained by the sole macrospin model. Taking the influence of the field-like torque and of non-homogeneous switching into account could be an interesting way of further analysing these experiments. The fact that deterministic switching loops are observed in circular, symmetric devices also deserves more investigation. A careful preparation of the defects, in particular of the structural

asymmetry originating from the misalignment of the dot position, could allow reproducible behaviours, which would be of great significance. One way to predict the conditions for such a deterministic switching would be to perform micromagnetic simulations, accounting for asymmetry, defects in the anisotropy and/or in the current distribution inside the bilayer, as well as their interaction with the field-like torque and the DMI. However, to be able to compare the experiments with a realistic micromagnetic model, a precise characterization of the samples with nanometer-resolved instruments would first be required, in order to understand the nature and size of the defects, the real amount of current imbalance, etc. Such an exploration would constitute a valuable extension of this work.

Conclusions and recommendations

In this thesis, we have been focusing on the switching dynamics of spin-orbit torque magnetic devices. It is expected that spin-orbit torque can provide fast, energy-efficient and reliable switching operations, placing spin-orbit torque devices as a good candidate for the design of future random access memories. In Chapter 3, we have identified two directions of further investigation for the manipulation of the magnetization in FM by spin-orbit torques that would benefit such applications.

The first direction was to find how to avoid the requirement that an external assist field needs to be applied to spin-orbit torque devices. Avoiding this requirement would indeed greatly simplify the engineering and the fabrication of the multilayer stack of spin-orbit torque devices. Two methods have been presented here that can be applied in two different contexts. In the case of quasi-static switching, where the switching speed is not one of the primary objectives, the approach of breaking the symmetry of the system by fabricating a rotated, ellipse-shaped device has been investigated in Chapter 6. It has been shown experimentally that this technique allows deterministic switching of the FM, in a simple bilayered HM/FM system fabricated by a common lithography technique. From this principle, a four-terminal device can be realized which allows to choose the direction of switching by varying the direction of the current. Nonetheless, further investigation of the behaviours observed experimentally is still to be done, in order to understand

and possibly control the deterministic switching originating from defects or inhomogeneities and exploit it in devices. In the situation of dynamic operation, which on the contrary especially aims at triggering the fastest magnetic switching, it has been demonstrated in Chapter 4 that the careful choice of the Slonczewski to field-like torque ratio allows to employ an efficient and simple deterministic switching scheme that does not require the assistance of a magnetic field. This dynamic switching scheme is particularly promising, as the careful study of the switching times and operation requirements has revealed switching performances able to compete with the other spin torque switching schemes. The half-precession switching of the FM is expected to operate in a sub-nanosecond timescale similar to that of the switching in orthogonal spin-torque devices or in the best spin-orbit torque devices achieved so far. Furthermore, the short switching times demonstrated in ultrafast spin-orbit torque devices have been analysed by micromagnetic simulations showing a non-uniform switching process triggered by the assist-field. Our proposed switching scheme promises the same switching speeds in the absence of external fields, as was confirmed by micromagnetic simulations. The development of new materials for spin-orbit torques may combine with this method to allow even shorter switching times at lower current densities. The influence of the angular dependence of the spin-orbit torques in this context remains largely unexplored and could also be combined with the approach presented in this thesis to develop more efficient switching schemes.

The second direction was to identify and understand the role of the field-like torque in magnetization switching. The half-precession switching scheme exposed in Chapter 4, which strongly relies on the field-like torque, constitutes an improvement in the understanding of the combined influences of

both torques in the dynamic regime. We have seen that while the field-like torque brings an excitation to the system, the Slonczewski torque damps the precession the field-like torque has induced. This thesis also helped to complete the understanding of thermally-activated spin-orbit torque switching, by analysing the influence of the field-like torque on the thermal regime in Chapter 5. We have shown that the dependence of the thermal barrier on both the amplitude and the angle of the external assist field is dramatically modified by the presence of a field-like torque, which allows for its characterization. Also, this shows that in the thermal regime, the influence of the field-like torque on the switching currents could be directly observed and distinguished from the one of the Slonczewski torque. This observation provides us a measurement method of the effective torque strengths in the particular context of magnetization switching, that adds to other methods relying on second-harmonic measurements.

Hopefully, these developments will benefit to the understanding of magnetization switching by spin-orbit torque as well as to its application in magnetic memory devices. The outcomes of the present work strengthens the expectations that spin-orbit torques memories can compete with the other magnetic memory technologies and motivates further efforts and developments in the area of 'spinorbitronics'.

Bibliography

1. Baibich, M. N. *et al.* Giant Magnetoresistance of (001)Fe/(001)Cr Magnetic Superlattices. *Phys. Rev. Lett.* **61,** 2472–2475 (1988).
2. Binasch, G., Grünberg, P., Saurenbach, F. & Zinn, W. Enhanced magnetoresistance in layered magnetic structures with antiferromagnetic interlayer exchange. *Phys. Rev. B* **39,** 4828–4830 (1989).
3. Camley, R. E. & Barnaś, J. Theory of giant magnetoresistance effects in magnetic layered structures with antiferromagnetic coupling. *Phys. Rev. Lett.* **63,** 664–667 (1989).
4. Valet, T. & Fert, A. Theory of the perpendicular magnetoresistance in magnetic multilayers. *Phys. Rev. B* **48,** 7099–7113 (1993).
5. Julliere, M. Tunneling between ferromagnetic films. *Phys. Lett. A* **54,** 225–226 (1975).
6. Miyazaki, T. & Tezuka, N. Giant magnetic tunneling effect in Fe/Al2O3/Fe junction. *J. Magn. Magn. Mat.* **139,** L231–L234 (1995).
7. Moodera, J. S., Kinder, L. R., Wong, T. M. & Meservey, R. Large Magnetoresistance at Room Temperature in Ferromagnetic Thin Film Tunnel Junctions. *Phys. Rev. Lett.* **74,** 3273–3276 (1995).
8. Ikeda, S. *et al.* Tunnel magnetoresistance of 604% at 300K by suppression of Ta diffusion in CoFeB/MgO/CoFeB pseudo-spin-valves annealed at high temperature. *Appl. Phys. Lett.* **93,** 082508 (2008).
9. Slonczewski, J. Current-driven excitation of magnetic multilayers. *J. Magn. Magn. Mat.* **159,** L1–L7 (1996).
10. Myers, E. B., Ralph, D. C., Katine, J. A., Louie, R. N. & Buhrman, R. A. Current-Induced Switching of Domains in Magnetic Multilayer Devices. *Science* **285,** 867–870 (1999).
11. Zhang, S., Levy, P. M. & Fert, A. Mechanisms of Spin-Polarized Current-Driven Magnetization Switching. *Phys. Rev. Lett.* **88,** 236601 (2002).
12. Stiles, M. D. & Zangwill, A. Anatomy of spin-transfer torque. *Phys. Rev. B* **66,** 014407 (2002).
13. Xia, K., Kelly, P. J., Bauer, G. E. W., Brataas, A. & Turek, I. Spin torques in ferromagnetic/normal-metal structures. *Phys. Rev. B* **65,** 220401 (2002).
14. Marti, X. *et al.* Room-temperature antiferromagnetic memory resistor. *Nat. Mater.* **13,** 367–374 (2014).
15. Železný, J. *et al.* Relativistic Néel-Order Fields Induced by Electrical Current in Antiferromagnets. *Phys. Rev. Lett.* **113,** 157201 (2014).

16. Yamanouchi, M. *et al.* Domain Structure in CoFeB Thin Films With Perpendicular Magnetic Anisotropy. *IEEE Magn. Lett.* **2,** 3000304 (2011).

17. Bode, M. *et al.* Chiral magnetic order at surfaces driven by inversion asymmetry. *Nature (London)* **447,** 190–193 (2007).

18. Torrejon, J. *et al.* Interface control of the magnetic chirality in CoFeB/MgO heterostructures with heavy-metal underlayers. *Nat. Comm.* **5,** 4655 (2014).

19. Mangin, S. *et al.* Current-induced magnetization reversal in nanopillars with perpendicular anisotropy. *Nat. Mater.* **5,** 210–215 (2006).

20. Bazaliy, Y. B., Jones, B. A. & Zhang, S.-C. Modification of the Landau-Lifshitz equation in the presence of a spin-polarized current in colossal- and giant-magnetoresistive materials. *Phys. Rev. B* **57,** R3213–R3216 (1998).

21. Xiao, J., Zangwill, A. & Stiles, M. D. Macrospin models of spin transfer dynamics. *Phys. Rev. B* **72,** 014446 (2005).

22. Liu, L. *et al.* Spin-Torque Switching with the Giant Spin Hall Effect of Tantalum. *Science* **336,** 555–558 (2012).

23. Niimi, Y. *et al.* Giant Spin Hall Effect Induced by Skew Scattering from Bismuth Impurities inside Thin Film CuBi Alloys. *Phys. Rev. Lett.* **109,** 156602 (2012).

24. Laczkowski, P. *et al.* Experimental evidences of a large extrinsic spin Hall effect in AuW alloy. *Appl. Phys. Lett.* **104,** 142403 (2014).

25. Narayanapillai, K. *et al.* Current-driven spin orbit field in $LaAlO_3$/$SrTiO_3$ heterostructures. *Appl. Phys. Lett.* **105,** 162405 (2014).

26. Kato, Y. K., Myers, R. C., Gossard, A. C. & Awschalom, D. D. Observation of the Spin Hall Effect in Semiconductors. *Science* **306,** 1910–1913 (2004).

27. Yokoyama, T., Zang, J. & Nagaosa, N. Theoretical study of the dynamics of magnetization on the topological surface. *Phys. Rev. B* **81,** 241410 (2010).

28. Chen, J., Jalil, M. & Tan, S. Current-Induced Spin Torque on Magnetization Textures Coupled to the Topological Surface States of Three-Dimensional Topological Insulators. *J. Phys. Soc. Jap.* **83,** 064710 (2014).

29. Mellnik, A. R. *et al.* Spin-transfer torque generated by a topological insulator. *Nature (London)* **511,** 449–451 (2014).

30. Fan, Y. *et al.* Magnetization switching through giant spin-orbit torque in a magnetically doped topological insulator heterostructure. *Nat. Mater.* **13,** 699–704 (2014).

31. Chen, J., Jalil, M. B. A. & Tan, S. G. Spin torque on the surface of graphene in the presence of spin orbit splitting. *AIP Adv.* **3,** 062127 (2013).

32. Miron, I. M. *et al.* Current-driven spin torque induced by the Rashba effect in a ferromagnetic metal layer. *Nat. Mater.* **9,** 230–234 (2010).

33. Miron, I. M. *et al.* Fast current-induced domain-wall motion controlled by the Rashba effect. *Nat. Mater.* **10,** 419–423 (2011).

34. Hirsch, J. E. Spin Hall Effect. *Phys. Rev. Lett.* **83,** 1834–1837 (1999).

35. Sinova, J. *et al.* Universal Intrinsic Spin Hall Effect. *Phys. Rev. Lett.* **92,** 126603 (2004).

36. Zhang, W., Han, W., Jiang, X., Yang, S.-H. & S. P. Parkin, S. Role of transparency of platinum-ferromagnet interfaces in determining the intrinsic magnitude of the spin Hall effect. *Nat. Phys.* **11,** 496–502 (2015).

37. Pai, C.-F., Ou, Y., Vilela-Leão, L. H., Ralph, D. C. & Buhrman, R. A. Dependence of the efficiency of spin Hall torque on the transparency of Pt/ferromagnetic layer interfaces. *Phys. Rev. B* **92,** 064426 (2015).

38. Liu, L., Moriyama, T., Ralph, D. C. & Buhrman, R. A. Spin-Torque Ferromagnetic Resonance Induced by the Spin Hall Effect. *Phys. Rev. Lett.* **106,** 036601 (2011).

39. Qiu, X. *et al.* Angular and temperature dependence of current induced spin-orbit effective fields in Ta/CoFeB/MgO nanowires. *Sci. Rep.* **4,** 4491 (2014).

40. Pai, C.-F. *et al.* Spin transfer torque devices utilizing the giant spin Hall effect of tungsten. *Appl. Phys. Lett.* **101,** 122404 (2012).

41. Hao, Q. & Xiao, G. Giant Spin Hall Effect and Switching Induced by Spin-Transfer Torque in a W/Co40Fe40B20/MgO Structure with Perpendicular Magnetic Anisotropy. *Phys. Rev. Appl.* **3,** 034009 (2015).

42. Manchon, A. & Zhang, S. Theory of nonequilibrium intrinsic spin torque in a single nanomagnet. *Phys. Rev. B* **78,** 212405 (2008).

43. Obata, K. & Tatara, G. Current-induced domain wall motion in Rashba spin-orbit system. *Phys. Rev. B* **77,** 214429 (2008).

44. Tan, S., Jalil, M., Fujita, T. & Liu, X. Spin dynamics under local gauge fields in chiral spin-orbit coupling systems. *Ann. Phys.* **326,** 207–215 (2011).

45. Kim, K.-W., Seo, S.-M., Ryu, J., Lee, K.-J. & Lee, H.-W. Magnetization dynamics induced by in-plane currents in ultrathin magnetic nanostructures with Rashba spin-orbit coupling. *Phys. Rev. B* **85,** 180404 (2012).

46. Haney, P. M., Lee, H.-W., Lee, K.-J., Manchon, A. & Stiles, M. D. Current-induced torques and interfacial spin-orbit coupling. *Phys. Rev. B* **88,** 214417 (2013).

47. Manchon, A. & Zhang, S. Theory of spin torque due to spin-orbit coupling. *Phys. Rev. B* **79,** 094422 (2009).

48. Haney, P. M., Lee, H.-W., Lee, K.-J., Manchon, A. & Stiles, M. D. Current induced torques and interfacial spin-orbit coupling: Semiclassical modeling. *Phys. Rev. B* **87,** 174411 (2013).

49. Allen, G., Manipatruni, S., Nikonov, D. E., Doczy, M. & Young, I. A. Experimental demonstration of the coexistence of spin Hall and Rashba effects in beta-tantalum/ferromagnet bilayers. *Phys. Rev. B* **91,** 144412 (2015).

50. Fan, X. *et al.* Quantifying interface and bulk contributions to spin-orbit torque in magnetic bilayers. *Nat. Comm.* **5,** 3042 (2014).

51. Pai, C.-F. *et al.* Enhancement of perpendicular magnetic anisotropy and transmission of spin-Hall-effect-induced spin currents by a Hf spacer layer in W/Hf/CoFeB/MgO layer structures. *Appl. Phys. Lett.* **104,** 082407 (2014).

52. Kim, J. *et al.* Layer thickness dependence of the current-induced effective field vector in Ta—CoFeB—MgO. *Nat. Mater.* **12,** 240–245 (2013).

53. Garello, K. *et al.* Symmetry and magnitude of spin-orbit torques in ferromagnetic heterostructures. *Nat. Nanotechnol.* **8,** 587–593 (2013).

54. Qiu, X. *et al.* Spin-orbit-torque engineering via oxygen manipulation. *Nat. Nanotechnol.* **10,** 333–338 (2015).

55. Liu, L., Chen, C.-T. & Sun, J. Z. Spin Hall effect tunnelling spectroscopy. *Nat. Phys.* **10,** 561–566 (2014).

56. Zhang, S. Spin Hall Effect in the Presence of Spin Diffusion. *Phys. Rev. Lett.* **85,** 393–396 (2000).

57. Liu, R. H., Lim, W. L. & Urazhdin, S. Control of current-induced spin-orbit effects in a ferromagnetic heterostructure by electric field. *Phys. Rev. B* **89,** 220409 (2014).

58. Lee, O. J. *et al.* Ultrafast switching of a nanomagnet by a combined out-of-plane and in-plane polarized spin current pulse. *Appl. Phys. Lett.* **95,** 012506 (2009).

59. Lee, O. J., Ralph, D. C. & Buhrman, R. A. Spin-torque-driven ballistic precessional switching with 50ps impulses. *Appl. Phys. Lett.* **99,** 102507 (2011).

60. Thomas, L. *et al.* Perpendicular spin transfer torque magnetic random access memories with high spin torque efficiency and thermal stability for embedded applications (invited). *J. Appl. Phys.* **115,** 172615 (2014).

61. Yan, S. & Bazaliy, Y. B. Phase diagram and optimal switching induced by spin Hall effect in a perpendicular magnetic layer. *Phys. Rev. B* **91,** 214424 (2015).

62. Miron, I. M. *et al.* Perpendicular switching of a single ferromagnetic layer induced by in-plane current injection. *Nature (London)* **476,** 189–193 (2011).

63. Liu, L., Lee, O. J., Gudmundsen, T. J., Ralph, D. C. & Buhrman, R. A. Current-Induced Switching of Perpendicularly Magnetized Magnetic Layers Using Spin Torque from the Spin Hall Effect. *Phys. Rev. Lett.* **109,** 096602 (2012).

64. Lee, K.-S., Lee, S.-W., Min, B.-C. & Lee, K.-J. Threshold current for switching of a perpendicular magnetic layer induced by spin Hall effect. *Appl. Phys. Lett.* **102,** 112410 (2013).

65. Finocchio, G., Carpentieri, M., Martinez, E. & Azzerboni, B. Switching of a single ferromagnetic layer driven by spin Hall effect. *Appl. Phys. Lett.* **102,** 212410 (2013).

66. Avci, C. O. *et al.* Fieldlike and antidamping spin-orbit torques in as-grown and annealed Ta/CoFeB/MgO layers. *Phys. Rev. B* **89,** 214419 (2014).

67. Taniguchi, T., Mitani, S. & Hayashi, M. Critical current destabilizing perpendicular magnetization by the spin Hall effect. *Phys. Rev. B* **92,** 024428 (2015).

68. Zhang, C., Fukami, S., Sato, H., Matsukura, F. & Ohno, H. Spin-orbit torque induced magnetization switching in nano-scale Ta/CoFeB/MgO. *Appl. Phys. Lett.* **107,** 012401 (2015).

69. Mikuszeit, N. *et al.* Spin-orbit torque driven chiral magnetization reversal in ultrathin nanostructures. *Phys. Rev. B* **92,** 144424 (2015).

70. Lee, O. J. *et al.* Central role of domain wall depinning for perpendicular magnetization switching driven by spin torque from the spin Hall effect. *Phys. Rev. B* **89,** 024418 (2014).

71. Pizzini, S. *et al.* Chirality-Induced Asymmetric Magnetic Nucleation in Pt / Co / AlOx Ultrathin Microstructures. *Phys. Rev. Lett.* **113,** 047203 (2014).

72. Martinez, E. *et al.* Universal chiral-triggered magnetization switching in confined nanodots. *Sci. Rep.* **5,** 10156 (2015).

73. Liu, H. *et al.* Dynamics of spin torque switching in all-perpendicular spin valve nanopillars. *J. Magn. Magn. Mat.* **358-359,** 233–258 (2014).

74. Yamanouchi, M. *et al.* Three terminal magnetic tunnel junction utilizing the spin Hall effect of iridium-doped copper. *Appl. Phys. Lett.* **102,** 212408 (2013).

75. Garello, K. *et al.* Ultrafast magnetization switching by spin-orbit torques. *Appl. Phys. Lett.* **105,** 212402 (2014).

76. Cubukcu, M. *et al.* Spin-orbit torque magnetization switching of a three-terminal perpendicular magnetic tunnel junction. *Appl. Phys. Lett.* **104,** 042406 (2014).

77. Yu, G. *et al.* Switching of perpendicular magnetization by spin-orbit torques in the absence of external magnetic fields. *Nat. Nanotechnol.* **9,** 548–554 (2014).

78. You, L. *et al.* Switching of perpendicularly polarized nanomagnets with spin orbit torque without an external magnetic field by engineering a tilted anisotropy. *Proc. Natl. Acad. Sci. USA* **112,** 10310–10315 (2015).

79. Wang, D. Spin-orbit field switching of magnetization in ferromagnetic films with perpendicular anisotropy. *Appl. Phys. Lett.* **100,** 212405 (2012).

80. Lee, K.-S., Lee, S.-W., Min, B.-C. & Lee, K.-J. Thermally activated switching of perpendicular magnet by spin-orbit spin torque. *Appl. Phys. Lett.* **104,** 072413 (2014).

81. Park, J., Rowlands, G. E., Lee, O. J., Ralph, D. C. & Buhrman, R. A. Macrospin modeling of sub-ns pulse switching of perpendicularly magnetized free layer via spin-orbit torques for cryogenic memory applications. *Appl. Phys. Lett.* **105,** 102404 (2014).

82. Schumacher, H. W. *et al.* Phase Coherent Precessional Magnetization Reversal in Microscopic Spin Valve Elements. *Phys. Rev. Lett.* **90,** 017201 (2003).

83. Akyol, M. *et al.* Effect of the oxide layer on current-induced spin-orbit torques in Hf—CoFeB—MgO and Hf—CoFeB—TaOx structures. *Appl. Phys. Lett.* **106,** 032406 (2015).

84. Donahue, M. & Porter, D. OOMMF Users Guide, Version 1.0. *National Institute of Standards and Technology Technical Report* **6376,** 158 (1999).

85. Emori, S. *et al.* Spin Hall torque magnetometry of Dzyaloshinskii domain walls. *Phys. Rev. B* **90,** 184427 (2014).

86. Brown, W. F. Thermal Fluctuations of a Single-Domain Particle. *Phys. Rev.* **130,** 1677–1686 (1963).

87. Cheng, X. Z., Jalil, M. B. A., Lee, H. K. & Okabe, Y. Mapping the Monte Carlo Scheme to Langevin Dynamics: A Fokker-Planck Approach. *Phys. Rev. Lett.* **96,** 067208 (2006).

88. Butler, W. H. *et al.* Switching Distributions for Perpendicular Spin-Torque Devices Within the Macrospin Approximation. *IEEE Trans. Magn.* **48,** 4684–4700 (2012).

89. Taniguchi, T., Utsumi, Y., Marthaler, M., Golubev, D. S. & Imamura, H. Spin torque switching of an in-plane magnetized system in a thermally activated region. *Phys. Rev. B* **87,** 054406 (2013).

90. Braun, H.-B. & Loss, D. Berry's phase and quantum dynamics of ferromagnetic solitons. *Phys. Rev. B* **53,** 3237–3255 (1996).

91. Sukhorukov, E. V. & Jordan, A. N. Stochastic Dynamics of a Josephson Junction Threshold Detector. *Phys. Rev. Lett.* **98,** 136803 (2007).

92. Lo Conte, R. *et al.* Spin-orbit torque-driven magnetization switching and thermal effects studied in Ta/CoFeB/MgO nanowires. *Appl. Phys. Lett.* **105,** 122404 (2014).

93. Van den Brink, A. *et al.* Spin-Hall-assisted magnetic random access memory. *Appl. Phys. Lett.* **104,** 012403 (2014).

94. Boulle, O. *et al.* Shaped angular dependence of the spin-transfer torque and microwave generation without magnetic field. *Nat. Phys.* **3,** 492–497 (2007).

95. Lee, K.-S. *et al.* Angular dependence of spin-orbit spin-transfer torques. *Phys. Rev. B* **91,** 144401 (2015).

96. Aharoni, A. Demagnetizing factors for rectangular ferromagnetic prisms. *J. Appl. Phys.* **83,** 3432–3434 (1998).